徳島大学
The University of Tokushima

Dissertation for Doctoral Degree

Development of advanced elemental detection methods in particles and gases using laser-induced breakdown spectroscopy and laser breakdown time-of-flight mass spectrometry for the application to thermal and nuclear power plants

A dissertation submitted to
The University of Tokushima
in partial fulfillment of the requirements
for the doctor degree

By
Wang Zhenzhen
Supervisor: Prof. Deguchi Yoshihiro; Prof. Yan Junjie
(Intelligent structures and mechanics system engineering)

June 2014

Development of advanced elemental detection methods in particles and gases using laser-induced breakdown spectroscopy and laser breakdown time-of-flight mass spectrometry for the application to thermal and nuclear power plants

Mechanical engineering

Intelligent structures and mechanics system engineering

The University of Tokushima

Wang Zhenzhen

June 2014

Abstract

In order to simulate coal combustion and develop optimal and stable boiler control systems in real power plants, it is imperative to obtain the detailed information in coal combustion processes as well as to measure species contents in fly ash, which should be controlled and analyzed for enhancing boiler efficiency and reducing environmental pollution. The fly ash consists of oxides (SiO_2, Al_2O_3, Fe_2O_3, CaO, and so on), unburned carbon, and other minor elements. Recently, laser-induced breakdown spectroscopy (LIBS) technique has been applied to coal combustion and other industrial fields because of the fast response, high sensitivity, real-time and non-contact features. In these applications it is important to measure controlling factors without any sample preparation to maintain the real-time measurement feature. The relation between particle content and particle diameter is also one of the vital researches, because compositions of particles are dependent on their diameter. In this study, the contents of size-segregated particles have been detected using LIBS. Particles were classified by an Anderson cascade impactor. The plasma conditions such as plasma temperature are dependent on the size of particles and these effects must be corrected to obtain quantitative information. The plasma temperature was corrected by the emission intensity ratio from the same atom. Using this correction method, the contents of particles can be measured quantitatively in fixed experimental parameters. This method was applied to coal and fly ash from a coal-fired burner to measure unburned carbon and other contents according to the particle diameter. The CO_2 effect was also discussed to accurately evaluate unburned carbon in fly ash in exhausts. The acquired results demonstrate that the LIBS technique is applicable to measure size-segregated particle contents in real time and this method is useful for the analyses of coal combustion and its control because of its sensitive and fast analysis features.

It has been highly recognized heavy metals and other trace species pollution concerns the environment, as well as human health. This paper also describes the rapid detection of trace species such as mercury and iodine using low pressure laser-induced breakdown spectroscopy (LIBS) and laser breakdown time-of-flight mass spectrometry (LB-TOFMS) at improved sensitivity. One of the challenging targets of LIBS is the enhancement of detection limit. In this study, the detection limit of gas phase LIBS analysis has been improved by controlling the pressure and laser pulse width. In order to verify this method, low pressure gas plasma was induced by nanosecond and picosecond lasers. Several trace species of mercury (Hg), iodine, cesium (Cs), strontium (Sr) and so on were measured using low pressure LIBS. For example, the method was applied to the detection of Hg, and the emission intensity ratio of Hg atom: I_{Hg} to NO emission signal: I_{NO} (interference signal), which was formed during the plasma generation and cooling process of N_2 and O_2 in the air, was analyzed to evaluate LIBS detection limit. It was demonstrated that the enhancement of I_{Hg}/I_{NO} arose by decreasing the pressure to a few kPa and I_{Hg}/I_{NO} of picosecond breakdown was always much higher than that of nanosecond breakdown at

low buffer gas pressure. The measurement results of iodine in N_2 demonstrated that low-pressure LIBS is the favorable method for trace species measurement in analytical application. The plasma generation process can be controlled by the pressure and laser pulse width for the larger ionization and excitation processes of iodine, which was discussed by the intensity ratio of iodine emission at 183 nm to nitrogen emission at 174.3 nm. The buffer gas effect was also discussed by the measurements of Hg and iodine in different buffer gases of air and N_2. The Hg detection limit (1 min) in air of nanosecond breakdown was 450 ppb ($3\sigma/m_s$) at 700 Pa. According to the enhancement of picosecond breakdown at low pressure, the detection limit was evaluated to be 30 ppb ($3\sigma/m_s$) in picosecond (35 ps) breakdown at 700 Pa. The detection limit can be enhanced when employing the buffer gas of N_2. Iodine detection limit (1 min) in the buffer gas of N_2 was 60 ppb ($3\sigma/m_s$) in nanosecond breakdown at pressure of 700 Pa. there was not evident enhancement of iodine detection limit in N_2 employing short pulse width breakdowns. The detection limit of iodine in air became worse due to the high quenching rate of excited iodine in buffer gas of air.

In the measurements of Hg and iodine using LB-TOFMS, two irradiation wavelengths of 1064 nm and 532 nm were employed under various experimental conditions without partial fragmentation interference from other species. The second harmonic 532 nm performs excellent measurement results. The influence of pressure on signal intensity displays a linear growth when increasing the pressure. The power dependence shows that as the laser power increased, mercury ion and iodine ion signal intensity increased first and then decreased. Experiment with different buffer gases clarified the recombination of mercury ion and iodine ion with electrons when the laser power increased, resulting in the decrease of mercury ion and iodine ion signal intensity. Mercury ion signal intensity can be enhanced 3.8 times and the signal intensity of iodine ion can be enhanced 1.3 times employing 35 ps 532 nm breakdown. The detection limits (2 mins) of mercury ion and iodine ion signals using 35 ps laser were 0.82 ppb ($3\sigma/m_s$) and 6.18 ppb ($3\sigma/m_s$) respectively.

Keywords: Fine particles; Size-segregation; Temperature correction; Trace species; Sensitive measurement; Low pressure laser-induced breakdown spectroscopy (LIBS); Laser breakdown time-of-flight mass spectrometry (LB-TOFMS)

Contents

Main symbol table

amu	Atomic Mass Unit
LB-TOFMS	Laser Breakdown Time-of-Flight Mass Spectrometry
LIBS	Laser-Induced Breakdown Spectroscopy
ppm	parts-per-million; 10^{-6}
ppb	parts-per-billion; 10^{-9}
ppt	parts-per-trillion; 10^{-12}
$D_{i,j}$	emission intensity correction factor from the upper energy level j of species i
$E_{i,j}$	upper level energy of species i/J
I_i	emission intensity of species i/J·s^{-1}
$I_{m,j1}$	emission intensity from the upper energy level j_1 of species m
$I_{m,j2}$	emission intensity from the upper energy level j_2 of species m
$K_{i,j}$	a variable that includes the Einstein A coefficient from the upper energy level j/J·m^3·s^{-1}
L	ion distance of flight/m
T	plasma temperature /K
V	acceleration electric field potential/V
$b_{i,m}$	temperature correction factor of the emission pair of $I_{m,j1}$ and $I_{m,j2}$ for species i
$g_{i,j}$	statistical weight of species *i* at the upper energy level j
k	the Boltzmann constant/1.38×10^{-23}J·K^{-1}
m	ion mass/kg
m_s	slope of the calibration curve
n_i	concentration of species i/m^{-3}
t	time of flight/s
z	ionic valence /C
α	angle/^{o}
α_i	a variable factor related to species i, which contains the plasma temperature correction factor
σ	standard deviation
Subscript	
i	element
j	energy level
m	element

1 Introduction

1.1 Background and significance

With the development of economy, the environmental pollution is becoming increasingly severe and much more attention should be paid to the issue[1-3]. In recent years, various pollution incidents result in serious influences on environment and human health[4-6]. The major sources of these contaminations include industry, traffic and domestic waste. The atmosphere as an important part of the urban environment suffers from human interference. Increased combustion of fossil fuels is responsible for the progressive change in the atmospheric composition. Air pollutants, such as CO, SO_2, NO_x, VOCs, O_3, heavy metals, PM2.5 and PM10, have both acute and chronic effects on human health. Several regulations and standards have been set by such agencies as the United States Environmental Protection Agency (US EPA) and the World Health Organization (WHO). Air pollution can also travel hundreds of miles and cause multiple health and environmental problems on regional or national scales[7,8]. It is imperative to detect these contaminations compounding in complex substances in the atmosphere.

As mercury is widely used in various industries, mercury pollution or its potentiality is one of the serious environmental problems concerning human health[9-12]. Power plants are currently the dominant emitters of mercury, acid gases and many toxic metals in the U.S. because the other sources of mercury have already reduced their emissions, such as medical waste incinerators and municipal waste combustors. In 2011, EPA finalized the first ever national standards to reduce mercury and other toxic air pollution from coal and oil-fired power plants. There are some examples of mercury vapour exposure guidelines, such as worker exposure of 25,000 ng/m^3 (one hour exposure, ACGIH) and residential exposure of 300 ng/m^3 (average annual exposure, New York State recommendations). It is necessary to make efforts to protect natural ecosystems and effectively utilize fossil fuels in various fields. Therefore, the understanding of the reaction mechanism of combustion is becoming more important to minimize environmental disruption and to improve the efficiency of combustors.

Electricity is the world's fastest-growing form of end-use energy consumption. The coal provides the largest share of world electricity generation and the thermal power plant share is dominant in total electric power supply in the world. Operating characteristics of coal-fired boilers are heavily influenced by factors such as differences in fuel properties and the combustion conditions. Accordingly, in order to achieve optimal operation of multiple coal-fired boilers, it is necessary to accurately understand the state of combustion and to adjust the control parameters. Nuclear power is a proven means to supply the growing demand for clean energy in our energy future. The importance of nuclear power is obviously depending on the basis of safe and rational utilization. Radioactive substances, such as strontium (Sr), iodine (I), cesium (Cs), uranium (U), plutonium (Pu) etc. should be paid much more attention to this issue.

In thermal power plants, the boiler control system is important for the adjustment of combustion process. 2D temperature and concentration distribution also plays an important role for the efficiency. The coal and fly ash contents, especially unburned carbon in fly ash, are the major factors of efficient combustion. As is well known, fly ash produced during coal combustion is one of the sources of fine particles. The compositions of fly ash, which contains SiO_2, Al_2O_3, Fe_2O_3, CaO, unburned carbon and other materials, are complex and highly depending on the coal quality and combustion procedure. Fig. 1-1 shows the system of coal-fired power plant and the necessary measurement items. Simultaneously, there is an urgent need to evaluate the heavy metal emission for the purpose of reducing and eliminating heavy metal influence. For example, Mercury (Hg) pollution has greatly increased and been considered as a global pollutant because of its long residence time[9-11]. Coal combustion in power plant constitutes the large share of global anthropogenic Hg emission. The harmful substances, such as heavy metals, are produced during the combustion processes in engines, boilers, other combustors. The rapid and precise measurement of trace species with variable compositions is imperative according to different applications.

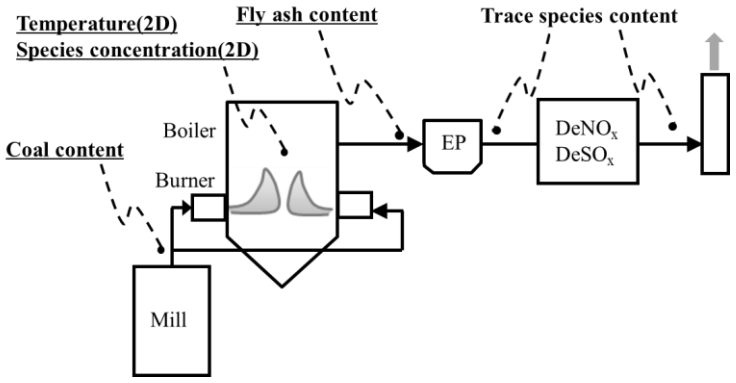

(a) Measurement items

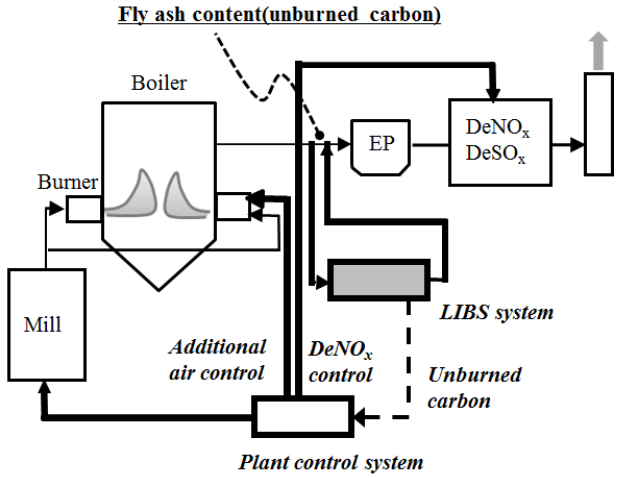

(b) Advanced control system by the real-time measurement of unburned carbon in fly ash

Fig. 1-1 System of coal-fired power plant

Nuclear power is a proven means to supply the growing demand for clean energy in our energy future. The importance of nuclear power is obviously depending on the basis of safe and rational utilization. Radioactive substances, such as strontium (Sr), iodine (I), cesium (Cs), uranium (U), plutonium (Pu) etc. should be paid much more attention to the radioactive contamination. The radioactive contamination released from the nuclear power plant is one of the main sources. Simultaneously, nuclear weapons testing fallout, some industry waste discharge, and radioactive substances applied for research[13,14] also contribute to the issue. The atmosphere, water, and soil are polluted by these released radioactive materials including iodine (I), cesium (Cs), strontium (Sr), barium (Ba), zirconium (Zr) and so on[15-17]. As is well known, after the Fukushima nuclear power plant accident in Japan, there are several serious pollutions to environment and human not only in the surrounding area of the nuclear power plant but also in the extensive regions[18-20]. The pollution of the radioactive materials becomes the focal issue and research point. Human and other organisms can be taken the radioactive materials, such as iodine, Cs, Sr, Se and so on, which leads to severe disease. Fig. 1-2 shows the schematic diagram of nuclear power plant and the necessary measurement items.

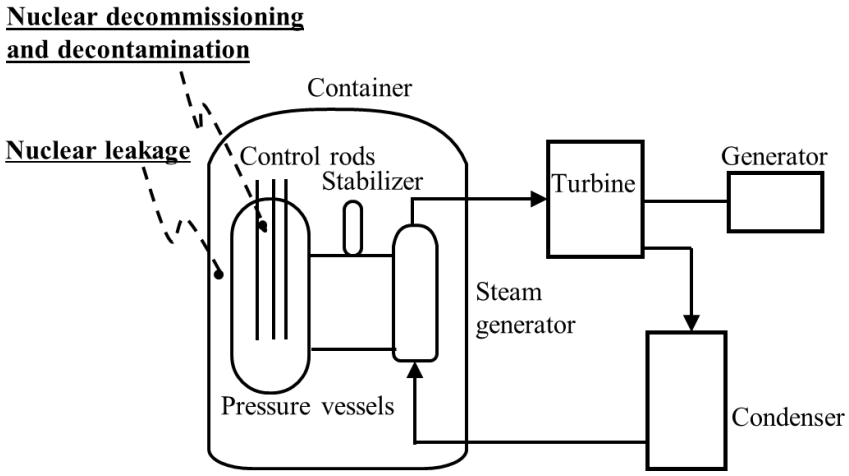

Fig. 1-2 System of nuclear power plant

1.2 Research status

The rapid and precise measurement of fine particles and trace species is imperative according to different applications. Laser diagnostics has attracted a great attention in various industries because of the non-contact, fast response and multi-dimensional features as the qualitative and quantitative analytical detection technique, such as laser-induced fluorescence (LIF), laser-induced breakdown spectroscopy (LIBS), tunable diode laser absorption spectroscopy (TDLAS), time-of-flight mass spectrometry (TOFMS) and so on[21,22]. LIBS is an analytical detection technique based on atomic emission spectroscopy to measure elemental composition. With the development of lasers and detection systems, LIBS has been applied in various fields containing solid, liquid and gas phases, such as combustion[23-27], metallurgy[28-30], food[31-33], human[34,35]

and others[36,37]. Especially, the advantages of the method are more significant in the areas of combustion, metallurgy and the harsh environment.

TOFMS is another appealing technique for the qualitative and quantitative analysis of atomic and molecular ion signal with the features of increased sensitivity and rapid analysis. The detection limit of measured species using TOFMS is often ppb or less. TOFMS has been applied to measure the hydrocarbons and nanoparticle constituents with the low concentration range of ppb-ppt[38-42], as well as waste disposal and treatment plants[43-45]. There are other developed TOFMS applications in several fields, such as medical and pharmaceutical fields[46,47].

1.2.1 Measurement of particles

Measurement of fine particles is important to study the pollution in environmental and industrial areas. Some problems of acid rain and photochemical smog are related to particulate matter 2.5 (PM2.5), referring to the particles with diameter of 2.5 μm or less, also known as the particles into the lungs. The fine particles containing toxic trace elements also affect human health. Fly ash produced during coal combustion is one of the sources of fine particles. The compositions of fly ash, which contains SiO_2, Al_2O_3, Fe_2O_3, CaO, unburned carbon and other materials, are complex highly depending on the coal quality and combustion procedure. Unburned carbon is a major determinant of combustion efficiency in coal-fired boiler. Recently, laser-induced breakdown spectroscopy (LIBS) technique has been applied to coal combustion and other industrial fields because of the fast response, high sensitivity, real-time and non-contact features. For the purpose of improving the economy and security of power plant, the content measurement of unburned carbon and other materials is essential for adjusting the boiler combustion.

The versatility and multi-elemental capability of LIBS have been demonstrated for the analysis of heterogeneous materials such as coal and mineral ores. Various elements included in samples can be detected simultaneously within a very short time[48,49]. LIBS technique has been widely applied to analyze the compositional characterization of coal. For example, inorganic species in coal were analyzed quantitatively under different conditions[50,51]. The solid sample features higher homogeneity than powdered counterparts. The feasibility of using binder for carbon measurement in anthracite has been studied[52]. In order to enhance the repeatability and precision of the results determining coal fly ash elemental composition, different blinders were employed for various coal samples[53]. This research group also analyzed fly ash and bottom ash using the same treating processes with collinear double pulse approach to address the influence of matrix effect on the calibration curves[54]. In these studies all samples should be prepared before measurement.

LIBS has been applied for detection of unburned carbon in fly ash, char and pulverized coal under high-pressure and high-temperature conditions without any sample preparation. The calibration difficulty of aerosol sample was surpassed by the correction factors for quantitative

measurement. This automated LIBS apparatus were also applied in a boiler-control system of a power plant with the objective of achieving optimal and stable combustion[55,56], which enabled real-time measurement of unburned carbon in fly ash as shown in Fig. 1-1(b). This apparatus featured a detection time capability of less than 1 minute, which showed better real-time capability compared to other methods (preparation of samples) used in other studies[49-54]. The boiler control in the real power plant was also demonstrated to achieve an optimized operation without time consumption. In these studies, unburned carbon in unclassified fly ash was analyzed and the effects of particle size to its contents have not been discussed. Furthermore, dependence of elemental signals of LIBS on the plasma temperature attributes to a very complex process in plasma. Several studies have reported the LTE (Local Thermodynamic Equilibrium) condition of plasma in several types of plasmas[57]. The plasma temperature is a very important factor for the quantification of the LIBS measurement[22,56]. The improvement of quantitative and real-time measurement is very necessary for the operation of coal-fired plants.

1.2.2 Measurement of trace species

Various harmful materials pollutions releasing from industry, traffic and domestic waste result in serious influence on environment and human health. Tighter environmental regulations recently have focused on global limit of harmful substances. Several papers have reported the measurement of trace species Hg, Cd, and Pb in different fields[58-63]. For example, coal combustion in power plant constitutes the large share of global anthropogenic Hg emission. There is an urgent need to evaluate Hg emission for the purpose of reducing and eliminating Hg influence. The behavior of Hg in coal-fired power plants has been studied extensively[64-67]. Flue gases for Hg analyses are sampled by different chemical methods and measured off-line. Because of the low concentration of these species, enrichment and separation are essential to analyze the trace species using these conventional methods, however these procedures usually take long time. On the other hand, due to the restriction of their detection limits these methods cannot obtain satisfactory results in some applications. Inductively coupled plasma-atomic emission spectroscopy (ICP-AES) and inductively coupled plasma-mass spectrometry (ICP-MS) have also been applied to detect the trace species[68-71]. However there is time consumption for the sample preparation.

With the development of laser technology, short pulse width lasers, such as picosecond laser and femtosecond laser have been employed to LIBS technique. The ablation mechanisms of nanosecond, picosecond and femtosecond pulses are different. As a result of the short duration, the laser pulse has terminated before the interactions of laser and material, plasma, and buffer gas concerning the complicated procedure. The utilization of short pulse laser for plasma generation has been extensively studied. Three femtosecond lasers were employed based stand-off sensing and spectroscopy techniques including LIBS, coherent Raman spectroscopy and THz spectroscopy[72]. Femtosecond irradiation allowed for a specificity of excitation that could yield

LIBS signals more tightly correlated to particular chemical species. Some comparisons between nanosecond and picosecond breakdown were made through LIBS spectra of aluminum, iron, and copper in metal samples and glass[73]. The picosecond laser pulse showed significantly lower background emission than the results of nanosecond laser.

However, laser-induced plasma process in gas phase is different from that in solid phase. There is no ablation process and the laser is used to atomize the molecules and generate the free electrons by multi-photon ionization. The interaction between atoms and electrons with enough energy makes the atoms ionize continuously and produces more electrons, resulting in the generation of plasma. To investigate the phenomena described above, a theoretical model using the lattice Boltzmann method (LBM) was applied and plasma creation processes were analyzed including multi-photon ionization and electron impact ionization processes. Creation and evolution processes of particles (electron, ion, and neutral) in plasma were clarified using LBM to solve the continuous Boltzmann equations used to model the generation of plasma[74]. One of the challenging targets of LIBS is the enhancement of detection limit of gas phase materials. Though the experiments have been mainly applied to direct observation of post-breakdown processes, a new method to control the LIBS plasma generation process is necessary for the enhancement of detection limit.

1.3 Contents and structure of this dissertation

The contents of fine particles also depend on particle diameter. Several studies have reported the distribution characteristics of trace elements in coal and fly ash[75-77]. It has been proved that the main elements in particles also have a very important impact on the distribution of some trace elements[78,79]. Therefore it is also necessary to measure the elemental compositions according to the particle diameter. In this study, an improved LIBS method has been applied to detect the contents of size-segregated particles with the temperature correction method and surrounding gas effect to the further applications. These factors are important for practical applications. Particles were classified by an Anderson cascade impactor and then measured using LIBS technique. The contents of particles such as fly ash and coal were measured quantitatively according to the diameter using a plasma temperature correction method. It has also been demonstrated that this method can be applicable to clarify the compositional dependence on the particle diameter of fly ash and coal in coal-fired thermal power plants.

In order to measure the trace species of heavy metals, radioactive materials and others, advanced LIBS and TOFMS methods with the features of increased sensitivity and rapid analysis have been employed in this study. One of the challenging targets of LIBS is the enhancement of detection limit of gas phase materials. Though the experiments have been mainly applied for direct observation of post-breakdown processes, a new method to control the LIBS plasma generation process is necessary for the enhancement of detection limit, i.e. low pressure and short pulse laser-induced breakdown spectroscopy. Considering the features of TOFMS,

fragmentation and signal intensity are the important factors for sensitive measurement. In order to eliminate or minimize the interference of fragmentation to heavy atoms, the method of laser breakdown combined with time-of-flight mass spectrometry was employed to measure trace species. The laser is introduced to break and ionize the measured species for the detection of ion signals using TOFMS. The trace species of Hg, iodine, Sr, Cs and As were measured in this study using low pressure laser-induced breakdown spectroscopy (LIBS) and laser breakdown time-of-flight mass spectrometry (LB-TOFMS). The comparison of their detection characteristics was discussed by measuring Hg and iodine in detail.

Therefore, the aim of current research is the applications of laser diagnostics in thermal and nuclear power plants. The contents of coal and fly ash, and the trace species of heavy metals and radioactive materials were measured using advanced LIBS and LB-TOFMS methods. The applicability of these methods to thermal and nuclear power plants was also discussed.

2 Theories

Two types of laser diagnostics technologies were employed in the measurements of fine particles and trace species. The principles behind laser-induced breakdown spectroscopy (LIBS) and laser breakdown time-of-flight mass spectrometry (LB-TOFMS) were clarified as follows.

2.1 Laser-induced breakdown spectroscopy and temperature correction method

In the LIBS process, a laser beam is focused into a small area, producing hot plasma. The material contained in the plasma is atomized and the light corresponding to a unique wavelength of each element is emitted from excited atoms in the plasma, as shown in Fig. 2-1.

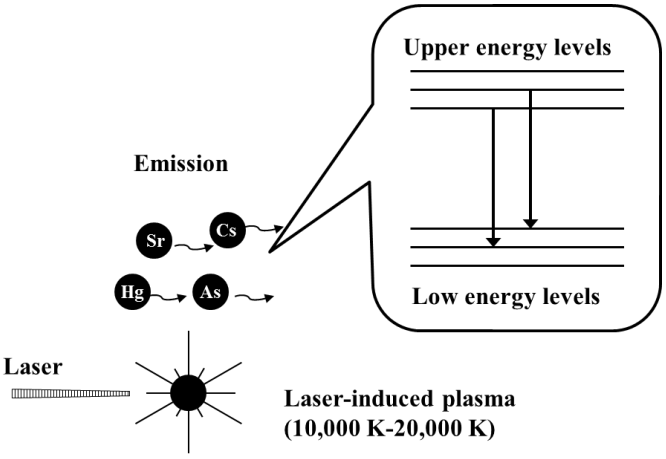

Fig. 2-1 Laser-induced plasma process

A calibration of the LIBS signal is necessary for quantitative analysis. Despite the fact that the LIBS processes involved are complex, the emission intensity from the atomized species can be described by the following equation with the assumption of uniform plasma temperature[22]:

$$I_{\mathrm{i}} = n_{\mathrm{i}} K_{\mathrm{i,j}} g_{\mathrm{i,j}} \exp\left(-\frac{E_{\mathrm{i,j}}}{kT}\right) \tag{2-1}$$

In the above expression, I_{i} is the emission intensity of species i, n_{i} is the concentration of species i, $K_{\mathrm{i,j}}$ is a variable that includes the Einstein A coefficient from the upper energy level j, $g_{\mathrm{i,j}}$ is the statistical weight of species i at the upper energy level j, $E_{\mathrm{i,j}}$ is the upper level energy of species i, k is the Boltzmann constant and T is the plasma temperature. Eq. (2-1) is applicable under the conditions of local thermodynamic equilibrium (LTE). In Eq. (2-1), there are several factors that affect the emission intensity I_{i}, including plasma temperature, plasma non-uniformity, and matrix effects, etc. The appropriate correction factors must be contained in $K_{\mathrm{i,j}}$ to obtain quantitative results.

Because of the strong signal intensity and the relative simplicity of the LIBS technique, LIBS can be applicable for real-time composition measurement of coal and fly ash. Quantitative

capability of LIBS was improved using the proposed plasma temperature correction method. The main components of fly ash are Si, Al, Fe, Ca and C (carbon). The carbon content in fly ash can be calculated using the emission intensity ratios of Al, Fe, Ca and C to Si that is the main element in fly ash, from the following relation:

$$Carbon\ content = \frac{\alpha_C I_C / I_{Si}}{1+\alpha_{Al} I_{Al}/I_{Si} + \alpha_{Fe} I_{Fe}/I_{Si} + \alpha_{Ca} I_{Ca}/I_{Si} + \alpha_C I_C/I_{Si}} \tag{2-2}$$

α_i is a variable factor related to species *i*, which contains the plasma temperature correction factor. These parameters have to be determined in the experimental operating conditions. Other species contents besides carbon, such as Al, Fe and Ca, can also be calculated using the similar relation.

In Eq. (2-1), we assume a uniform plasma temperature. Actually, emission intensity I_i is a function of concentration of species i and plasma temperature. The emission intensity for each element also fluctuates with plasma temperature, which introduces error into quantitative measurements. There are several methods of plasma temperature correction. The following equation is used in this study. α_i is defined by use of the intensity ratio of $I_{m,j1}/I_{m,j2}$:

$$\alpha_i = D_{i,j}\left(I_{m,j1}/I_{m,j2}\right)^{b_{i,m}} \tag{2-3}$$

$D_{i,j}$ is the emission intensity correction factor from the upper energy level *j* of species i. $I_{m,j1}$ is the emission intensity from the upper energy level j_1 of species m, $I_{m,j2}$ is the emission intensity from the upper energy level j_2 of species m, and $b_{i,m}$ is the temperature correction factor of the emission pair of $I_{m,j1}$ and $I_{m,j2}$ for species i. $(I_{m,j1}/I_{m,j2})^{bi,m}$ is dependent on plasma temperature and is used for plasma temperature correction. Different spectral lines from the same species are selected to correct the plasma temperature dependence of the emission intensity, and the intensity ratio of the emission pair is determined from Eq. (2-1):

$$\frac{I_{m,j1}}{I_{m,j2}} = \frac{K_{m,j1} g_{m,j1}}{K_{m,j2} g_{m,j2}} \exp\left(-\frac{E_{m,j1}-E_{m,j2}}{kT}\right) \tag{2-4}$$

Applying the intensity ratio to Eq. (2-3), α_i becomes:

$$\alpha_i = D_{i,j}\left(\frac{K_{m,j1} g_{m,j1}}{K_{m,j2} g_{m,j2}}\right)^{b_{i,m}} \exp\left[b_{i,m}\left(-\frac{E_{m,j1}-E_{m,j2}}{kT}\right)\right] \tag{2-5}$$

Taking C (carbon) from the upper energy level j_C for example, the concentration ratio is as follows:

$$\alpha_C \frac{I_C}{I_{Si}} = \alpha_C \frac{n_C}{n_{Si}}\left(\frac{K_{C,jC} g_{C,jC}}{K_{Si,jSi} g_{Si,jSi}}\right)\exp\left[-\frac{E_{C,jC}-E_{Si,jSi}}{kT}\right]$$

$$= D_{\mathrm{C,jC}} \frac{n_{\mathrm{C}}}{n_{\mathrm{Si}}} \left(\frac{K_{\mathrm{C,jC}} g_{\mathrm{C,jC}}}{K_{\mathrm{Si,jSi}} g_{\mathrm{Si,jSi}}} \right) \exp\left[-\frac{E_{\mathrm{C,jC}} - E_{\mathrm{Si,jSi}}}{kT} \right] \left(I_{\mathrm{m,j1}} / I_{\mathrm{m,j2}} \right)^{b_{\mathrm{C,m}}}$$

$$= D_{\mathrm{C,jC}} \frac{n_{\mathrm{C}}}{n_{\mathrm{Si}}} \left(\frac{K_{\mathrm{C,jC}} g_{\mathrm{C,jC}}}{K_{\mathrm{Si,jSi}} g_{\mathrm{Si,jSi}}} \right) \left(\frac{K_{\mathrm{m,j1}} g_{\mathrm{m,j1}}}{K_{\mathrm{m,j2}} g_{\mathrm{m,j2}}} \right)^{b_{\mathrm{C,m}}} \cdot \exp\left[-\left(b_{\mathrm{C,m}} \frac{E_{\mathrm{m,j1}} - E_{\mathrm{m,j2}}}{kT} + \frac{E_{\mathrm{C,jC}} - E_{\mathrm{Si,jSi}}}{kT} \right) \right] \quad (2\text{-}6)$$

This ratio becomes a function of species concentration and does not depend on the plasma temperature on condition that $b_{\mathrm{C,m}}$ is given as follows:

$$b_{\mathrm{C,m}} = -\frac{E_{\mathrm{C,jC}} - E_{\mathrm{Si,jSi}}}{E_{\mathrm{m,j1}} - E_{\mathrm{m,j2}}} \quad (2\text{-}7)$$

From this analytical result, the correction factor can be calculated using the above equation. However, the correction factor depends on the experimental parameters such as the optical setups, pressure, buffer gas composition, and so on. The plasma induced by the LIBS process is not uniform and complex and LTE can be assumed in the limited range of these experimental conditions. In the case of ion emission intensities it is also necessary to consider the degree of ionization which can be calculated by the Saha equation as a function of plasma temperature and electron number density in a LTE condition. Therefore the correction factor cannot be determined by the theory and should be evaluated under actual experimental conditions.

2.2 Low pressure laser-induced breakdown spectroscopy (LIBS)

One of the challenging targets of LIBS is the enhancement of detection limit of gas phase materials. Though the experiments have been mainly applied to direct observation of post-breakdown processes, a new method to control the LIBS plasma generation process is necessary for the enhancement of detection limit. Creation and cooling processes of plasma in LIBS can be described in detail. The core of plasma is firstly produced by the absorption of the incident laser energy, such as multi-photon ionization. The creation of the plasma core induces the rapid growth of plasma through the absorption of the laser light by electrons and the electron impact ionization process in it. After the termination of the laser pulse, the plasma continues expanding because of its high temperature and pressure gradients compared with the ambient conditions. At the same time, recombination of electrons and ions proceeds due to the collision process and temperature decreases gradually compared with that in the plasma generation process. Emission signals arise in the plasma cooling period[22]. The emission intensity from the atomized species provides information on elemental composition.

There are several interferences with target signal in LIBS process, generally including the continuum emission from plasma itself, coexisting molecular and atomic emissions, noise from detectors and so on. At high pressure, the main interference is the continuum emission from plasma itself, the intensity of which is proportional to biquadratic temperature. The temperature of plasma is also high. The generated plasma is dense and the electrons, ions and neutrals collide

frequently with each other. The temperatures of electrons, ions and neutrals become approximately same through the violent collision to transfer energy in high pressure plasma, generally called thermal plasma. At low pressure, however, the density of plasma is rather low and few opportunities to the collisions between electrons and other particles cause the large difference of kinetic energy. In this case, these particles are not in local thermodynamic equilibrium (LTE) condition. T_e, T_i and T_n are defined as the temperatures of electrons, ions and neutrals respectively, and the temperatures are in the order $T_e >> T_i$, $T_e >> T_n$, which is called cold plasma. The interference of coexisting molecular and atomic emissions appears from the products of plasma generation process. Compared with this interference, the influence of the continuum emission from plasma itself and detectors consisting of dark and shot noises are insignificant at low pressure.

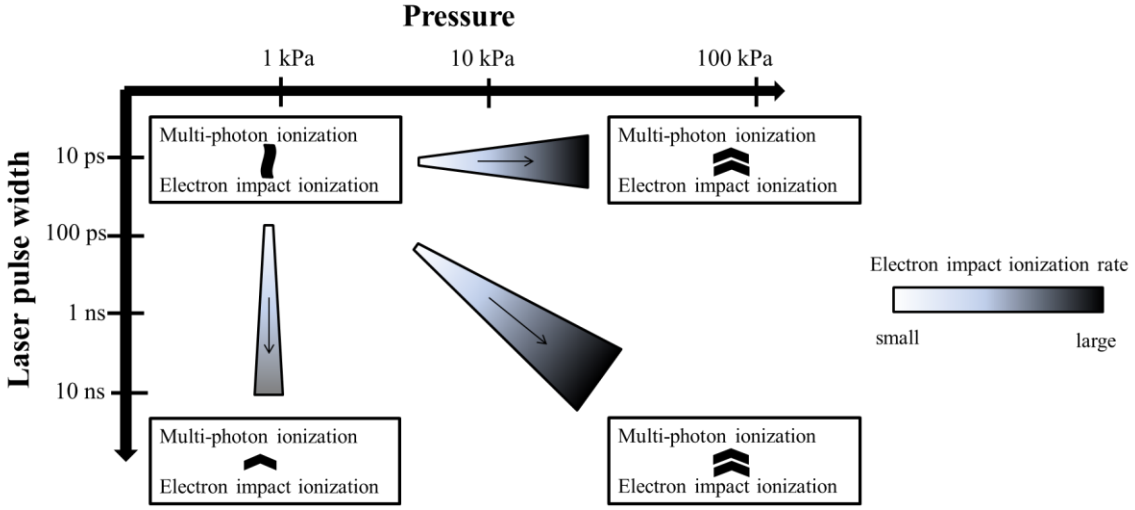

Fig. 2-2 Dominant phenomena in the laser breakdown process

Fig. 2-2 displays the dominant phenomena in the laser breakdown process as a function of pressure and laser pulse width. At high pressure the electron impact ionization becomes the major source of plasma generation. The multi-photon ionization effect appears at the low pressure and short pulse width condition. Another important strategy is the control of electron impact ionization process by the laser pulse width. Once charged particles are produced by multi-photon ionization, laser energy will be absorbed intensively and plasma grows rapidly by electron impact ionization. This plasma growth process can be controlled by using short pulse laser, such as picosecond laser.

2.3 Laser breakdown time-of-flight mass spectrometry (LB-TOFMS)

The principle behind the time-of-flight mass spectrometry (TOFMS) is illustrated in Fig. 2-3. In TOFMS system, a measurement sample is introduced into a vacuum chamber and it is atomized and ionized by laser irradiation. The action of laser irradiation on materials mainly

consists of multi-photon ionization and laser dissociation at low pressure, i.e. less than 1 Pa. The signals are distinguished and detected according to the following process of time-of-flight mass spectrometry.

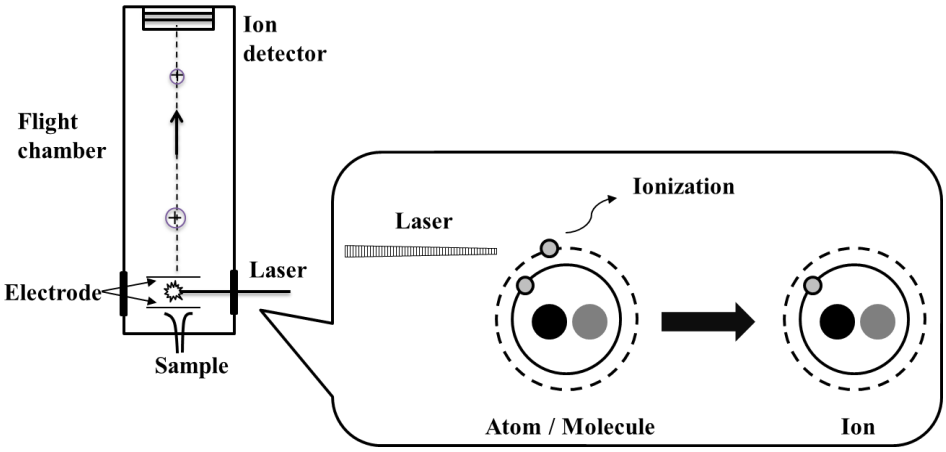

Fig. 2-3 Concept of TOFMS

The electric field potential is simultaneously applied for acceleration of ions after ion generation. The accelerated ions enter the drift region with no potential difference and undergo uniform motion. An ion detector records the signals of ionized species and ion counter takes over to digitize and display the results. Due to the law of energy conservation, the ions' electric field potential is equivalent to their kinetic energy. The following formula is established by the energy conservation law[22]:

$$zV = \frac{m}{2}\left(\frac{L}{t}\right)^2 \tag{2-8}$$

In the above expression, z is the ionic valence, V is the acceleration electric field potential, m is the ion mass, L is the ion distance of flight, t is the time of flight.

TOFMS distinguishes the ions of different atoms or molecules based on their arrival time to ion detector. The following relation between the ion mass and the time of flight can be expressed from Eq. (2-8):

$$m = \frac{2zV}{L^2}t^2 \tag{2-9}$$

TOFMS with ionization processes of laser ionization, electrospray ionization (ESI), matrix-assisted laser desorption/ionization (MALDI) and so on are the appealing technique for qualitative and quantitative analysis of atom and molecule with the features of increased sensitivity and rapid analysis. The detection limit of measured species using the technique of TOFMS with ionization process is often ppb or less. The current research focused on the measurement of trace species with heavy mass, which often compound in complex materials or

as a form of molecules. Considering the features of TOFMS, fragmentation and signal intensity are the important factors for sensitive measurement. Therefore laser breakdown is combined with TOFMS to atomize the molecules and then ionize in order to eliminate or minimize the interference of fragmentation from the coexisting materials to the atomic ion signals.

The laser breakdown processes of materials consist of laser dissociation, multi-photon ionization, electron impact ionization and so on. At low pressure, i.e. less than 1Pa, the effect of electron impact ionization is reduced significantly. The major interference in this method is partial-fragmentation and daughter ions with target atomic ion signals from the materials, which usually restricts the enhancement of its sensitivity. The feasibility to measure the trace atoms with heavy mass using laser breakdown time-of-flight mass spectrometry (LB-TOFMS) was demonstrated and the merits of the method was discussed in terms of the sensitive measurement, fast analysis and especially the efficient breakdown without interferences of partial fragmentation.

3 Experimental systems

The employed experimental systems of particles measurement using LIBS and trace species measurement using LIBS and LB-TOFMS are illustrated respectively as follows.

3.1 LIBS system for elemental detection of coal and fly ash

The objective of present experiment is to detect the size-segregated particles according to the diameter. Fig. 3-1 illustrates the experimental apparatus used in this study. The experimental set-up was composed of laser, beam focusing system, detection system, separator and auxiliary device. The beam from a Q-switched Nd:YAG laser (LOTIS TII, LS-2137U, energy stability: 2.5%, beam diameter: 8 mm) operating at 1064 nm with 6-8 ns pulse width was focused into the measurement area using the lens with focus length of 200 mm. The laser power was 30 mJ/p for unclassified particle composition measurements and 60 mJ/p for size-segregated particles. Since the samples were introduced to the measurement area using the 1.8 mm (inner diameter) stainless steel pipe, the breakdown of the particles was occurred along the laser path around the focusing point and the averaged LIBS signals were detected for the analyses. The temperature correction factors were detected and checked using the laser power between 30-60 mJ/p and different delay times from 300 ns to 3000 ns. Temperature correction factors were determined in each fly ash and coal sample. The delay time of 500 ns was used for unclassified particle composition measurements. The emission signals were separated from the laser path using a splitter and focused into an optical fiber. The spectra were dispersed using a spectrometer (JASCOCT-10S) and detected by an ICCD camera (iStar 334T Series, Andor) with the wavelength resolution of 0.072 nm/pixel, FWHM of 0.5 nm and spectral bandwidth of 65 nm. The ICCD camera consisted of 1024 × 1024 active pixels with an effective active area of 13.3 mm × 13.3 mm and was cooled to -30 ℃.

The significant device is the separator, Anderson cascade impactor. The Andersen cascade impactor employs the impacting method with multistage and porous jet nozzles and can measure the granularity distribution of aerosol according to aerodynamics. Since the method utilizes inertial impaction to classify particles by the difference of aerosol inertial force, diameter of particles gradually decreases from top down. Generally, the particle diameter for each stage can be calculated according to the density of particles and flow rate. In order to measure the particles in real time, the structure of the Andersen cascade impactor was modified. The pipe for each stage was placed in the wall of the separator to continuously separate and measure size-segregated particles with a vacuum pump.

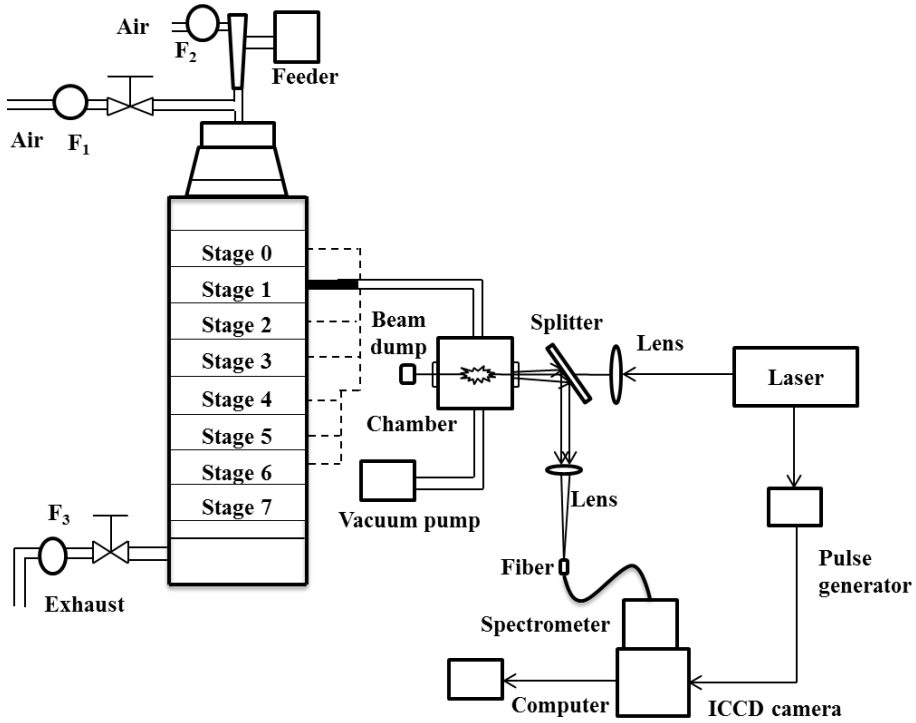

Fig.3-1 Experimental system of size-segregated particles

Three samples of Fe_2O_3 (FEO10PB, Kojundo Chemical Laboratory CO, LTD.), fly ash and coal were measured using the following procedure. The fly ash and coal (Newlands Coal) in powder form with a range of elemental composition were provided by Central Research Institute of Electric Power Industry (CRIEPI, Japan) as practical samples. According to the density of particles used in the experiment, the diameter of 50% particles for each stage was calculated, as listed in Tables 3-1, 3-2 and 3-3. The particles of Fe_2O_3, fly ash and coal were separated using the Anderson cascade impactor under the following two operation conditions. Particles were sampled from the pipe of each stage in the wall of the Anderson cascade impactor and measured continually, which is called the dynamic mode. Samples were also assembled from the collecting plate of each stage and then measured in turn, called the static mode. The signals of 100 laser shots (10 seconds) in the dynamic mode and 50 laser shots (5 seconds) in the static mode were accumulated on the CCD chip and transferred to a computer for later analyses.

Table 3-1 Experimental condition of size-segregated Fe_2O_3 sample

Stage number	Static mode Range[dp50%*] (μm)
Stage 0	4.37~ [4.37]
Stage 1	3.09~4.37 [3.09]
Stage 2	2.06~3.09 [2.06]
Stage 3	1.41~2.06 [1.41]
Stage 4	0.85~1.41 [0.85]
Stage 5	0.50~0.85 [0.50]
Stage 6	0.30~0.50 [0.30]

*dp50% is the diameter of 50% particles on each collecting plate.

Table 3-2 Experimental condition of size-segregated fly ash sample

Stage number	Dynamic mode Range (μm)	Static mode Range[dp50%] (μm)
Stage 0		6.75~ [6.75]
Stage 1	< 6.75	4.77~6.75 [4.77]
Stage 2	< 4.77	3.18~4.77 [3.18]
Stage 3	< 3.18	2.18~3.18 [2.18]
Stage 4	< 2.18	1.32~2.18 [1.32]
Stage 5	< 1.32	0.77~1.32 [0.77]
Stage 6	< 0.77	0.47~0.77 [0.47]

Table 3-3 Experimental condition of size-segregated coal sample

Stage number	Dynamic mode Range (μm)	Static mode Range[dp50%] (μm)
Stage 0		7.92~ [7.92]
Stage 1	< 7.92	5.60~7.92 [5.60]
Stage 2	< 5.60	3.73~5.60 [3.73]
Stage 3	< 3.73	2.56~3.73 [2.56]
Stage 4	< 2.56	1.54~2.56 [1.54]
Stage 5	< 1.54	0.90~1.54 [0.90]
Stage 6	< 0.90	0.55~0.90 [0.55]

Firstly, the experimental system including the Anderson cascade impactor and detectors was demonstrated by measuring the uniform sample of Fe_2O_3. Next the fly ash and coal samples were measured to get the temperature correction factors. Meanwhile, the contents of fly ash and coal samples were also analyzed using the conventional chemical analysis methods (Japanese Industrial Standards: JIS-M-8813[Coal and coke - Determination of constituents], JIS-M-8819[Coal and coke −Mechanical methods for ultimate analysis], JIS-M-8801[Coal -Testing methods] for the composition and size distribution of coal, JIS-M-8815[Methods for analysis of

coal ash and coke ash] and JIS-Z-8825[Particle size analysis−Laser diffraction methods]). Then size-segregated fly ash and coal were detected under two operation conditions, the dynamic and static modes. The composition and particle size distribution of coal and fly ash samples used in this study were shown in Table 3-4 and Fig. 3-2, respectively.

Table 3-4 Composition of coal and fly ash samples

Species	Coal (%)	Fly ash (%)
C	56.2	17.25
SiO_2	7.31	45.01
Al_2O_3	5.19	25.13
Fe_2O_3	1.05	6.17
CaO	0.54	0.75

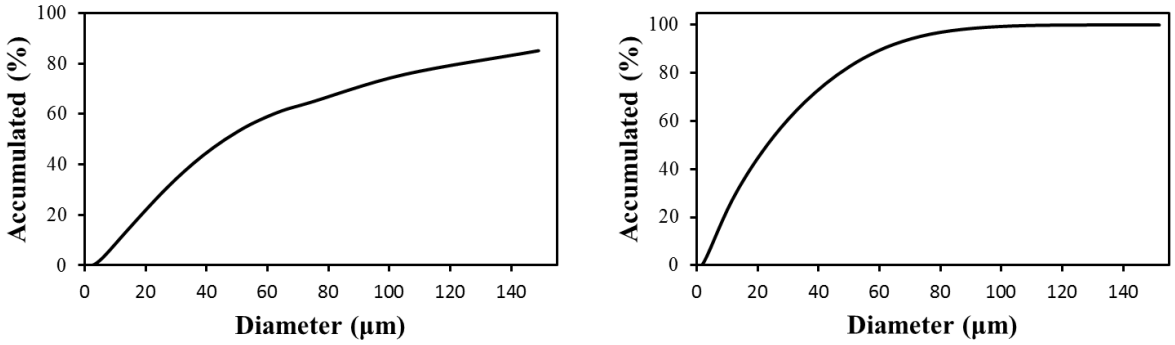

(a) Diameter distribution of coal (b) Diameter distribution of fly ash

Fig.3-2 Particle size distribution of coal and fly ash samples

Improvement on quantification of LIBS has been demonstrated in terms of plasma temperature and surrounding gas effects to further applications. Fig. 3-3 shows the experimental apparatus used with burner. The same LIBS system above was employed in the developed study. Temperature correction factors and LTE conditions were determined using a fly ash sample by the intensity ratio of the emission pair of magnesium atom as a plasma temperature indicator. The data was acquired by setting the accumulation of 10 seconds each time.

Pulverized coal (Newlands Coal) was added to combustion-supporting gas of methane and air using a feeder (Nisshin Engineering Inc. Feedcon-μ Mtype) and then introduced to the Bunsen-type burner. The flow rates of methane, air and coal were 3.9 l/min, 15.6 l/min and 0.41 g/min, respectively. A sampling pipe above the burner was employed to connect with the vacuum chamber of LIBS analyzer. The compositions of coal and fly ash used here were same as previous experiment summarized in Table 3-4.

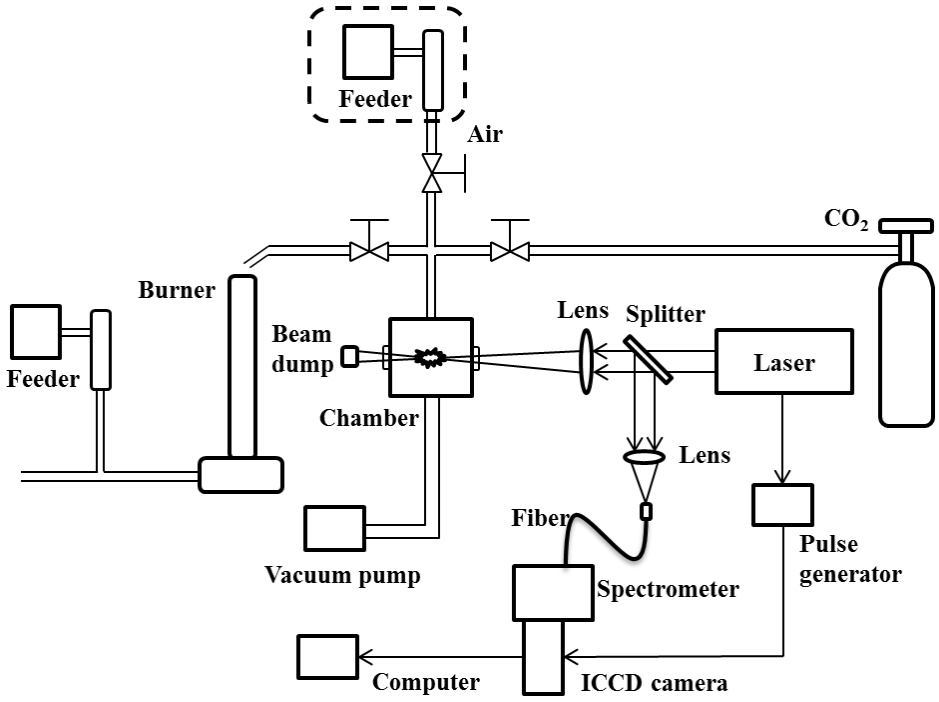

Fig. 3-3 Experimental system of particles using burner

3.2 LIBS system for the measurement of trace species

The schematic diagram of the experimental apparatus in this study is illustrated in Fig. 3-4(a). The apparatus fundamentally consisted of lasers, vacuum chamber, lens, detectors and so on. Four different pulse width lasers were used here. The parameters of nanosecond laser (Quantel Brilliant b, 6 ns, 10 Hz, beam diameter: 9 mm) output radiation were: 1064 nm and 800 mJ/p for Hg measurement. Nanosecond laser employed for iodine measurement is pulse Nd:YAG laser (Quanta-Ray Pro-230, 6-12 ns, 10 Hz, beam diameter: 9 mm) operated at fundamental radiation 1064 nm and second harmonic 532 nm with different pulse energy, respectively. The parameters of picosecond laser 1 (EKSPLA SL312, 150 ps, 10 Hz, beam diameter: 10 mm) output radiation were: 1064 nm and 150 mJ/p. The picosecond laser 2 (Quantel YG901C-10, 35 ps, 10 Hz, beam diameter: 9.5 mm) was operated at 1064 nm with power of 64 mJ/p and 66 mJ/p. The output laser beam was focused into the measurement chamber using the lens with focal length of 80 mm. The measurement chamber was a vacuum cell with four quartz windows and its internal volume was about 200 cm^3. Perpendicular to laser propagation direction, emission from another window of the chamber was focused onto the spectrometer slit. The focal length of the lens between the vacuum chamber and the spectrometer was 60 mm. Emission signals were finally detected by combination of a spectrometer (JASCOCT-10S), an ICCD camera (Princeton Instruments Inc., Model ITEA/CCD-576-S/RB-E), and auxiliary equipment. In the measurement of iodine, the iodine signal was located at vacuum UV region such as 183 nm, in which there was the effect of

O_2 absorption. Therefore N_2 was purged along the detection path from the vacuum chamber to the spectrometer, which is shown as the dashed range in Fig. 3-4(a).

The standard gas of CH_3I with concentration of 101 ppm was used and diluted by the buffer gases of N_2 and air to reduce the concentration around few ppm levels. The gaseous mixture of air and Hg was fed into the chamber from the constant-temperature bath at 370 K. The pressure was controlled with valves between the constant-temperature bath and chamber and measured with a pressure gauge (Tem-Tech Lab. SE1000-SNV-420T1) installed at the evacuation port of the chamber. The concentration of Hg was determined using a mercury gas detector tube (Komyo Rikagaku Kogyo K.K. No. 142S), sampling from the gas outlet. In the case of Hg measurement, different areas of plasma were defined to represent the central and edge signals, as shown in Fig. 3-4(b).

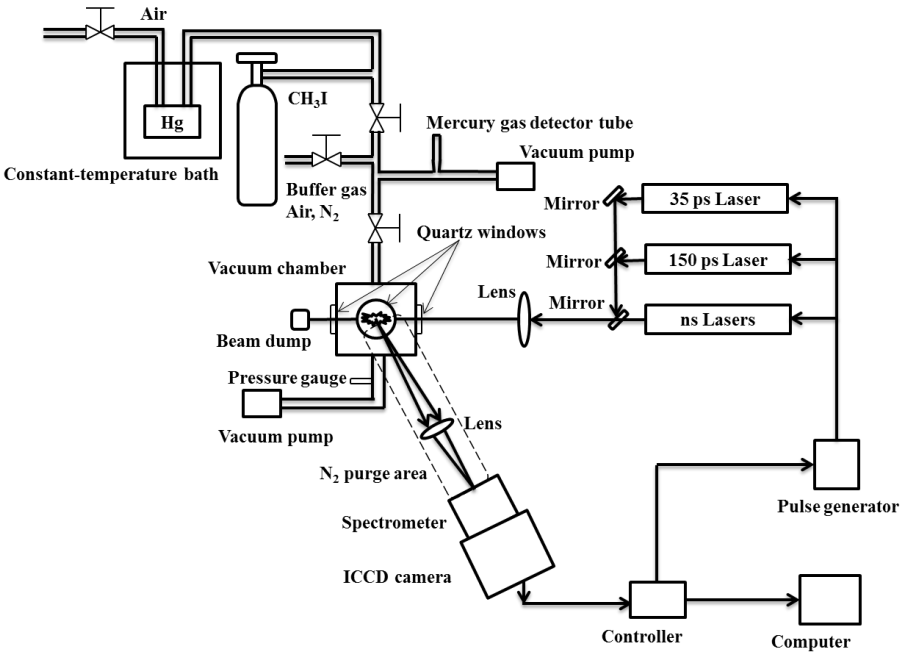

(a) Schematic diagram of the experimental apparatus

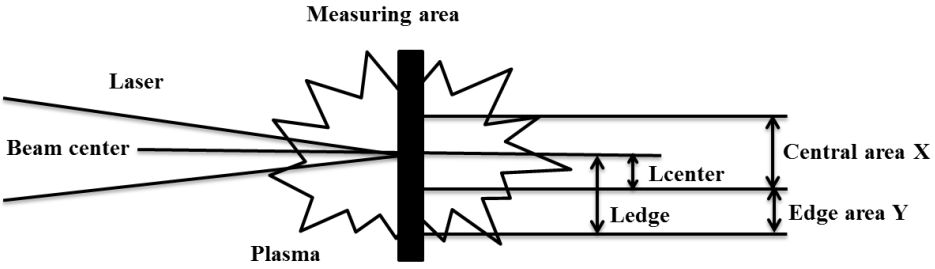

(b) The selective areas of plasma emission

Fig. 3-4 Experimental system of Hg and iodine measurements using LIBS

The verification of low pressure LIBS was extended to various trace species measurements including Hg, Sr and Cs. The schematic diagram of the experimental apparatus is illustrated in Fig. 3-5. The nanosecond laser (Quanta-Ray Pro-230, 6-12 ns, 10 Hz, beam diameter: 9 mm) was operated at 1064 nm. The fundamental apparatus has been explained above. The emission was focused onto the optical fiber employed here. Emission signals were finally detected by combination of a spectrometer (JASCO CT-10S), an ICCD camera (Princeton Instruments Inc. Model ITEA/CCD-576-S/RB-E), and auxiliary equipment. Measured trace species generally compound in various mixtures or as a form of molecules with other elements, such as hydrocarbons from exhaust in industries. In this system, there are several samples including mercury (Hg), $HgCl_2$(Kojundo Chemical Laboratory Co. $HgCl_2$), $Sr[C_5(CH_3)_5]_2$ (Kojundo Chemical Laboratory Co. Sr(C5Me5)2), and $Cs(C_{11}H_{19}O_2)$ (Kojundo Chemical Laboratory Co. Cs dpm). The gaseous mixtures of Hg, $HgCl_2$, $Sr[C_5(CH_3)_5]_2$, $Cs(C_{11}H_{19}O_2)$ with buffer gases of air or N_2 were fed into the measurement chamber from the constant-temperature bath according to the vaporizing pressure (VP). The temperatures of Hg, $HgCl_2$, $Sr[C_5(CH_3)_5]_2$ and $Cs(C_{11}H_{19}O_2)$ in the constant-temperature bath were 370 K (VP: 39 Pa), 370 K (VP: 11Pa), 420 K (VP: 2.9 Pa) and 470 K respectively. Hg concentration was determined using the mercury gas detector tube (Komyo Rikagaku Kogyo K.K. No. 142S), sampling from the gas outlet.

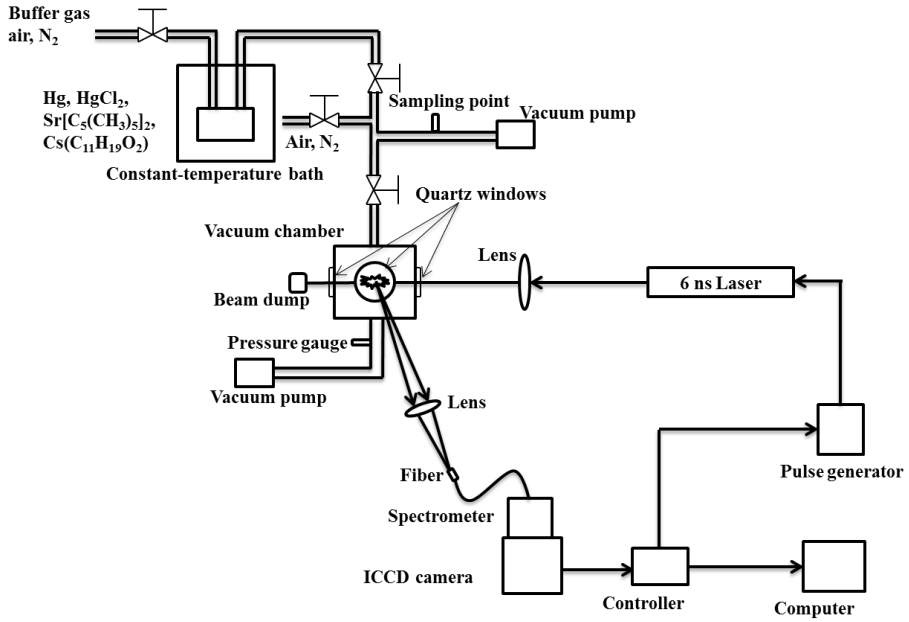

Fig. 3-5 Experimental system of various trace species measurements using LIBS

3.3 LB-TOFMS system for the measurement of trace species

These trace species were also measured using the method of laser breakdown time-of-flight mass spectrometry (LB-TOFMS). The schematic diagram of the experimental apparatus in this study is shown in Fig. 3-6(a), consisting of sample containers, lasers, jet chamber, test chamber,

flight chamber (R.M. Jordan Co., D-850 AREF; drift tube length: 500mm), ion detector (R.M. Jordan Co., 40 mm MCP Z-gap detector), ion counter (SRS, Model SR430 multi-channel scaler) and auxiliary equipment. One nanosecond laser is a pulse energy Nd:YAG laser (LOTIS TII, LS-2134UTF, 5-8 ns, 10 Hz, beam diameter: 6 mm) operated at fundamental radiation 1064 nm and fourth harmonic 266 nm. Another two nanosecond lasers employed are pulse energy Nd:YAG lasers (Quantel Brilliant b, 6 ns, 10 Hz, beam diameter: 9 mm and Quanta-Ray Pro-230, 6-12 ns, 10 Hz, beam diameter: 9 mm) operated at fundamental radiation 1064 nm and second harmonic 532 nm with different pulse energy. The picosecond laser (Quantel YG901C-10, 35 ps, 10 Hz, beam diameter: 9.5 mm) was operated at second harmonic 532 nm. The power of the lasers employed in this study was measured as an average value (energy per pulse). For the measurement of sample with heavy mass, the jet chamber was used to ensure heavy materials go straight ahead to the test chamber. The temperature of gas inlet and outlet pipes was controlled at 423 K to reduce the adhesion effects of input species. There are two turbo pumps (Pfeiffer vacuum, MVP 055-3) belonging to the test chamber and the flight chamber respectively. Pressure gauge-1 and pressure gauge-2 (Pfeiffer vacuum, PBR 260) were also installed in the test and flight chambers. The pressure gauge-3 (Pfeiffer vacuum, TPR 280) was installed between the jet chamber and the vacuum pump to measure the pressure in the jet chamber. The pressure in the test chamber is an important parameter as an indicator under different experimental conditions. The ion counter was triggered by the laser q-switch signal and operated at two detection modes. Two mass resolutions at 200 amu were employed in this experiment including 0.07 amu (5 ns resolution) for isotope measurement and 0.6 amu (40 ns resolution) for all other measurements to detect the ion signals up to 300 amu simultaneously. Ions are created between repeller plate (VA1 = +4430 V) and extraction grid (VA2 = +2900 V). During the acceleration to the flight chamber the ions pass through the Einsel lenses (no power supply is provided) and between the deflection plates (VXY1 = 0 V, VXY2 = +1871 V). At the end of the flight chamber the ions pass through the retarding grid (VR1 = +2900 V), then reflected out of the reflector assembly by the reflector grid (VR2= +4430 V). When each of these ions arrives at the detector it will impact the microchannel plate (VD= -2600 V).

The aim of our research is to clarify the breakdown patterns of hydrocarbons and its application to evaluate interferences to heavy metals, such as Cd, Hg, Pb and so on. A preliminary study is to eliminate or minimize the interference of fragmentation of molecules especially hydrocarbons to the detection of elemental compositions. Therefore the breakdown pattern dependence of hydrocarbons was analyzed by laser breakdown time-of-flight mass spectrometry using different hydrocarbons. In this system, several hydrocarbons were measured under different conditions. The influence of 1064 nm and 266 nm breakdowns was examined using a gaseous mixture of p-$C_7H_6Cl_2$, C_7H_8, $C_6H_5C_2H_3$, p-C_8H_{10}, p-$C_6H_4(C_2H_5)_2$ and $C_6H_3(CH_3)_3$. The concentration of each hydrocarbon was 1 ppm in the mixture. The method of laser breakdown time-of-flight mass spectrometry using wavelength 1064 nm and 532 nm was

also applied to various hydrocarbons, including C_2H_4, C_2H_6, C_3H_8, n-C_4H_{10} and p-C_8H_{10}. The concentrations of these standard gases in buffer gas of N_2 were 0.986%, 1.00%, 0.996%, 0.996%, and 9.78 ppm, respectively. Diluent gas of N_2 was used to reduce the concentration of the samples introduced to the jet chamber. In order to examine the detailed breakdown characteristics, p-C_8H_{10} was measured under different laser power and pressure conditions.

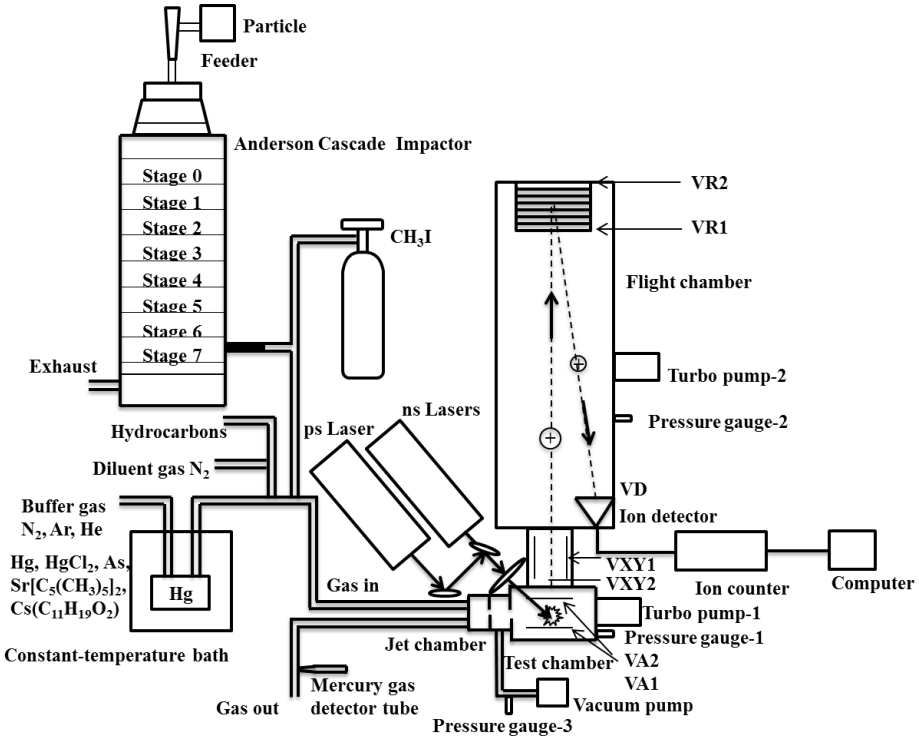

(a) Schematic diagram of the experimental apparatus

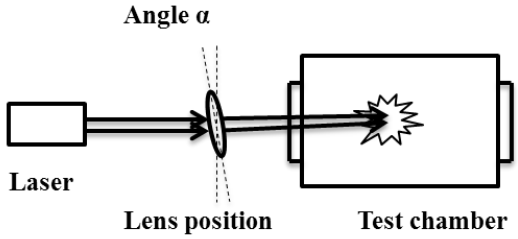

(b) Different position of the focal lens

Fig. 3-6 Experimental system of various trace species measurements using LB-TOFMS

In order to demonstrate the applicability of this method, several samples including Hg, $HgCl_2$, $Sr[C_5(CH_3)_5]_2$, $Cs(C_{11}H_{19}O_2)$, As, I_2, CH_3I, hydrocarbons and fine particles of fly ash were measured using LB-TOFMS. The chamber was purged between each measurement due to the sensitive features of TOFMS system. As for fine particles, Andersen cascade impactor (Tokyo Dylec. Corp., Model AN-200) was used to separate the particles according to particle diameter, which has been explained in section of elemental detection of coal and fly ash. The samples were

fed into the jet chamber from the constant-temperature bath according to the vaporizing temperature. For example, the gaseous mixture of Hg with buffer gas, such as N_2, Ar and He, was fed into the jet chamber from the constant-temperature bath according to the vaporizing temperature of mercury at 370 K. I_2 in the constant-temperature bath was vaporized at low temperature and introduced into the chambers. The standard gas of CH_3I with concentration of 101 ppm was also measured to demonstrate the method of laser breakdown time-of-flight mass spectrometry. Diluent gas of N_2 was used to reduce the concentration of the samples introduced to the jet chamber. The concentration of Hg was determined using the mercury gas detector tube (Komyo Rikagaku Kogyo K.K. No. 142S), sampling from the gas outlet, as shown in Fig. 3-6(a). The objective of the present experiment is to rapidly detect trace species using laser breakdown time-of-flight mass spectrometry at high sensitivity. The lasers operated at wavelengths 1064 nm, 532 nm, and 266 nm were employed to break and ionize the samples under different laser power and pressure conditions to compare the features of dissociation and ionization processes. Picosecond laser with 35 ps pulse width was also employed to enhance the detection limit. In order to improve the detection ability of this method, the focal area was enlarged by tilting the focal lens, as shown in Fig. 3-6(b). Angle α was defined to represent different position of the focal lens.

4 Coal and fly ash measurement using LIBS

The Fe_2O_3 sample was measured according to particle diameter. It was demonstrated that the experimental system has the good performance as we expected by measuring Fe_2O_3 sample under static mode. Fig. 4-1 shows the measurement results of size-segregated particles from stage 3 to stage 6. The difference of spectra of each stage was rather small because of the simplicity of Fe_2O_3 sample and similar upper energy levels of Fe around 40000 cm^{-1} between 240-290 nm, as listed in Table 4-1. The relative signal intensity was not affected by species concentration and the dependence of plasma temperature was rather small when each emission has the comparable upper energy at its emission wavelength. Therefore the similar patterns of spectra were observed from different stages.

Table 4-1 Upper energy levels of Fe

Wavelength (nm)	Upper energy (cm^{-1})
249.8	40421.85
254.1	40052.03
260.6	45294.85
261.8 ion	38858.96
263.1 ion	38660.04
275	36766.96
275.57 ion	44232.51

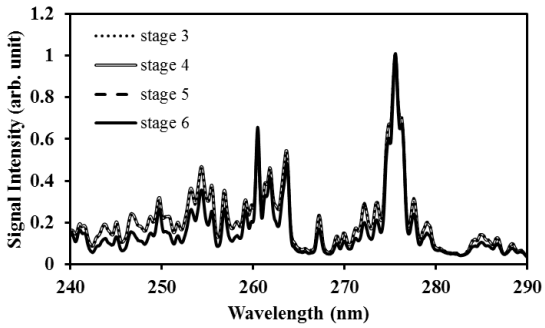

Fig. 4-1 Measurement results of size-segregated Fe_2O_3 particles from different stages

4.1 Temperature correction factors

In LIBS applications the plasma generation process contains several physical phenomena such as electron impact ionization and ion recombination, and its plasma temperature intrinsically fluctuates causing the fluctuation of evaluated concentrations from the LIBS signal intensities. Therefore the plasma temperature correction becomes important to assure the quantitative measurement, especially for the particle measurement in gases. The fly ash and coal samples were measured to set up the plasma temperature correction factors under different experimental conditions, such as detection delay time. Fig. 4-2 shows LIBS spectra of fly ash in delay time of

800 ns, 1500 ns and 3000 ns with the laser power of 30 mJ/p. These temperature correction factors were measured in each experimental condition such as fly ash and coal. The intensity concerning species concentration varied with different delay time, which means the alteration of plasma temperature. There are several Fe lines between 240-290 nm as shown in Fig. 4-1. Because of the low concentrations of Fe_2O_3 in coal and fly ash, elemental signals in coal and fly ash can be distinguished with little interference of Fe signals. Employing the detection system in this study, the emission lines with this spectral resolution can be used reasonably in the sense of signal intensities for applications such as thermal power plants[55,56]. The emission lines listed in Table 4-2 were used for the analysis of species concentration[80]. The ratio of I_{Mg1}/I_{Mg2} was used for the plasma temperature correction factor as shown in Eq. (2-3). I_{Mg1}/I_{Mg2} was altered between 4-24 by changing the delay time between 800 ns - 3000 ns. I_{Mg1}/I_{Mg2} became bigger according to the decrease of the delay time. The typical temperature correction curves between I_{Mg1}/I_{Mg2}: 4-24 and temperature corrected results of I_C/I_{Si} and I_{Fe}/I_{Si} are shown in Fig. 4-3. A fly ash sample was used in this experiment of temperature correction. It is clear from Fig. 4-3(a) and Fig. 4-3(b) the ratios are influenced by the plasma temperature, which is directly related to the ratio of I_{Mg1}/I_{Mg2}. By applying the temperature correction scheme described in Eq. (2-2)-(2-7), the fluctuation of I_C/I_{Si} and I_{Fe}/I_{Si} became smaller under different plasma temperatures conditions, i.e. I_{Mg1}/I_{Mg2}, as shown in Fig. 4-3(c) and Fig. 4-3(d). However, the plasma temperature dependencies of I_{Mg1}/I_{Mg2} are apparently different between I_{Mg1}/I_{Mg2}: 4-8, which means the low plasma temperature condition, and I_{Mg1}/I_{Mg2}: 12-24, i.e. high plasma temperature condition. This result means that the plasma induced by the LIBS process is not uniform and complex and LTE can be assumed in the limited range of plasma temperature, i.e. I_{Mg1}/I_{Mg2}. The limitation of LTE assumption has been also discussed in the glow discharge plasma[57], and the understanding of the phenomena is important for the quantitative measurement, which requires the accurate plasma correction.

Table 4-2 Upper energy levels of detection species in fly ash and coal

Species	Upper energy (cm^{-1})	Wavelength (nm)
Si	39955.05	251.6
Si	40991.88	288.2
Fe	45206.45-36766.96 (ion and atom)	274.9-275
Al	32436.8	309.27
Ca ion	56839.25	315.9
Ca ion	56839.25	318.1
C	61982.2	247.9
Mg1 ion	35760.88	279.6
Mg1 ion	35669.31	280.3
Mg2	35051.27	285.2

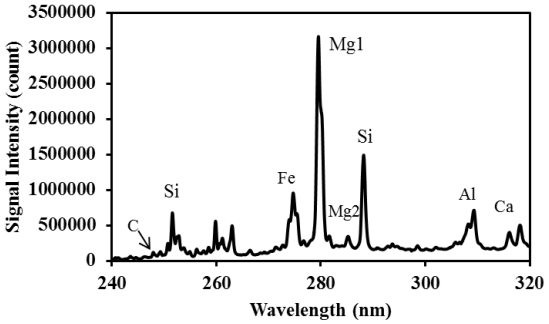

(a) Delay time: 800 ns

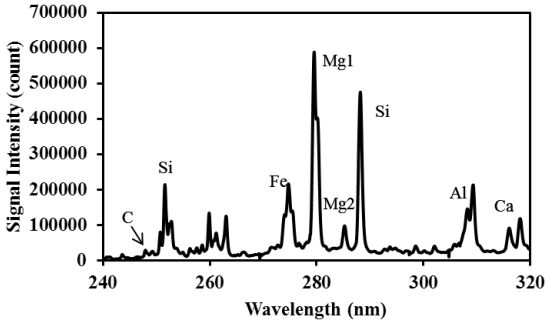

(b) Delay time: 1500 ns

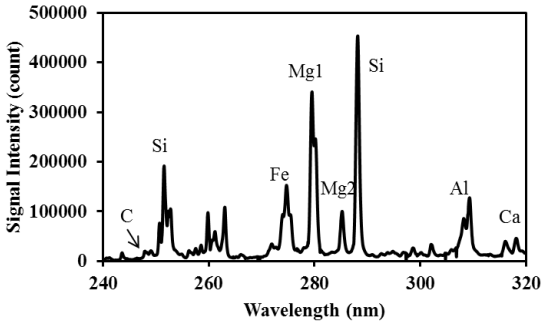

(c) Delay time: 3000 ns

Fig.4-2 LIBS spectra of fly ash with different delay time

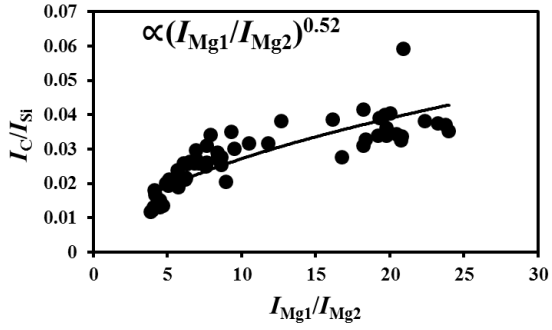

(a) Correction factor for the I_C/I_{Si} ratio

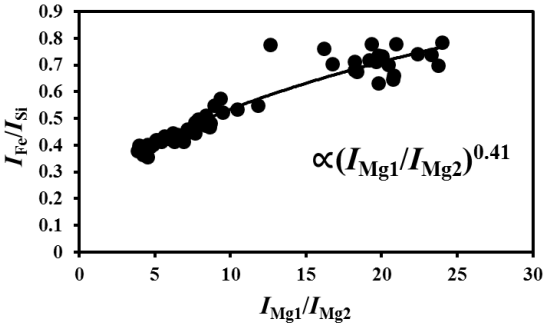

(b) Correction factor for the I_{Fe}/I_{Si} ratio

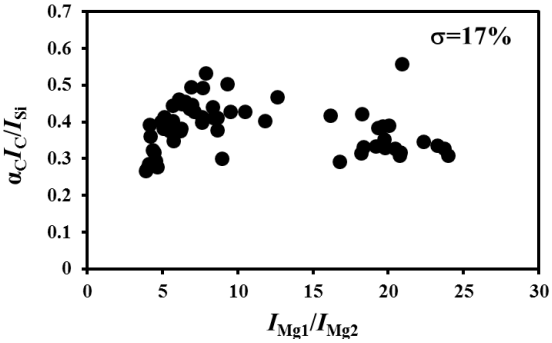

(c) Correction result for the I_C/I_{Si} ratio

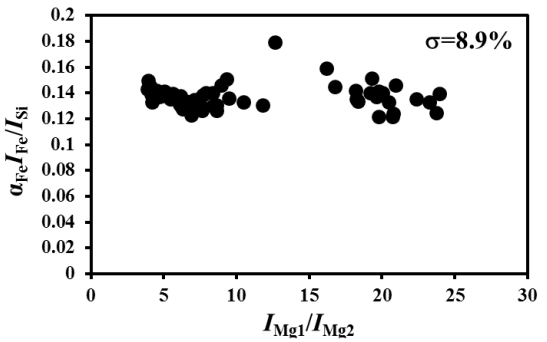

(d) Correction result for the I_{Fe}/I_{Si} ratio

Fig. 4-3 Correction curves and results of plasma temperature between I_{Mg1}/I_{Mg2}: 4-24

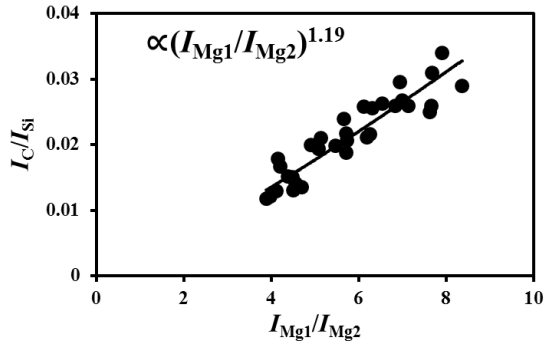

(a) Correction factor for the I_C/I_{Si} ratio

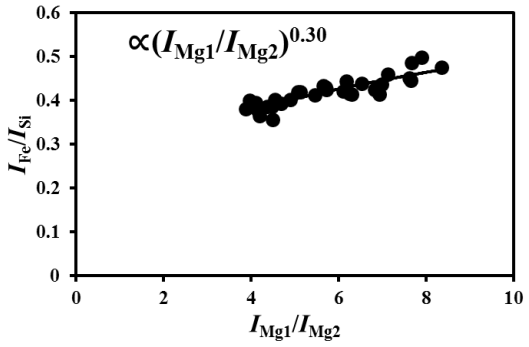

(b) Correction factor for the I_{Fe}/I_{Si} ratio

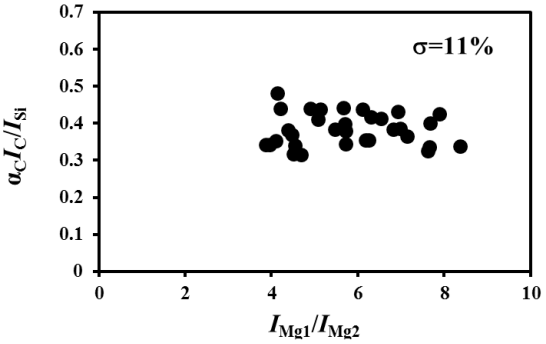

(c) Correction result for the I_C/I_{Si} ratio

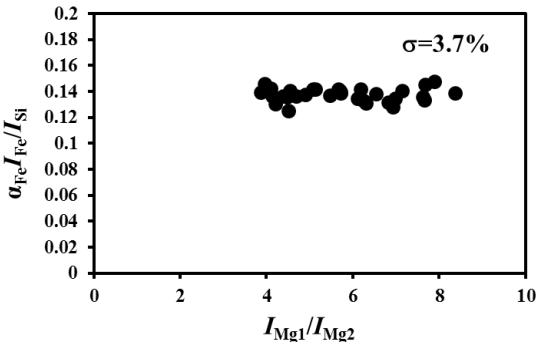

(d) Correction result for the I_{Fe}/I_{Si} ratio

Fig. 4-4 Correction curves and results of plasma temperature between I_{Mg1}/I_{Mg2}: 4-8

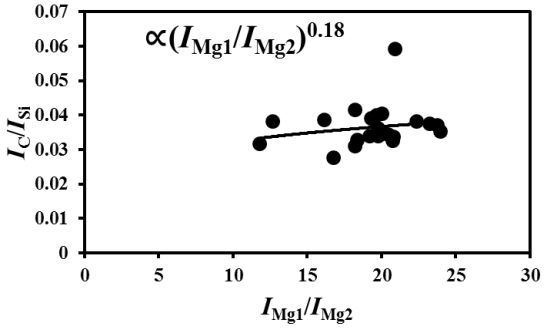

(a) Correction factor for the I_C/I_{Si} ratio

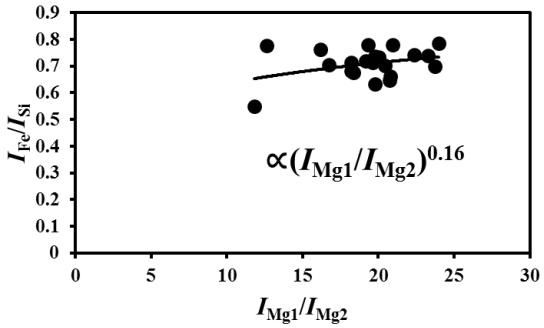

(b) Correction factor for the I_{Fe}/I_{Si} ratio

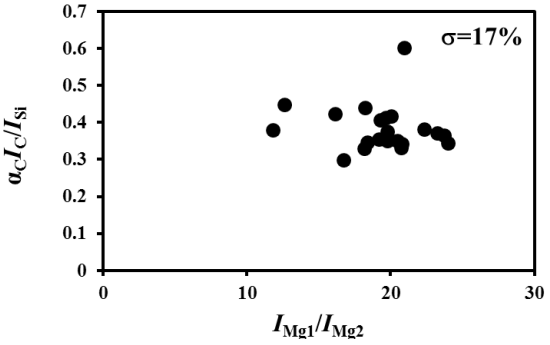

(c) Correction result for the I_C/I_{Si} ratio

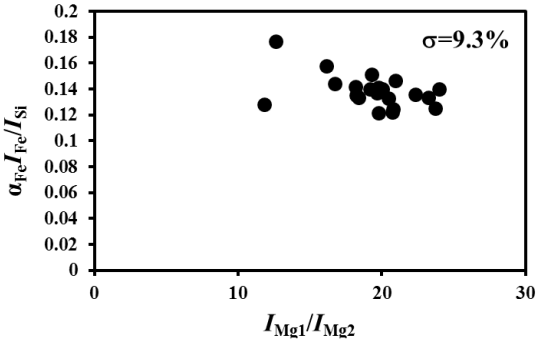

(d) Correction result for the I_{Fe}/I_{Si} ratio

Fig. 4-5 Correction curves and results of plasma temperature between I_{Mg1}/I_{Mg2}: 12-24

The temperature correction curves between I_{Mg1}/I_{Mg2}: 4-8 and temperature corrected results of I_C/I_{Si} and I_{Fe}/I_{Si} are shown in Fig. 4-4. Fig. 4-5 shows those between I_{Mg1}/I_{Mg2}: 12-24. It is clear from Fig. 4-4(a)-(b) that the correction curves are more accurate than those in Fig. 4-3(a)-(b) and Fig. 4-5(a)-(b), and $b_{i,m}$ in Eq.(2-3) takes the different values depending on the range of I_{Mg1}/I_{Mg2}, which means the limitation of LTE assumption. The fluctuation of the concentration ratios of C/SiO_2 and Fe_2O_3/SiO_2 corrected by the correction factor $b_{i,m}$ in the range of I_{Mg1}/I_{Mg2}: 4-24 are 17% and 8.9%, respectively. The fluctuation of the concentration ratios does not improve by limiting the range of I_{Mg1}/I_{Mg2}: 12-24. On the other hand the fluctuation of these ratios corrected by the correction factor $b_{i,m}$ in the range of I_{Mg1}/I_{Mg2}: 4-8 reduces to be 11% and 3.7%, respectively. The results for C/SiO_2, Al_2O_3/SiO_2, Fe_2O_3/SiO_2 and CaO/SiO_2 are summarized in Table 4-3. The correction characteristics for these concentration ratios show the same tendency as described above and it is important to set measurement condition within an appropriate I_{Mg1}/I_{Mg2} range. The cause of the fluctuation in the temperature correction results is also attributed to the sample uniformity, because the fly ash contents are not uniform in the microscopic sense. This phenomenon also appears in other species such as I_{Al}/I_{Si} and I_{Ca}/I_{Si}. Using this set of experimentally determined correction factors by choosing the appropriate I_{Mg1}/I_{Mg2} range, the fluctuation of the concentration ratios such as Fe_2O_3/SiO_2, Al_2O_3/SiO_2, CaO/SiO_2, C/SiO_2, was greatly reduced. Unburned carbon in fly ash (C content) can be evaluated down to less than 1%[56], which can satisfy the requirements in most pulverized coal fired boilers. The detection limit (S/N=1) of Fe, Al, and Ca can be estimated to be 0.1%, 0.3%, and 0.02%, respectively. The fluctuation of measured results stems from inhomogeneity of fly ash because fly ash particles consist of inhomogeneous compositions. Consistent results have also been acquired in the case of coal measurement. With temperature correction, signals became much more stable than those without plasma temperature correction.

Table 4-3 LIBS standard deviation depending on I_{Mg1}/I_{Mg2} correction range

Composition ratio	Chemical analysis	LIBS standard deviation (%) : No correction (I_{Mg1}/I_{Mg2}: 4-24)	LIBS standard deviation (%) : Corrected (I_{Mg1}/I_{Mg2}: 4-24)	LIBS standard deviation (%) : Corrected (I_{Mg1}/I_{Mg2}: 4-8)	LIBS standard deviation (%) : Corrected (I_{Mg1}/I_{Mg2}: 12-24)
C/SiO_2	0.383	34	17	11	17
Al_2O_3/SiO_2	0.558	48	20	4.9	14
Fe_2O_3/SiO_2	0.137	27	8.9	3.7	9.3
CaO/SiO_2	0.017	44	27	10	22

There are several plasma temperature correction methods such as employing the Boltzmann plot method with many emission pairs. However, considering the system simplicity and real-time measurement capability, the temperature correction method employing emission pair of I_{Mg1} and I_{Mg2} is preferable compared with others, which

demonstrated that the method is workable and satisfactory for practical applications by choosing the appropriate plasma temperature correction range.

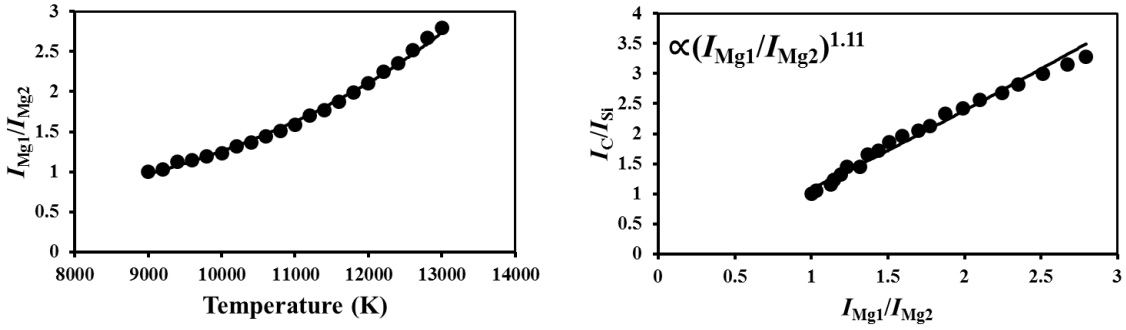

(a) Dependence of I_{Mg1}/I_{Mg2} on plasma temperature (b) Dependence of I_C/I_{Si} on I_{Mg1}/I_{Mg2}

Fig. 4-6 The dependence of intensity ratio on plasma temperature

The theoretical dependence of intensity ratio I_{Mg1}/I_{Mg2} on the plasma temperature is shown in Fig. 4-6(a)[80]. Based on the emission intensity ratio I_{Mg1}/I_{Mg2}, which is clearly related to the plasma temperature, the theoretical dependence of I_C/I_{Si} on plasma temperature is also shown in Fig. 4-6(b). In these figures I_{Mg1}/I_{Mg2} and I_C/I_{Si} were normalized at 9000 K. The result agrees with the experimental one shown in Fig. 4-3(a). According to the theory, the correction factor can be determined by the upper energy levels. When calculating the intensities, it is assumed the plasma induced by LIBS is in thermodynamic equilibrium and plasma temperature is uniform. The populations of excited levels are given by Boltzmann distribution. The ratio of ions to neutrals can be controlled by Saha equations, and an ionization temperature can be determined. In reality, the plasma induced by LIBS is non-thermodynamic equilibrium plasma and the plasma temperature is difficult to determinate due to its complexity. There are some influencing factors, such as background noise, stability of plasma, matrix effects, etc. As a result of actual complexity, several processing methods are employed to get approximate results based on the applications. However no standard method is available to determine accurate results for all kinds of plasma conditions. In this sense, our experimental results are in agreement with calculated results. The fluctuation of temperature can also be predicted according to the calculated results above. Temperature of different stages fluctuated in the range of 2000 K.

4.2 Measurement results of size-segregated fly ash

Size-segregated fly ash was detected under two operation conditions, dynamic and static modes. As introduced in experimental apparatus, there are pipes in the wall of the Anderson cascade impactor, from stage 0 to stage 6. Under dynamic mode, particles were separated and measured continuously. Here, the diameter of fly ash measured for each stage was less than that on the collecting plate from upper stage as shown in Table 3-2. For example, the diameters of fly ash on plates for stage 2 and stage 3 were 3.18 and 2.18 μm, which means the diameter of

particles from the pipe in stage 3 was less than 3.18 μm. Size-segregated fly ash was detected according to this variation tendency of diameter under dynamic mode.

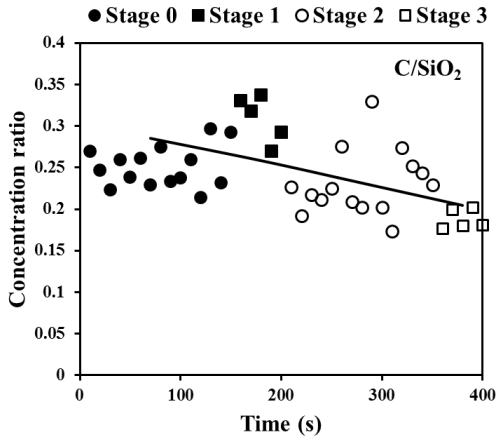

(a) Variation of concentration ratio C/SiO_2

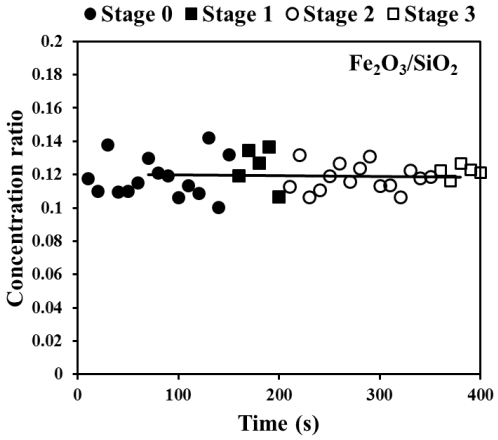

(b) Variation of concentration ratio Fe_2O_3/SiO_2

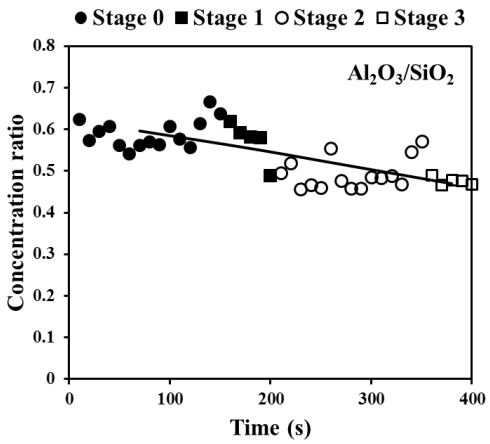

(c) Variation of concentration ratio Al_2O_3/SiO_2

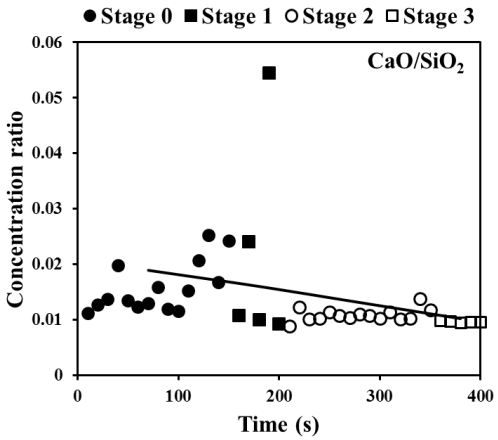

(d) Variation of concentration ratio CaO/SiO_2

Fig. 4-7 Real-time LIBS measurement results of fly ash in different stages

Fig. 4-7 shows real-time measurement results of fly ash from stage 0 to stage 3 under dynamic mode. The particles from the pipe in stage 0 were fly ash samples that had not been separated yet. At different stages, concentration ratio Fe_2O_3/SiO_2 unchanged and was stable. On the other hand, concentration ratios C/SiO_2, Al_2O_3/SiO_2 and CaO/SiO_2 decreased slightly by 2.7%, 4.2% and 0.3% according to the stage number, i.e. the decrease of particle diameter. The smaller particles combust much more adequately, resulting in lower carbon concentration in smaller particles. Because the boiling points of Ca and Al are lower than that of Fe, concentration ratios Al_2O_3/SiO_2 and CaO/SiO_2 also decreased during coal combustion, which were consistent with chemical analysis results. The standard deviations at stage 0 for C/SiO_2, Fe_2O_3/SiO_2, Al_2O_3/SiO_2

and CaO/SiO_2 were 9.9%, 10%, 5.9% and 29% respectively, and 17%, 6.7%, 7.7% and 10% at stage 2. The inhomogeneity of fly ash samples mainly caused the fluctuation of each measurement.

Variation of carbon content was apparent according to particle diameter. Furthermore, carbon content fluctuated broadly at the same stage and different measurement time because the content of carbon in fly ash was different from particle to particle. It is also demonstrated the dependence of elemental concentration on the diameter can be measured even if elemental distribution in fly ash is very complex. From this perspective, the experimental system and method can be applied for online measurement in real power plant. Variation of calcium content was also measured though the low calcium concentration (0.75%, see Table 3-4) in fly ash.

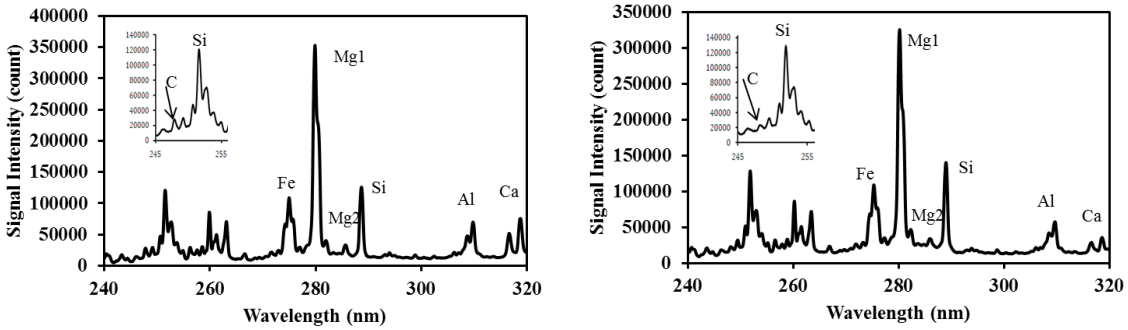

(a) Spectra of stage 1 (dp50%=4.77 μm) (b) Spectra of stage 5 (dp50%=0.77 μm)

Fig. 4-8 The measurement results of fly ash of stage 1 and stage 5

Under static mode, the fly ash was separated onto each collecting plate from stage 1 to stage 6. The diameters of 50% particles for each stage were 4.77, 3.18, 2.18, 1.32, 0.77 and 0.47 μm. The spectra of stage 1 and stage 5 are shown in Fig. 4-8. Compared with spectra of stage 1, the intensity of Al, Ca, and C signal in stage 5 decreased as the particle diameter decreased. The normalized concentration ratios of each stage to stage 1 are shown in Table 4-4 and Fig. 4-9. The concentration ratio Fe_2O_3/SiO_2 was not dependent on particle diameter and the concentration ratios C/SiO_2, Al_2O_3/SiO_2 and CaO/SiO_2 decreased with the decrease of particle diameter. These results agree with the results under dynamic mode. As shown Fig. 3-2, the amount of fly ash and coal samples decreases according to the diameter. The meaningful LIBS signal was detected up to stage 6. The fly ash employed in this study was sampled from a practical coal burner and the contents in the fly ash were inhomogeneous, especially for fine particles. Because of the sample amount and inhomogeneity, the ratios in smaller particles such as C/SiO_2 of stage 6 in Fig. 4-9 show the deviation from the tendency.

Table 4-4 Average results of LIBS measurement of fly ash

Normalized concentration ratio	Concentration ratio			
	Fe_2O_3/SiO_2	Al_2O_3/SiO_2	CaO/SiO_2	C/SiO_2
Stage 1/Stage 1	1	1	1	1
Stage 2/Stage 1	0.90	0.80	0.83	0.65
Stage 3/Stage 1	0.81	0.75	0.44	0.41
Stage 4/Stage 1	0.82	0.73	0.32	0.33
Stage 5/Stage 1	0.81	0.74	0.32	0.32
Stage 6/Stage 1	0.89	0.78	0.34	0.47

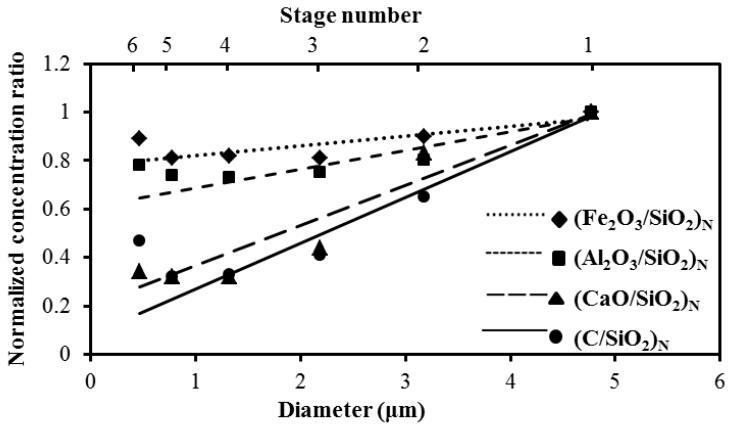

Fig. 4-9 Average results of LIBS measurement of fly ash

4.3 Measurement results of size-segregated coal

The experimental procedure and parameters were the same as the measurement of fly ash under static mode. The diameters of 50% particles for each stage were 5.60, 3.73, 2.56, 1.54, 0.90 and 0.55 μm, respectively. The spectra of stage 1 and stage 5, which indicate significant difference of C signal, are shown in Fig. 4-10. The concentration ratios of each stage normalized by those of stage 1 are shown in Table 4-5 and Fig. 4-11. Concentration ratios, Fe_2O_3/SiO_2, Al_2O_3/SiO_2, CaO/SiO_2, were similar for different stages. However, C/SiO_2 decreased when reducing the particle diameter. One reason for these results is the variation of mineral matter during coal grinding process. Coal ash particles packed in combustible components of coal are named included particles and coal ash particles expelled from combustible components are called excluded particles. During the coal grinding process, some of the mineral matter is released from the coal matrix (excluded), while some remains within the organic particles (included)[81]. It means contents of different species in fine particles are uneven. Acquired results are in good agreement with this fact. It is hereby displayed that LIBS can quantitatively measure size-segregated particles according to diameter with temperature correction method.

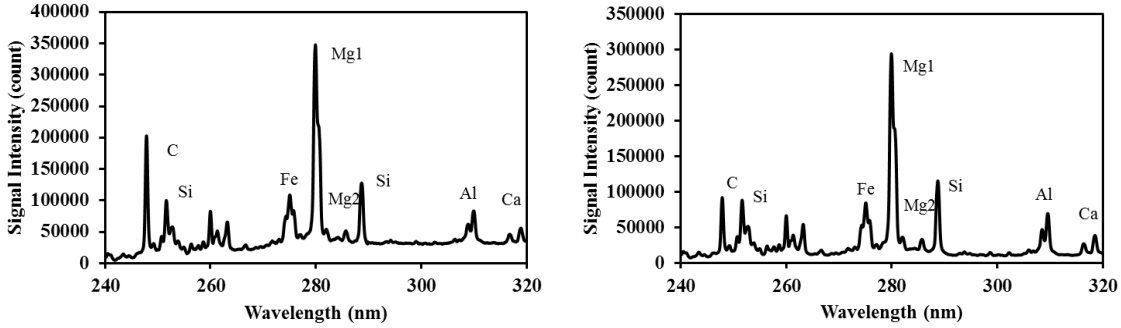

(a) Spectra of stage 1 (dp50%=5.60 μm) (b) Spectra of stage 5 (dp50%=0.90 μm)

Fig. 4-10 The measurement results of coal of stage 1 and stage 5

Table 4-5 Average results of LIBS measurement of coal

Normalized concentration ratio	Concentration ratio			
	Fe_2O_3/SiO_2	Al_2O_3/SiO_2	CaO/SiO_2	C/SiO_2
Stage 1/Stage 1	1	1	1	1
Stage 2/Stage 1	0.92	0.97	0.98	0.81
Stage 3/Stage 1	1.08	0.97	0.91	0.74
Stage 4/Stage 1	0.85	0.99	1.17	0.57
Stage 5/Stage 1	0.98	1.05	1.02	0.47
Stage 6/Stage 1	1.11	1.16	1.15	0.46

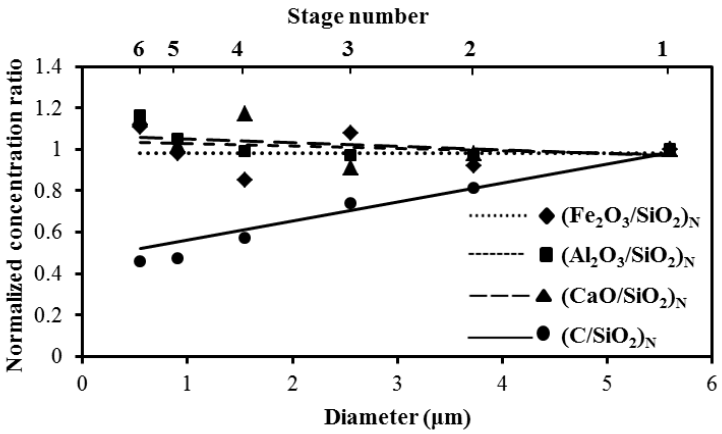

Fig. 4-11 Average results of LIBS measurement of coal

4.4 Influence of coexisting gases

In the case of fly ash measurement at actual conditions such as the real-time measurement of fly ash contents in exhausts of coal-fired boilers, influence of coexisting gases such as CO_2 must be considered to maintain the quantitative measurement of this method. In the particle contents measurement in gases using LIBS, the effects of coexisting gases become important because the gas phase materials also produce plasma

caused by the particle breakdowns. Fig. 4-12 shows the LIBS signals of burned gas from the burner without coal addition using different laser power. It is clear from Fig. 4-12(a), the burned gas was broken by the laser input in the case of 90 mJ/p laser power and the strong C signal caused by the CO_2 breakdown was detected at 247.9 nm. When reducing the laser power, the C signal became small and disappeared at 37 mJ/p laser power as shown in Fig. 4-12(b). On the other hand, when the pulverized coal was added in the fuel and the fly ash in the burned gas was measured, the signals of fly ash contents such as Si and Fe were measured along with the strong C signal as Fig. 4-13(a) shows. This C signal is mainly produced by CO_2 in burned gas and it interferes with the measurement of carbon content in fly ash. Fig. 4-13(b) shows that the C signal was also detected using the 37 mJ/p laser power in the case of the fuel with pulverized coal, though it was not detected without pulverized coal as shown in Fig. 4-12(b). This is because the particles such as fly ash became the core of the plasma and the plasma expands to the surrounding gases. The influence of coexisting gases in LIBS depends on the measurement conditions, especially the particle conditions in gases, and its effects must be evaluated in the actual measurement applications.

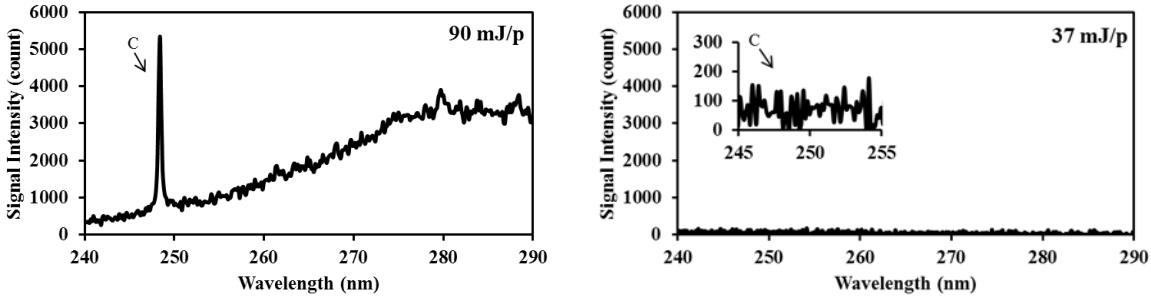

(a) Laser power: 90 mJ/p (b) Laser power: 37 mJ/p

Fig. 4-12 LIBS spectra of burned gas without pulverized coal addition

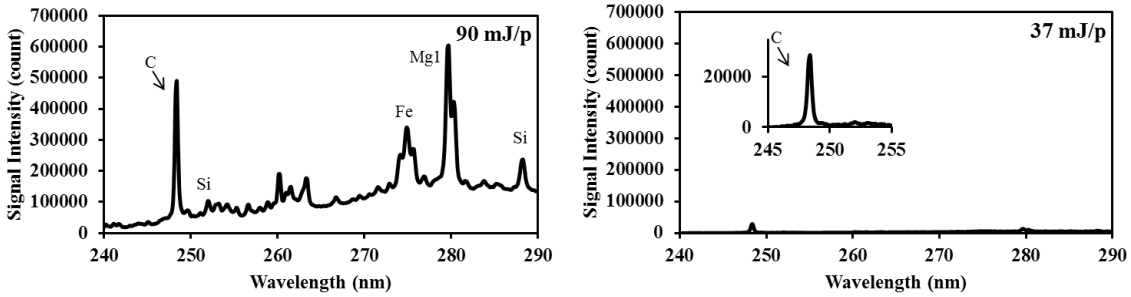

(a) Laser power: 90 mJ/p (b) Laser power: 37 mJ/p

Fig. 4-13 LIBS spectra of burned gas with pulverized coal addition

Fig. 4-14 shows the LIBS spectra of fly ash with different CO_2 concentration. In this experiment the fly ash was introduced into the measurement area with the addition of CO_2 in air. As CO_2 concentration increases, the C signal increases compared to other signals while other signal ratios such as Fe and Si remains the same. This is because the breakdown of CO_2 added in air was induced by fly ash plasma. As shown in Fig. 4-12(b) the C signal does not appear without pulverized coal addition. Fig. 4-15 shows the dependence of I_C/I_{Si} on CO_2 concentration that was measured two times at each CO_2 concentration. The CO_2 effect is rather sensitive to the concentration in surrounding gas and less than 1% CO_2 will cause the spurious C signal in fly ash LIBS spectra. The measured results also fluctuated at the conditions with CO_2 because of the unstable breakdown phenomena of CO_2 induced by fly ash. Therefore it is important to reduce the CO_2 content in burned gas when applying LIBS for unburned carbon content in fly ash under burned gas conditions. The threshold level of CO_2 depends on the measurement conditions such as the range of carbon contents and particle density. The sampling of fly ash using a cyclone used in the coal-fired power plant[56] is one of the effective methods to reduce this CO_2 effect.

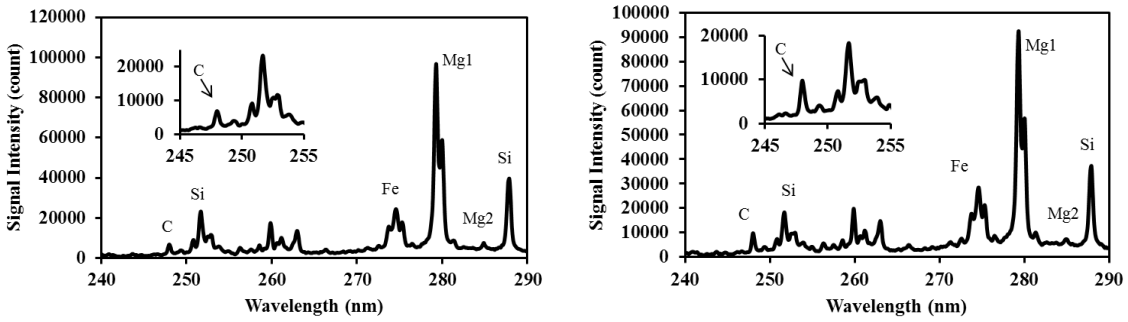

(a) CO_2: 0.84% (b) CO_2: 2.5%

Fig. 4-14 LIBS spectra of fly ash with different CO_2 concentration

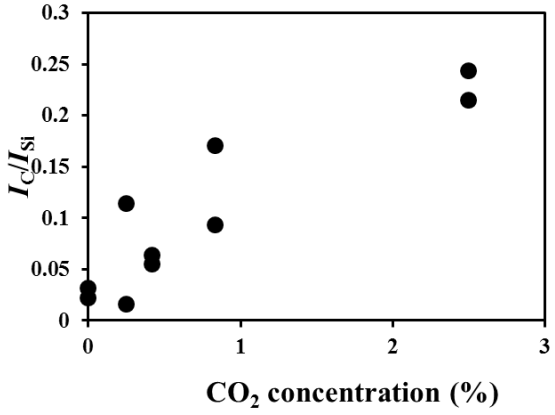

Fig. 4-15 CO_2 concentration dependence of I_C/I_{Si}

5 Trace species measurement using LIBS

5.1 Laser breakdown processes and pressure effect

Fig. 5-1 shows measured results of the gaseous mixture at 30 kPa using nanosecond (6 ns) and picosecond (150 ps) breakdowns. The emission line of Hg atom at 253.7 nm in air was difficult to distinguish from the spectra in this high pressure condition in both cases because of serious background interference of continuum emission from plasma itself. At high pressure, electron impact ionization process following multi-photon ionization strengthens the background interference besides the enhancement of Hg signal. Due to the dense plasma and high plasma-quenching rate, LIBS spectra under high pressure condition are buried in the background interference during the high plasma temperature period, and appear at rather low plasma temperature. Low pressure laser induced plasma was employed to minimize the background interference and enhance the detection limit.

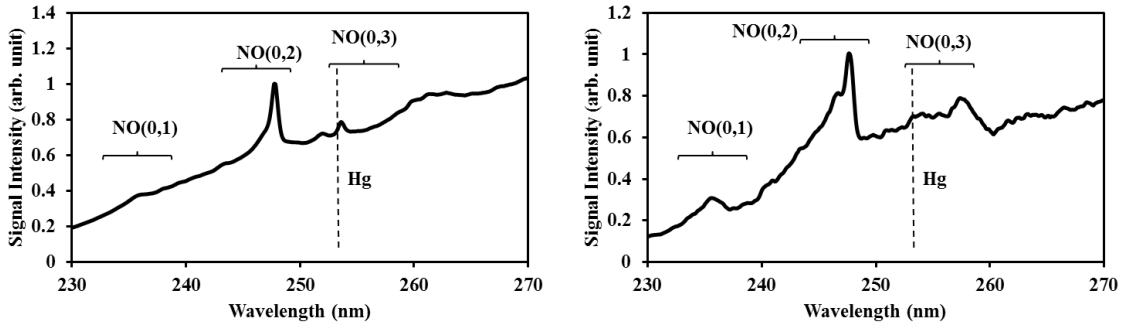

(a) 6 ns breakdown (b) 150 ps breakdown

Fig. 5-1 LIBS spectra at high pressure of 30 kPa

In LIBS process, there are several interferences with target signal, generally including continuum emission from plasma itself, coexisting molecular and atomic emissions, detectors and so on. At high pressure, the main background interference is the continuum emission from plasma itself, as shown in Fig. 5-1. In this study, low pressure laser induced plasma method was employed to reduce this background interference, which means the interference from coexisting molecular and atomic emissions became the main influencing factor under the low pressure condition. The (0,3) emission band of $A^2\Sigma \rightarrow X^2\Pi$ electronic transition of NO centered at 258 nm, which was formed during the plasma generation and cooling process of N_2 and O_2 in the air, was the interference with Hg signal. The NO formation rate is dependent on plasma temperature and more NO is produced in the plasma cooling process because of the faster reaction rate of species in plasma. The ratio of Hg signal at 253.7 nm to NO(0,3) at 258 nm (I_{Hg}/I_{NO}) was employed to evaluate the capability of low pressure and short pulse laser-induced plasma method. Here, the signal intensities I_{Hg} and I_{NO} are the Hg and NO signals of the peak height.

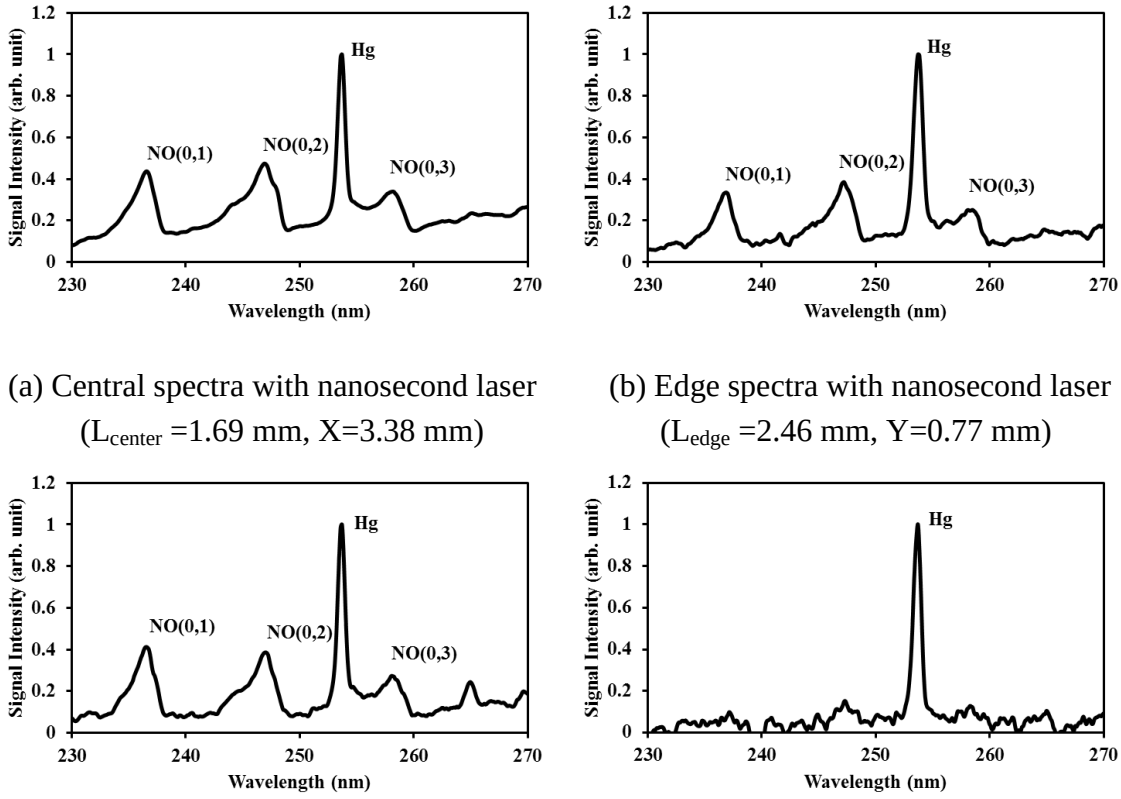

(a) Central spectra with nanosecond laser (L_{center} =1.69 mm, X=3.38 mm)

(b) Edge spectra with nanosecond laser (L_{edge} =2.46 mm, Y=0.77 mm)

(c) Central spectra with picosecond laser (L_{center} =1.125 mm, X=2.25 mm)

(d) Edge spectra with picosecond laser (L_{edge} =2.475 mm, Y=1.35 mm)

Fig. 5-2 Comparison of central and edge signals

The areas of plasma were determined as Fig. 3-4(b) shows. The range of X and Y varied from plasma under different conditions because of the different size and shape of plasma. Fig. 5-2 shows the comparison of central and edge signals between nanosecond (6 ns) and picosecond (150 ps) breakdowns at low pressure 2000 Pa. These results suggest there was no obvious variation in I_{Hg}/I_{NO} between central and edge signal in nanosecond plasma generation. On the other hand the edge I_{Hg}/I_{NO} of picosecond plasma generation was significantly higher than the center I_{Hg}/I_{NO}. This phenomenon attributes to the plasma expansion, that is, the plasma expansion characteristics vary with laser pulse width. The plasma induced by picosecond laser was much smaller and the edge of plasma becomes thermally non-equilibrium due to the rapid plasma expansion process. NO emission was not strong comparing to Hg emission at the edge of plasma because of this non-equilibrium effect, resulting in the increase of I_{Hg}/I_{NO}.

Comparing the measurement results at different pressure, the signal of Hg at 253.7 nm was distinguished obviously with the high signal intensity at low pressure. The interference of the continuum emission from plasma itself can be reduced dramatically under reducing pressure conditions. Fig. 5-3 shows the measurement results of Hg, CH_3I, $Sr[C_5(CH_3)_5]_2$ and $Cs(C_{11}H_{19}O_2)$ in the buffer gas of N_2 under low pressure condition. The apparent signals of Hg at 253.7 nm,

iodine at 183 nm (I-3), Sr at 460.7 nm and Cs at 852.1 nm can be detected with little interference of continuum emission and coexisting materials. At low pressure, the temperature of plasma was low because of the control of the electron impact ionization process, resulting in the decrease of interference of continuum emission from plasma itself. Therefore low pressure LIBS (a few kPa) has been applied to measure the trace species of Hg and iodine in this study.

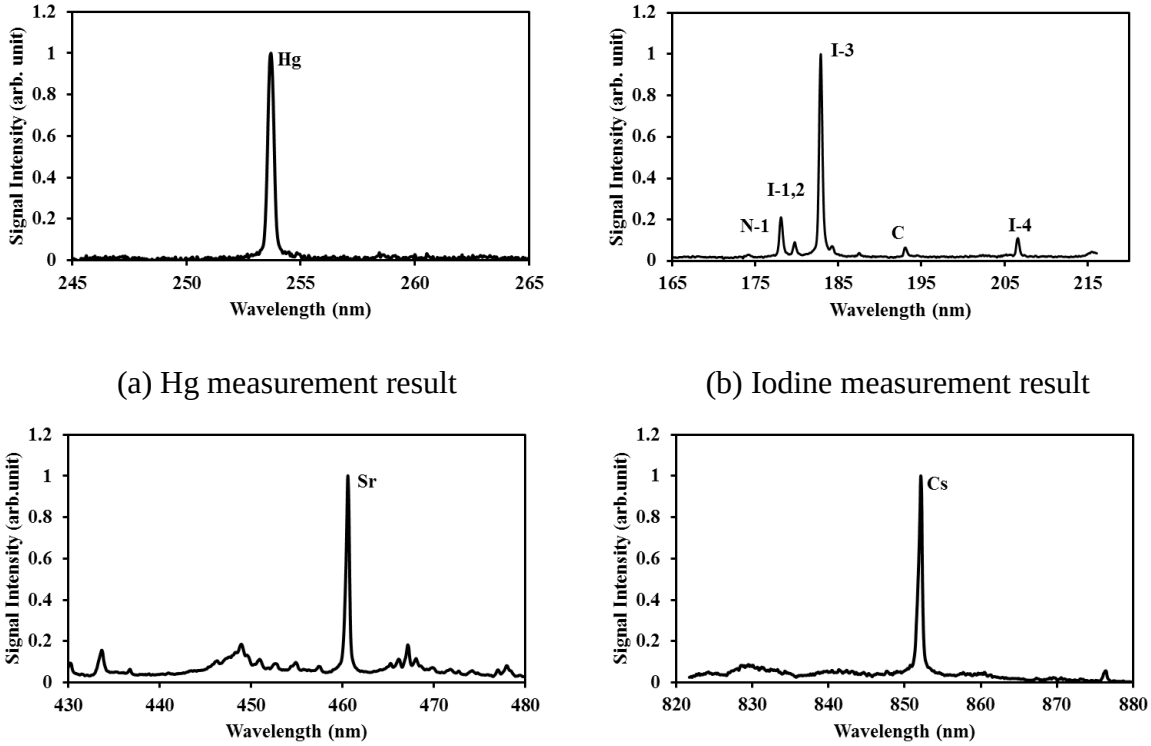

(a) Hg measurement result (b) Iodine measurement result

(c) Sr measurement result (d) Cs measurement result

Fig. 5-3 LIBS spectra of Hg, CH_3I, $Sr[C_5(CH_3)_5]_2$ and $Cs(C_{11}H_{19}O_2)$ in N_2

Trace species of Hg and iodine were measured using low pressure LIBS with 1064 nm and 532 nm breakdowns at different pressure. In LIBS detection system, the coexisting molecular and atomic emissions became the main interference when reducing the pressure. The coexisting molecular and atomic emissions in Hg detection employing air as the buffer gas are the NO emissions due to the recombination of N and O in plasma generation. In the measurement of iodine, the buffer gas was N_2 that produced N atom emissions which appear around the iodine emission wavelength region. The intensity ratios of I_{Hg}/I_{NO} and $I_{I\text{-}3}/I_{N\text{-}1}$ were defined to evaluate the emission characteristics of Hg and iodine compared with emissions (NO centered at 258 nm and N at 174.3 nm) from the buffer gases. Fig. 5-4 shows the pressure dependence of I_{Hg}/I_{NO} and $I_{I\text{-}3}/I_{N\text{-}1}$ ratios using LIBS detection system. When the pressure decreased the ratios of I_{Hg}/I_{NO} and $I_{I\text{-}3}/I_{N\text{-}1}$ increased, which indicates the influence of the coexisting materials (air and N_2) was reduced to enhance the detection ability. The electron impact ionization process was controlled when reducing the pressure. The comparison of I_{Hg}/I_{NO} and $I_{I\text{-}3}/I_{N\text{-}1}$ ratios between 532 nm and

1064 nm breakdowns at different pressure reveals higher I_{Hg}/I_{NO} and $I_{I\text{-}3}/I_{N\text{-}1}$ ratios in the case of 532 nm laser-induced plasma process because of the larger ionization and excitation for Hg and iodine atoms.

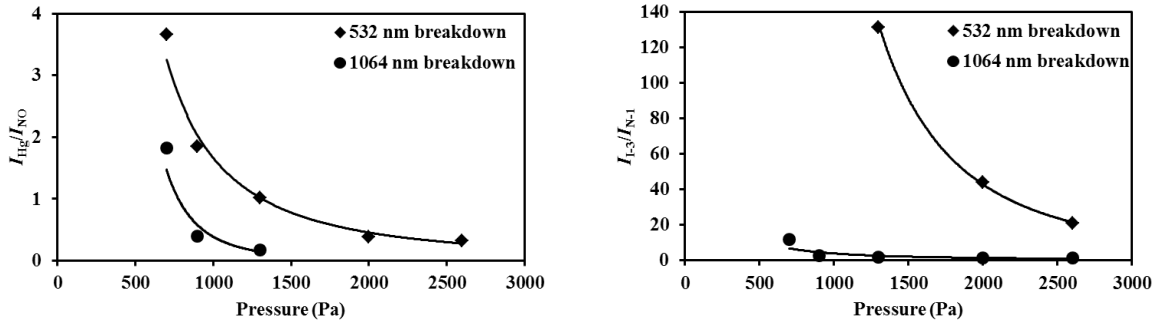

(a) The ratio of I_{Hg}/I_{NO} (b) The ratio of $I_{I\text{-}3}/I_{N\text{-}1}$

Fig. 5-4 Comparison of I_{Hg}/I_{NO} and $I_{I\text{-}3}/I_{N\text{-}1}$ ratios between 1064 nm and 532 nm breakdowns at different pressure using LIBS

5.2 Delay time and power effect on the emission signals

LIBS signals appear during the plasma cooling process, which means the atomic emissions arise after a certain time delay. Therefore, the delay time corresponding to plasma temperature is an important parameter for LIBS measurement. There is an appropriate delay time—that is, the plasma temperature—to get a maximum signal-to-noise ratio. Delay time dependence of I_{Hg}/I_{NO} and $I_{I\text{-}3}/I_{N\text{-}1}$ was measured using 1064 nm and 532 nm breakdowns, as shown in Fig. 5-5. The ratios of I_{Hg}/I_{NO} and $I_{I\text{-}3}/I_{N\text{-}1}$ were improved using 532 nm breakdown, which was consistent with the measurement results of the pressure dependence using 1064 nm and 532 nm breakdowns.

At low pressure, the delay time was not a determining factor for the I_{Hg}/I_{NO} ratio in Hg measurement because of their similar upper level energies, as shown in Fig. 5-5(a). In the case of iodine measurement using 532 nm breakdown shown in Fig. 5-5(b), $I_{I\text{-}3}/I_{N\text{-}1}$ increased when the delay time increased. In general, the density of plasma is rather low and few opportunities to the collisions between electrons and other particles cause the large difference of kinetic energy under these low pressure conditions. The particles of cold plasma are not in local thermodynamic equilibrium (LTE) condition. On the other hand, the temperature of plasma reduced as increasing the delay time, leading to the decrease of coexisting N atom emission due to the high upper level energy of N at 174.3 nm, as listed in Table 5-1. Therefore the intensity ratio of $I_{I\text{-}3}/I_{N\text{-}1}$ increased when increasing the delay time.

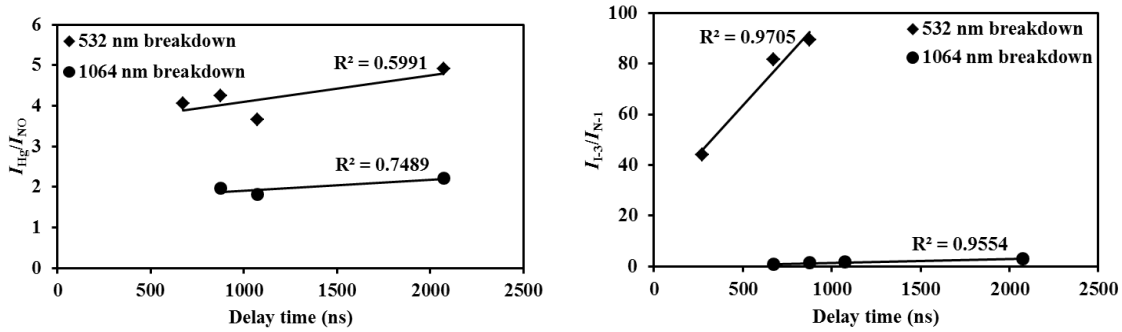

(a) The ratio of I_{Hg}/I_{NO} (b) The ratio of I_{I-3}/I_{N-1}

Fig. 5-5 Comparison of I_{Hg}/I_{NO} and I_{I-3}/I_{N-1} dependence on delay time between 1064 nm and 532 nm breakdowns using LIBS

Table 5-1 Upper level energy of measured species

Species	Wavelength (nm)	Upper level energy (cm^{-1})
Hg	253.7	39 412.2[82]
NO	258	38 759.7[83]
I-3	183	54 633.5[84]
N-1	174.3	86 220.5[85]

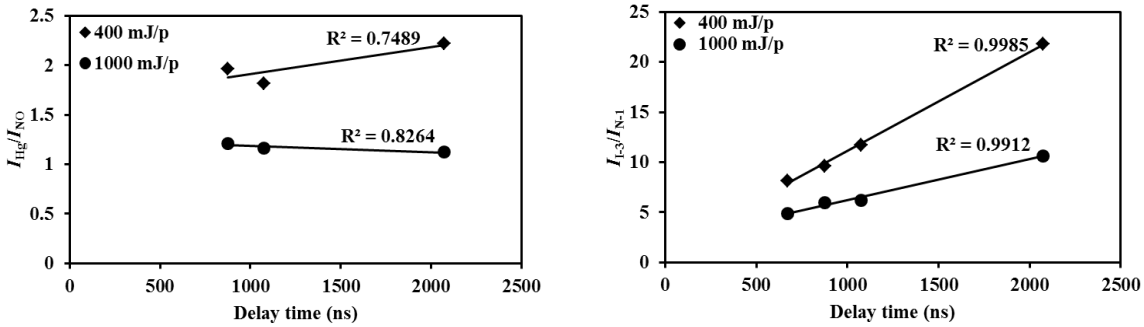

(a) The ratio of I_{Hg}/I_{NO} (b) The ratio of I_{I-3}/I_{N-1}

Fig. 5-6 Comparison of I_{Hg}/I_{NO} and I_{I-3}/I_{N-1} dependence on delay time between different laser powers

In LIBS detection system, trace species of Hg and iodine were measured in two laser power conditions. Fig. 5-6 shows the measurement results of Hg and iodine using 1064 nm breakdown with laser power of 400 mJ/p and 1000 mJ/p. These results indicate that the ratios of I_{Hg}/I_{NO} and I_{I-3}/I_{N-1} at low power of 400 mJ/p were larger than that at power of 1000 mJ/p. When the laser power increased, all the emission signals increased, especially NO and N signals due to the effect of electron impact ionization on the plenty buffer gases of air and N_2, resulting in the decrease of the ratios of I_{Hg}/I_{NO} and I_{I-3}/I_{N-1}. At the initial process of plasma generation, multi-photon

ionization was the dominant effect for Hg and iodine emission signals because of the larger ionization and excitation feature.

5.3 Pulse width effect on the emission signals

At the initial period of the LIBS process, multi-photon ionization is dominant for the plasma generation and after a certain time delay electron impact ionization becomes the influencing process. It means the electron impact ionization process can be controlled by the laser pulse width. On the other hand, the laser pulse width also affects the multi-photon ionization process. Therefore different pulse width lasers, such as nanosecond and picosecond (150 ps and 35 ps) lasers were employed to measure Hg and iodine using LIBS. Fig. 5-7 shows LIBS measurement results of Hg and iodine employing different pulse width lasers at various pressure, which shows decrease in pressure led to increase in I_{Hg}/I_{NO} and $I_{I\text{-}3}/I_{N\text{-}1}$**.** The intensity ratios were the highest in shortest pulse case at the same pressure condition, i.e. picosecond (35 ps) laser breakdown. These findings suggest that the low pressure and short pulse LIBS performs remarkable detection characteristics. Fig. 5-7(b) shows the pressure dependence of $I_{I\text{-}3}/I_{N\text{-}1}$ under different breakdown conditions. When reducing the pressure, the intensity ratio of I-3 to N-1 increased in all cases. Short pulse width and short wavelength breakdown performed improved intensity ratio of I-3 to N-1. Taking all the conditions into consideration, the reasons for the improved results were the control of the laser-induced plasma process, especially electron impact ionization process, and the larger ionization and excitation of iodine. The coexisting molecular and atomic emissions usually appear during the electron impact ionization process. The interference of coexisting atomic emission, i.e. N emission, was diminished employing short pulse width and short wavelength breakdown.

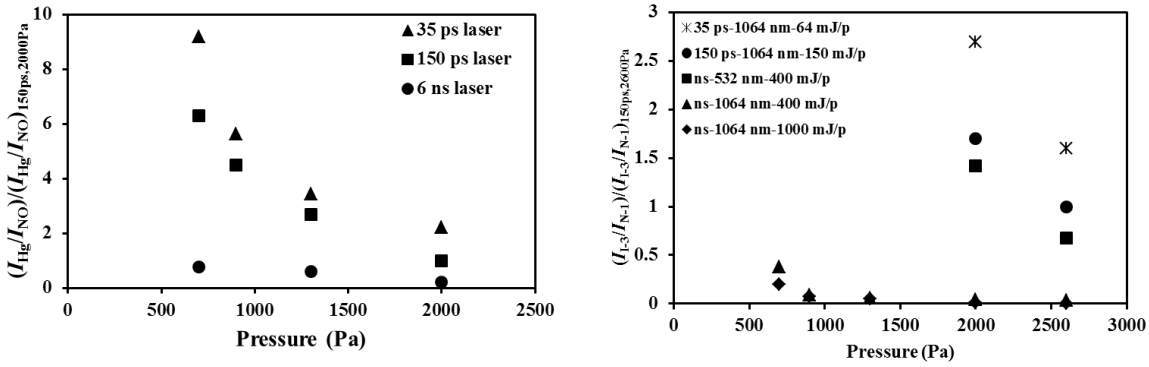

(a) The intensity ratios of I_{Hg}/I_{NO} (b) The intensity ratios of $I_{I\text{-}3}/I_{N\text{-}1}$

Fig. 5-7 Pressure dependence of I_{Hg}/I_{NO} and $I_{I\text{-}3}/I_{N\text{-}1}$ under different conditions

5.4 Buffer gas effect and their detection limits

The concentration dependence of Hg and iodine signals was measured employing different pulse width lasers. Fig. 5-8(a) and Fig. 5-8(b) show the measurement results of Hg and iodine using ns 1064 nm breakdown, which displays the linear growth.

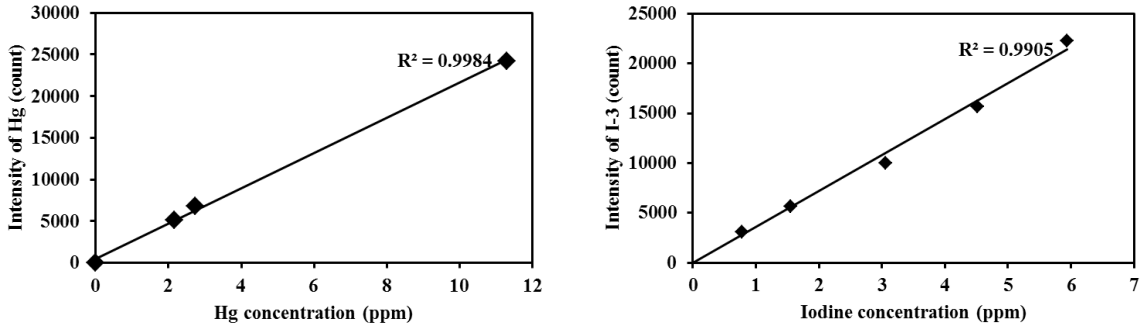

(a) Hg emission signal (b) Iodine emission signal

Fig. 5-8 Concentration dependence of Hg and iodine emission signal intensities

Different buffer gases of N_2 and air were employed in the case of elemental Hg measurement to compare the buffer gas effect on the plasma process, especially the O_2 effect. Fig. 5-9(a) and Fig. 5-9(b) show the Hg spectra in different buffer gases of N_2 and air at low pressure 2.6 kPa. Hg signal in Fig. 5-9(a) is very clear without any interference of continuum emission and coexisting N_2 effect. Employing air as the buffer gas, several signal lines including N and NO emissions were detected besides the Hg signal because of the O_2 in air. The NO emissions were formed during the plasma generation and cooling process of N_2 and O_2 in the air, which were the interference with Hg signal. The intensity of Hg signal also became weak due to the presence of O_2. Therefore the signal to background ratio reduced rapidly compared with that in buffer gas of N_2. The results can be explained by the quenching of Hg signal in O_2.

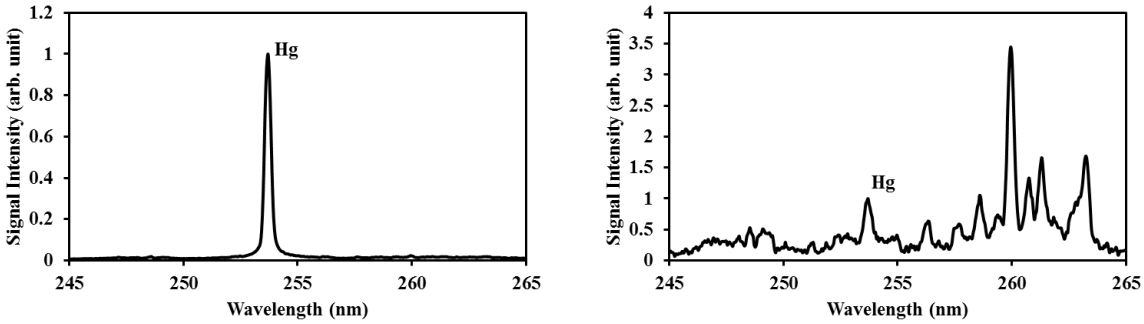

(a) Hg in N_2 (b) Hg in air

Fig. 5-9 LIBS spectra of Hg in different buffer gases

The Hg detection limit of 600 shots (1 min) was estimated in the buffer gas of N_2 and it was calculated by evaluating the ratio of the slope of the Hg calibration curve (m_s) to the background

noise (standard deviation: σ) around 253.7 nm. The detection limit of nanosecond breakdown was 3.5 ppb ($3\sigma/m_s$) at 6.6 kPa. Low pressure laser-induced plasma process was also employed to measure Hg with buffer gas of air using different pulse with lasers. The detection limit of nanosecond breakdown was 450 ppb ($3\sigma/m_s$) at 700 Pa. According to the enhancement of picosecond breakdown at low pressure, the detection limit was evaluated to be 30 ppb ($3\sigma/m_s$) in picosecond (35 ps) breakdown at 700 Pa. According to comparison of Fig. 5-9(a) and Fig. 5-9(b), these results suggest that the signal to background ratio became worse in buffer gas of air due to the quenching of Hg signal in O_2 and the NO emission effect on the background signal. In the buffer gas of air, the NO emission was reduced to enhance the detection limit using short pulse laser. However, there is no NO emission effect in the case of Hg in N_2. Therefore the detection limit was enhanced significantly by reducing the pressure to control the electron impact ionization process when employing N_2 as the buffer gas.

Iodine was also measured in buffer gas of air to evaluate the buffer gas effect at reduced pressure conditions. Fig. 5-10 shows the measurement results of iodine in air at 700 Pa using ns and 35 ps lasers operated at 1064 nm. O_2 absorption around 183 nm was not significant at such low pressure of 700 Pa inside the chamber because the absorption cross section of O_2 at 183 nm is around 10^{-21} cm^2 [86] and its effect is less than 1% according to the Beer-Lambert law. The LIBS spectra in buffer gas of air were different from that in buffer gas of N_2 because of the reduction of iodine signal by the effect of oxygen. The iodine signal (I-3) at 183 nm was reduced markedly due to the high quenching rate of excited iodine in buffer gas of air. According to the comparison of Fig. 5-10(a) and Fig. 5-10(b), the continuum emission from plasma itself was reduced when employing 35 ps breakdown, which led to the increase of signal to background ratio in the case of short pulse laser breakdown. These measurement results were consistent with those in buffer gas of N_2.

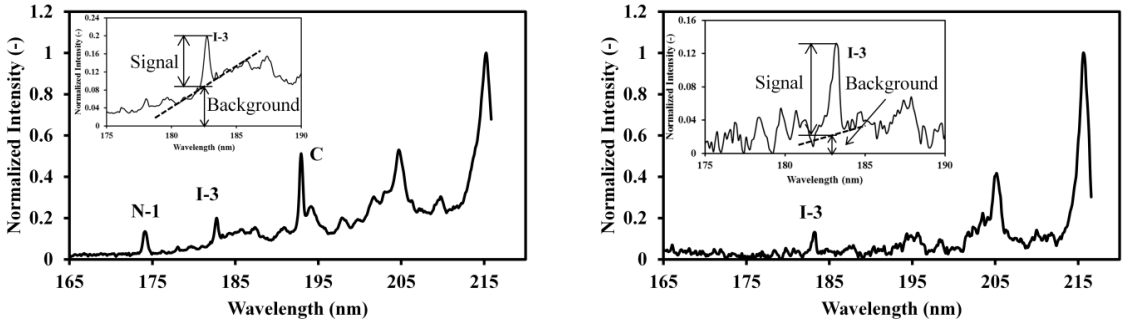

(a) ns 1064 nm breakdown (b) 35 ps 1064 nm breakdown

Fig. 5-10 LIBS spectra of iodine signal in air

According the measurement results, the detection limit can be enhanced using low pressure LIBS. As for the measurement of iodine in N_2 under low pressure condition, the iodine detection limit of 600 shots (1 min) in buffer gas of N_2 was estimated by evaluating the ratio of the slope

of the iodine signal calibration curve (m_s) to the background noise (standard deviation: σ). The iodine detection limit was 60 ppb ($3\sigma/m_s$) in nanosecond breakdown at pressure of 700 Pa. The background emission around I-3 at 183 nm was not eminent and the iodine detection limit was mainly determined by the detector noise in buffer gas of N_2. Therefore, there was not evident enhancement of iodine detection limit employing short pulse width breakdowns. The detection limit of iodine in air became worse due to the high quenching rate of excited iodine in buffer gas of air.

6 Trace species measurement using LB-TOFMS

For the purpose of detecting elemental compositions in high-mass region compounding in the complex molecules, such as hydrocarbons, laser breakdown time-of-flight mass spectrometry was applied to the mixture of hydrocarbons, i.e. p-$C_7H_6Cl_2$, C_7H_8, $C_6H_5C_2H_3$, p-C_8H_{10}, p-$C_6H_4(C_2H_5)_2$ and $C_6H_3(CH_3)_3$. Laser wavelength dependence of this method was evaluated using 1064 nm, 532 nm and 266 nm laser outputs. The mixture of hydrocarbons was used to find the preferable laser wavelength for this method as a first step. Fig. 6-1 and Fig. 6-2 show the laser breakdown mass spectra employing different wavelengths. The fragment ion signals easily become noise for the detection of target heavy atoms such as Pb, Cd, Cr, Hg, As and so on. In this method, the interference of fragment ion signals with target atomic ion signals becomes the important parameter.

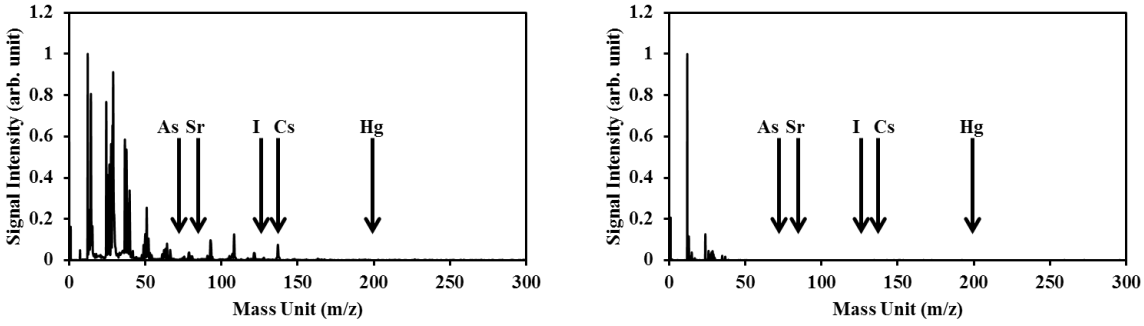

(a) 266 nm breakdown

(b) 1064 nm breakdown

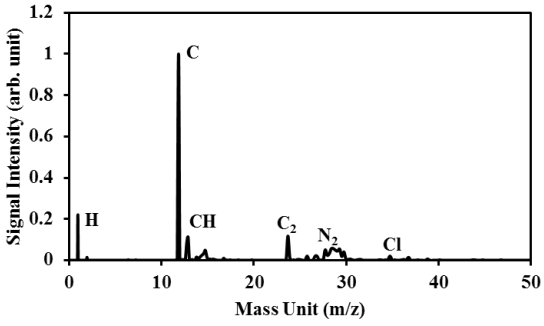

(c) 1064 nm breakdown (magnification)

Fig. 6-1 Laser breakdown mass spectra of hydrocarbons (mixture of p-$C_7H_6Cl_2$, C_7H_8, $C_6H_5C_2H_3$, p-C_8H_{10}, p-$C_6H_4(C_2H_5)_2$ and $C_6H_3(CH_3)_3$) using different wavelengths

Fragment ion signals from the hydrocarbons appear using 266 nm breakdown, as shown in Fig. 6-1(a). Laser breakdown time-of-flight mass spectrometry with wavelength 266 nm can produce partial fragmentation, especially for large fragile molecules which will be dissociated and ionized using 266 nm laser output. The target atoms, such as As, Sr, Cs and so on, can be submerged in the interference of partial fragmentation. On the other hand, it was found that the

mass spectra of atoms were detected using 1064 nm breakdown process without intermediate fragment signals in the mass region of 30-300 m/z, as shown in Fig. 6-1(b), which demonstrates that the target atoms can be easily distinguished. Fig. 6-1(c) displays the mass spectra of hydrocarbons with magnification using 1064 nm breakdown, which shows very distinct atomic ion signals, such as Cl^+, without any interference. The molecules were broken efficiently using long wavelength such as 1064 nm. According to these results, fundamental radiation 1064 nm breakdown and second harmonic 532 nm breakdown were employed to compare the breakdown characteristics of this method. Fig. 6-2(a) and Fig. 6-2(b) show the measured results of p-C_8H_{10} using 1064 nm and 532 nm breakdowns. These findings suggest the detection of trace species without any interference of fragmentations in the mass region of 30-300 m/z. The measured result of Hg and CH_3I using 532 nm breakdown is shown in Fig. 6-2(c), which indicates the legible I^+ and Hg^+ signals. There are several Hg^+ signal lines, such as 198, 199, 200, 201, 202 and 204 amu, representing the isotopes of Hg, as shown in Fig. 6-3(d). The element can be measured precisely, as the method depends on the mass of atom and molecule with high sensitivity.

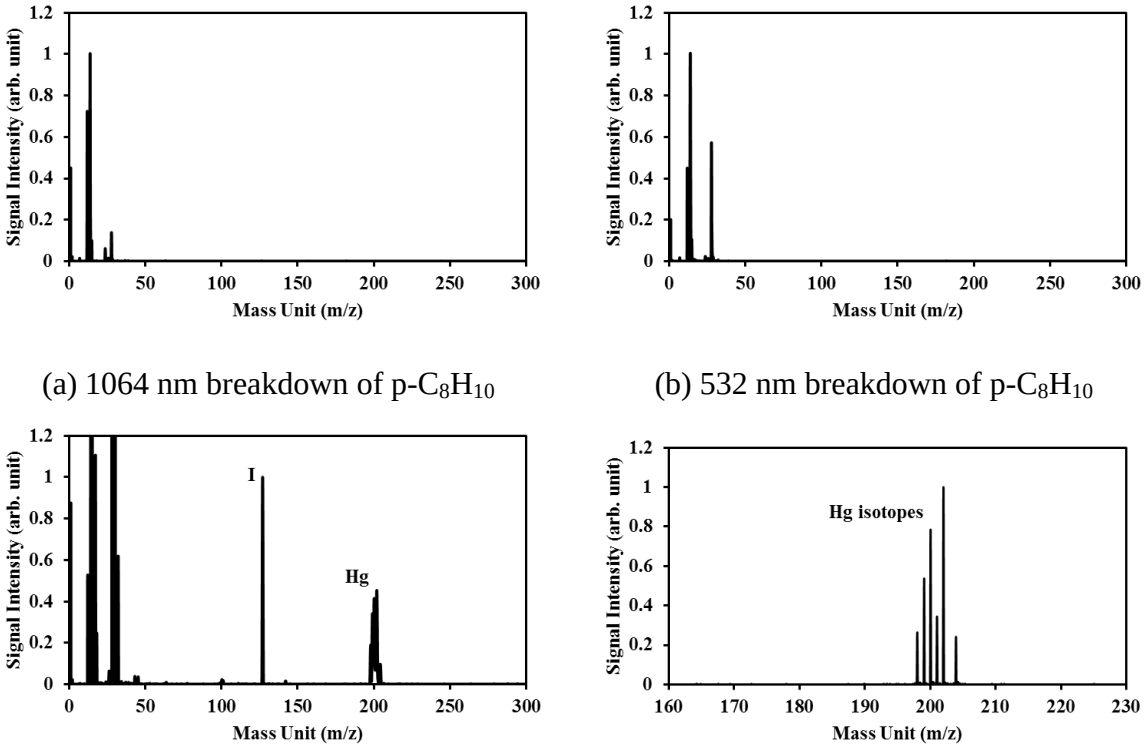

(a) 1064 nm breakdown of p-C_8H_{10}

(b) 532 nm breakdown of p-C_8H_{10}

(c) 532 nm breakdown of Hg and CH_3I

(d) Hg isotopes using 1064 nm breakdown

Fig. 6-2 Laser breakdown mass spectra using different wavelengths

As hydrocarbons contain various types of molecular structures, the energy of chemical bonds including C-C, C=C, C≡C, C-H, etc. is different from each other. Hydrocarbon molecules consisting of hydrogen, carbon and other atoms, such as chlorine and fluorine, can be broken

apart by laser irradiation, which destroys the bond between atoms. In the molecules, other atoms such as iodine (I), etc. are easily separated from the hydrocarbons because of lower bond energy than the bond energy between carbon and carbon or carbon and hydrogen. An approximate level of bond energy in hydrocarbons is shown as follows: C-C < C-H < C=C < carbon-carbon bond in a benzene ring < C≡C. It implies that the breakdown pattern will vary according the different structure of hydrocarbons.

6.1 Measurement of breakdown pattern from several hydrocarbons

The method of laser breakdown time-of-flight mass spectrometry using wavelength 1064 nm was applied to measure C_2H_4, C_2H_6, C_3H_8, n-C_4H_{10} and p-C_8H_{10} respectively under the condition of laser power 800 mJ/p and pressure 0.1 Pa. For example, Fig. 6-3 shows the different breakdown patterns of hydrocarbons including straight chain hydrocarbon of C_2H_6 and cyclic hydrocarbon of p-C_8H_{10}. Each hydrocarbon shows its characteristic breakdown mass spectra and it becomes possible to distinguish each hydrocarbon by the characteristic breakdown mass spectra. There is no fragment from hydrocarbons using long wavelength 1064 nm breakdown around 30-300 m/z. Second harmonic 532 nm breakdown was also employed to detect each hydrocarbon, which shows the different breakdown patterns of these hydrocarbons without any fragmentations around 30-300 m/z. The 1064 nm and 532 nm breakdown results of different hydrocarbons are listed in Table 6-1 and Table 6-2. Under the conditions of 1064 nm and 532 nm breakdowns, the bond energy of C-H in C_2H_4 is lower than that of C=C, therefore the ratio of atomic hydrogen (H) and carbon (C) to partial fragments, such as CH and CH_3, was high. In the case of straight chain hydrocarbons of C_2H_6, C_3H_8 and n-C_4H_{10}, the bond energy of C-H is higher than that of C-C. At the same time, when increasing the number of carbon atom, the dissociation energy of hydrocarbons will decrease and the ratio of atomic H and C to partial fragments increased. As for p-C_8H_{10}, the lower bond energy of C-H lead to the high ratio of atomic H and C to partial fragments, such as CH and CH_3.

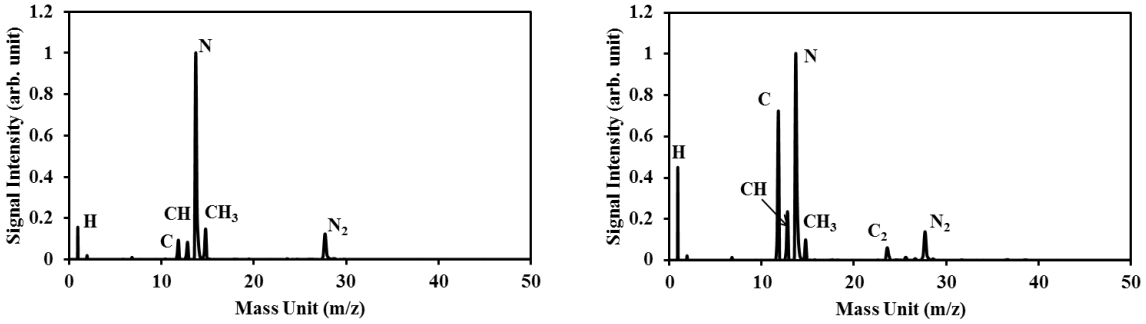

(a) Mass spectra of C_2H_6 (b) Mass spectra of p-C_8H_{10}

Fig. 6-3 1064 nm breakdown mass spectra of hydrocarbons

Table 6-1 1064 nm breakdown of different hydrocarbons

Ion	Mass (m/z)	Normalized intensity in different hydrocarbons				
		C_2H_4	C_2H_6	C_3H_8	n-C_4H_{10}	p-C_8H_{10}
H	1	0.05	0.12	0.24	0.46	0.32
H_2	2	-	0.02	0.02	0.05	0.02
C	12	0.09	0.09	0.30	0.67	0.59
CH	13	0.03	0.08	0.20	0.38	0.20
N	14	1	1	1	1	1
CH_3	15	0.02	0.14	0.31	0.24	0.08
C_2	24	-	-	0.01	0.04	0.06
C_2H_2	26	-	-	0.01	0.10	0.01
C_2H_3	27	0.01	-	0.04	0.27	0.01
N_2	28	0.12	0.13	0.11	0.12	0.13
C_2H_5	29	0.01	0.01	0.01	0.12	0.01

Table 6-2 532 nm breakdown of different hydrocarbons

Ion	Mass (m/z)	Normalized intensity in different hydrocarbons				
		C_2H_4	C_2H_6	C_3H_8	n-C_4H_{10}	p-C_8H_{10}
H	1	0.19	0.16	0.28	0.35	0.09
H_2	2	0.01	0.01	0.03	0.03	-
C	12	0.25	0.14	0.30	0.37	0.20
CH	13	0.06	0.06	0.16	0.22	0.04
N	14	1	1	1	1	1
CH_3	15	0.05	0.11	0.20	0.20	0.07
C_2	24	-	-	0.01	0.02	0.02
C_2H_2	26	0.01	-	0.04	0.09	0.01
C_2H_3	27	-	-	0.01	0.04	-
N_2	28	0.37	0.41	0.48	0.50	0.34
C_2H_5	29	0.02	0.03	0.04	0.07	0.03

In addition, the breakdown characteristics of these molecules were analyzed to evaluate the possibility of quantitative measurement. Fig. 6-4 shows the comparison between H and C atomic ratio of breakdown ion signals and molecular H and C element ratio of different hydrocarbons using 1064 nm breakdown. The ratios of H to C in p-C_8H_{10}, C_2H_4, n-C_4H_{10}, C_3H_8 and C_2H_6 molecules are 1.25, 2, 2.5, 2.67 and 3. In TOFMS system, an ion detector records the signals of ionized species and ion counter takes over to digitize and display the results by counting the number of different ions. According to the breakdown results of these hydrocarbons listed in Table 6-1 and Table 6-2, the number of H and C ions including atoms contained in fragments,

such as H, H_2, CH, CH_3, C_2H_2, and C_2H_3, was totalled to acquire the ratios of H to C. It is found that the element ratio of breakdown ion signals increases according to that of molecules. These findings demonstrate the breakdown characteristics of quantitative detection possibility of different hydrocarbons employing 1064 nm and 532 nm laser breakdown time-of-flight mass spectrometry.

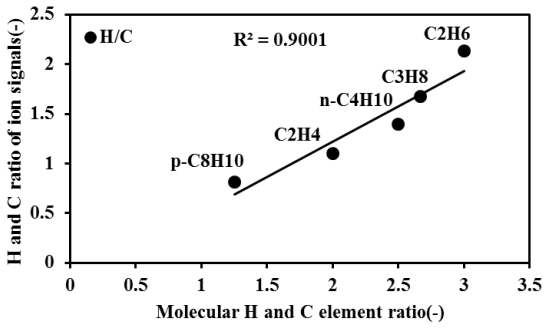

Fig. 6-4 Comparison between H and C atomic ratio of 1064 nm breakdown ion signals and molecular H and C element ratio

H and C atom yields of breakdown ion signals of these hydrocarbons were compared to p-C_8H_{10} according to the ion number of H and C atoms. Table 6-3 presents the calculated results of 1064 nm and 532 nm breakdowns. H and C yields were calculated by the number of H and C atoms divided by each hydrocarbon H and C contents (i.e. : p-C_8H_{10} : C=8, H=10). Since the H and C ion yields of p-C_8H_{10} were the highest, the H and C yields of other molecules were compared to that of p-C_8H_{10}. The H and C yields of 532 nm breakdown ion signals increased compared with that of 1064 nm breakdown due to the higher photon energy. It is demonstrated the high efficiency of 532 nm breakdown.

Table 6-3 H and C atom yields by 1064 nm and 532 nm breakdowns

Molecule	Molecular weight	H and C element ratio	H yield of breakdown ion signals compared to p-C_8H_{10}		C yield of breakdown ion signals compared to p-C_8H_{10}	
			1064 nm	532 nm	1064 nm	532 nm
p-C_8H_{10}	106	1.25	1	1	1	1
C_2H_4	28	2	0.07	0.37	0.10	0.35
n-C_4H_{10}	58	2.5	0.25	0.40	0.39	0.39
C_3H_8	44	2.67	0.17	0.42	0.25	0.44
C_2H_6	30	3	0.11	0.25	0.10	0.24

6.2 Laser power and pressure dependence of p-C_8H_{10} measurement

p-C_8H_{10} was measured under different laser power and pressure conditions to examine the detailed breakdown characteristics using 1064 nm and 532 nm breakdowns. Fig. 6-5 shows the

1064 nm breakdown mass spectra of p-C_8H_{10} in different laser power. The difference of two breakdown patterns is N and N_2 signals released from buffer gas of N_2 due to the higher laser power as shown in Fig. 6-5(b). The breakdown pattern of p-C_8H_{10} is identical and doesn't vary within this laser power range. Other hydrocarbons also showed this tendency. Fig. 6-6 shows the laser power dependence of 1064 nm breakdown C and H ion signal intensity at pressure 0.55 Pa. When increasing the laser power, the intensities of C and H ion signals present a linear growth. In the process of laser breakdown, the molecules were broken and then ionized. Laser operated at higher power can break much more molecules leading to an increase in the number density of ions. The signal intensity was enhanced by increasing the laser power. Considering the linear dependence of ion signals on laser power, the ion generation process depends on the breakdown process of hydrocarbons rather than the simple multi-photon ionization which usually shows the power-law of laser power. Power dependence of 532 nm breakdown at pressure 0.55 Pa also showed the linear relation.

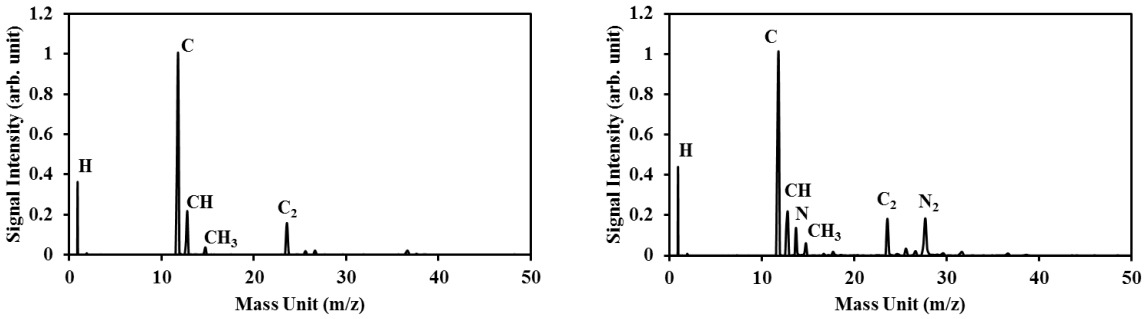

(a) Laser power: 320 mJ/p (b) Laser power: 600 mJ/p

Fig. 6-5 1064 nm breakdown mass spectra of p-C_8H_{10} in different laser power

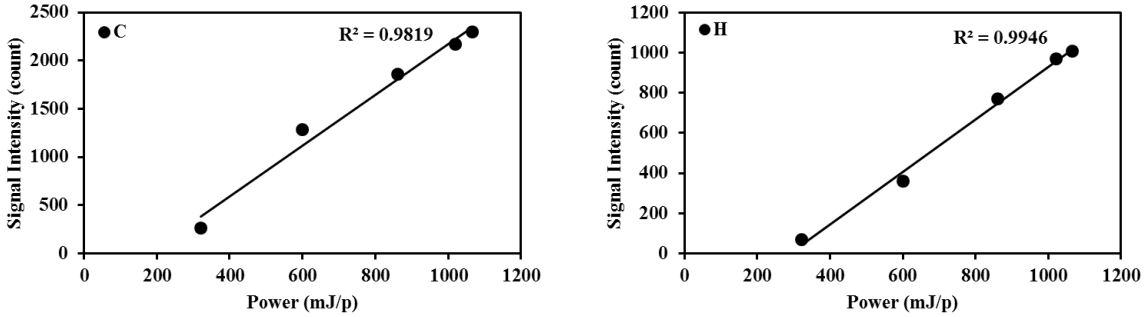

(a) Carbon ion signal (p-C_8H_{10}) (b) Hydrogen ion signal (p-C_8H_{10})

Fig. 6-6 Dependence of 1064 nm breakdown signal intensity on laser power

The influence of pressure in the test chamber on signal intensity was measured using 1064 nm breakdown. The signal intensities of C and H ions increased with an increase of pressure and it shows a nonlinear growth over 0.5 Pa. These results suggest that there is a possibility of other factors besides the direct laser-molecule interaction which influence the relation between the

pressure and the number density of ions because the ratio of N to N_2 ions was changed at high pressure, as shown in Fig. 6-7. One possible explanation for this phenomenon is that excited electrons with high energy break and ionize the molecules or radicals simultaneously at high pressure conditions. Associative effects of the pressure and the excited electrons led to the nonlinear variation. It is demonstrated that the signal intensity will be enhanced at high pressure, as well as that in the case of 532 nm breakdown.

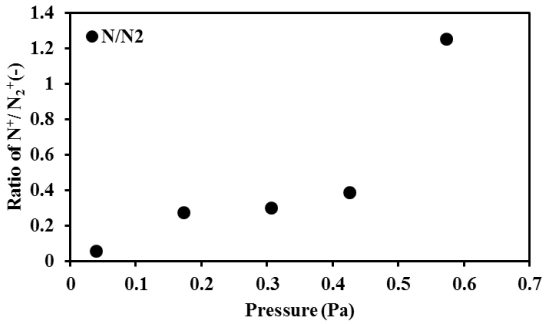

Fig. 6-7 Pressure dependence of 1064 nm breakdown of N^+/N_2^+

Diluent gas of N_2 was introduced to detect the concentration dependence of hydrocarbons using 1064 nm and 532 nm breakdowns. Fig. 6-8 shows the relation of the ion signals on their parent hydrocarbon concentration using 1064 nm breakdown including the measurement results of C, H, CH and C_2 of p-C_8H_{10} with laser power of 740 mJ/p and at pressure of 0.55 Pa. Signal intensities of C^+ and H^+ were directly proportional to the concentration of their parent hydrocarbon. Compared to C^+ and H^+, CH^+ and C_2^+ signal intensities show fluctuation from the linear relation, which is also recognized by the R^2 values of linearity (0.99, 0.99, 0.89, and 0.91) for C^+, H^+, CH^+, and C_2^+,respectively. Under this condition, the detection limit is in the range of ppb. According to the results of power dependence and pressure dependence, this detection limit will be enhanced considerably when increasing the laser power and pressure. Concentration dependence of ion signals was also detected by the measurement of p-C_8H_{10} using 532 nm breakdown. The linearity of CH^+ and C_2^+ signal intensities to the concentration of their parent hydrocarbon became better in the case of 532 nm breakdown.

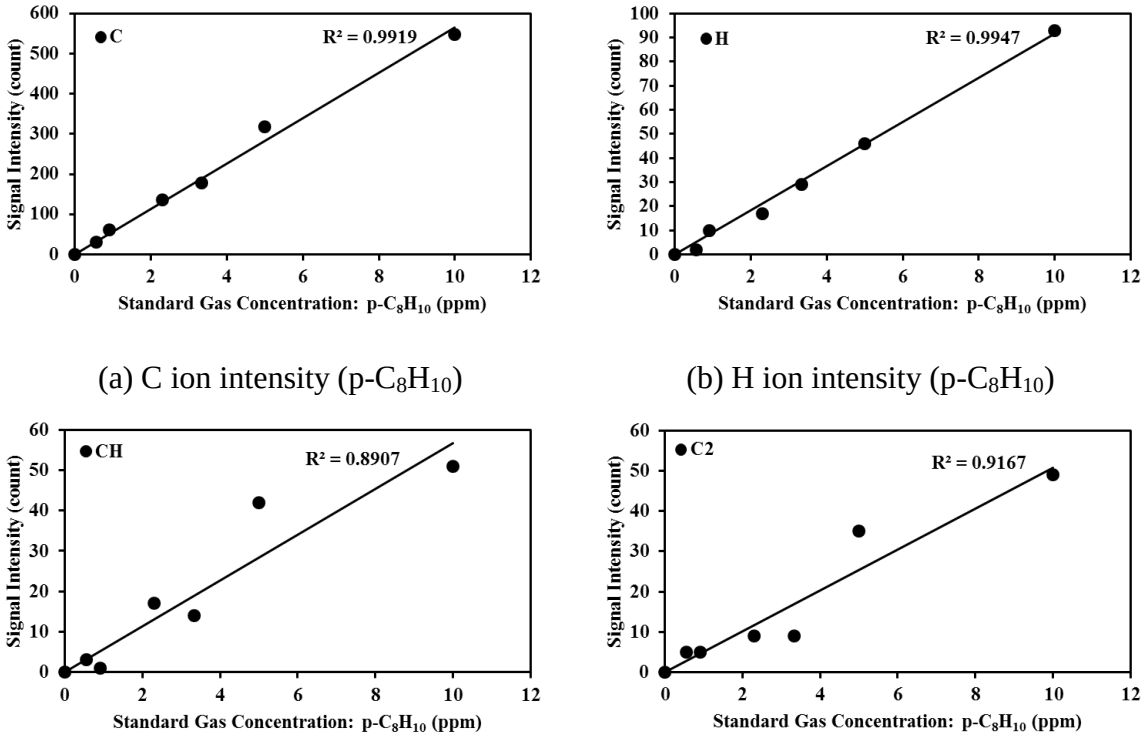

(a) C ion intensity (p-C_8H_{10}) (b) H ion intensity (p-C_8H_{10})

(c) CH ion intensity (p-C_8H_{10}) (d) C_2 ion intensity (p-C_8H_{10})

Fig. 6-8 Dependence of 1064 nm breakdown signal intensity on concentration

Laser breakdown time-of-flight mass spectrometry (LB-TOFMS) method was developed and applied for the detection of hydrocarbons in order to measure elemental compositions such as heavy metals compounding in complex molecules. This method features the rapid detection without complex sample preparation when compared with conventional methods, as well as the improved detection ability. This method was developed and applied to detect mercury and iodine in mixture.

6.3 Pressure effect on Hg and iodine ion signals

The pressure dependence of Hg^+ and I^+ signal intensity was measured according to the pressure in the test chamber. Fig. 6-9(a) shows the pressure dependence of Hg^+ signal intensity using 1064 nm and 532 nm breakdowns. The measurement results present Hg^+ signal intensity increased linearly when the pressure increased. When increasing the pressure in the test chamber, the number density of ions increases to enhance the signal intensity in both cases. Hg^+ signal intensity of 532 nm breakdown was much higher in comparison to that of 1064 nm breakdown at same pressure. In the case of 532 nm breakdown, the multi-photon ionization process is much more efficient due to the higher photon energy, which leads to the improved signal intensity at the same condition. The photon energy is 1.87×10^{-19} J/photon at 1064 nm, however the photon energy of 532 nm is double. In the pressure range of the TOFMS system, other processes such as

plasma heating phenomena by laser irradiation and electron impact ionization are less important compared to the multi-photon ionization and laser dissociation. Taking in account the comparison of Hg measurement results using different wavelengths, CH_3I was measured using 532 nm breakdown at different pressure. Fig. 6-9(b) shows the pressure dependence of I^+ signal intensity using 532 nm breakdown, which is linear in accordance with the results of Hg^+. In the case of 1064 nm breakdown reasonable signal was not able to be detected using the same laser irradiation condition as shown in Fig. 6-9(a).

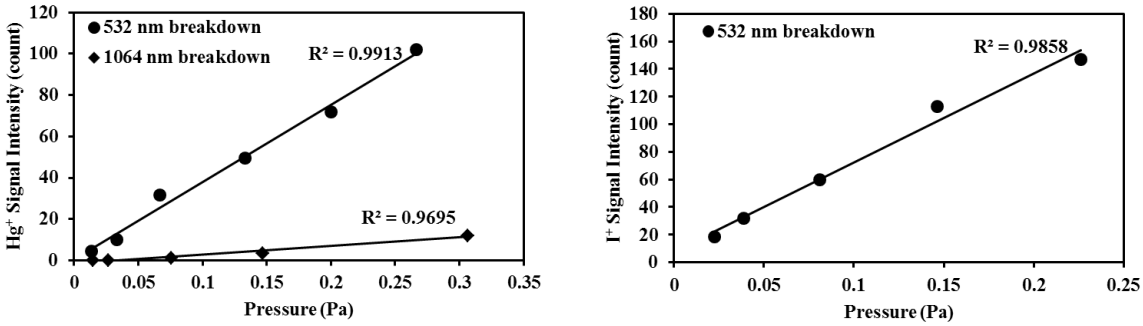

(a) Hg^+ signal (b) I^+ signal

Fig. 6-9 Dependence of Hg^+ and I^+ signal intensity on pressure in test chamber

6.4 Laser power effect on Hg and iodine ion signals

The power dependence of Hg^+ and I^+ signal intensity using 532 nm breakdown was detected at the pressure 0.15 Pa. The variations of Hg^+ and I^+ signal intensity based on the laser power are presented in Fig. 6-10 when the angle α was 0°, which means the laser beam was focused tightly into the test chamber. Hg^+ and I^+ signal intensity increases first and then decreases when increasing the laser power. According to the multi-photon ionization, the signal intensity increases as the laser power increases. Under the experimental condition, the laser power exceeding 40 mJ/p of 532 nm caused reduction of Hg^+ and I^+ signal intensity. This phenomenon may have occurred because of the recombination of Hg^+ and I^+ with electrons under high laser power condition. As increasing the laser power, more samples of N_2, Hg and CH_3I were broken and ionized to produce dense ions and electrons. Because of the high recombination rate of Hg^+ and I^+ with electrons, Hg^+ and I^+ signal intensity decreased using high laser power.

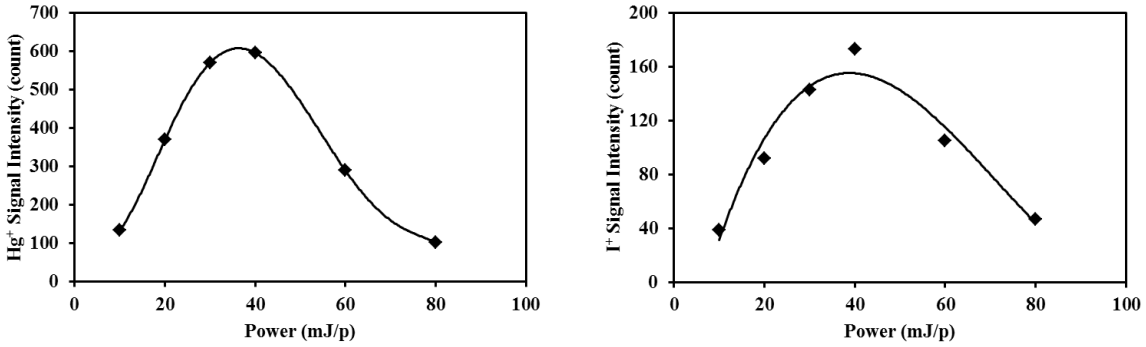

(a) Hg^+ signal (b) I^+ signal

Fig. 6-10 Dependence of Hg^+ and I^+ signal intensity on power using 532 nm breakdown when angle α was 0°

Fig. 6-11 shows the power dependence of Hg^+ and I^+ signal intensity when the angle α was 10°, which means the focal area was enlarged by titling the focal lens. The variations of Hg^+ and I^+ signal intensity based on the laser power are compatible with the results shown in Fig. 6-10, that is Hg^+ and I^+ signal intensity increases first and then decreases. When tilting the focal lens to enlarge the focal area, more samples were exposed in the laser beam with diminished laser power, resulting in reduction the densities of ions and electrons. Because of the recombination of Hg^+ and I^+ with electrons, the curves of power dependence shifted to higher laser power area. These findings suggest that the recombination rate of Hg^+ and I^+ with electrons can be reduced with appropriate focal condition. Comparing the maximum I^+ signal at different focal area, I^+ signal intensity was improved to 1.5 times when the focal area was enlarged, as shown in Fig. 6-10(b) and Fig. 6-11(b). On the other hand the maximum signal intensity of Hg^+ was kept constant at different focal area because elemental Hg ionization occurred in the narrower laser power range than that of I^+ from CH_3I.

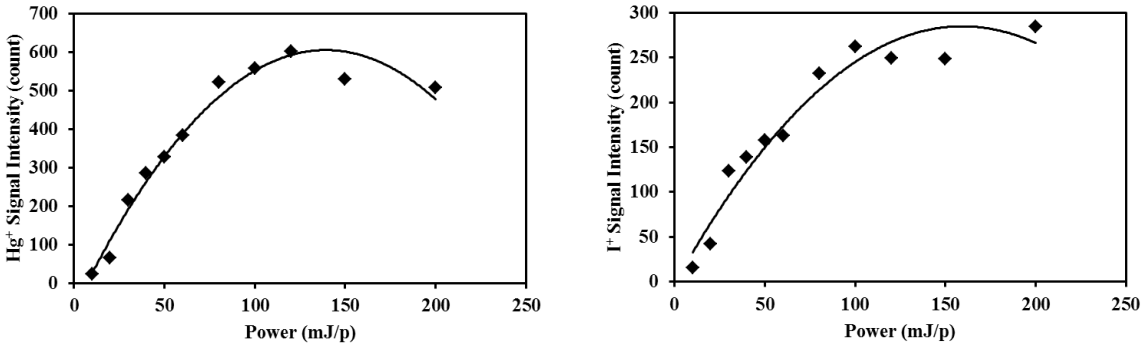

(a) Hg^+ signal (b) I^+ signal

Fig. 6-11 Dependence of Hg^+ and I^+ signal intensity on power using 532 nm breakdown when angle α was 10°

Hg with different buffer gases was introduced to the test chamber to verify the phenomenon of recombination, such as Ar and He besides N_2. Fig. 6-12 displays the dependence of Hg^+ signal intensity on the laser power employing different buffer gases. The laser power corresponding to the maximum Hg^+ signal intensity increased when using Ar as the buffer gas comparing to that in buffer gas of N_2. In the case of He, Hg^+ signal intensity just increased as the laser power increased under the experimental condition. The peak shifted due to the different recombination rate resulted from different ionization potential of N_2, Ar and He, as listed in Table 6-4. Because the ionization potential of He is the highest one among these buffer gases, the minimum He atoms can be ionized to produce electrons. Therefore the recombination rate of Hg^+ with electrons was the lowest under same laser power condition.

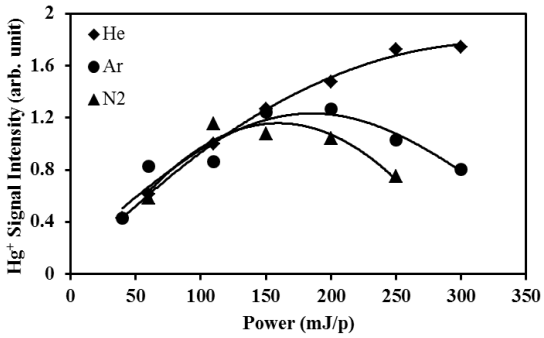

Fig. 6-12 Power dependence of Hg^+ signal intensity using 532 nm breakdown with different buffer gases

Table 6-4 Ionization potential

species	Ionization potential (eV)
Hg	10.4
N_2	15.6
N	14.5
Ar	15.8
He	24.6

6.5 Enhancement of detection limit

Analyses above indicate that the measurement results using 532 nm breakdown are much more desirable than that using 1064 nm breakdown. It is reasonable to enhance the detection limit employing the laser operated at 532 nm.

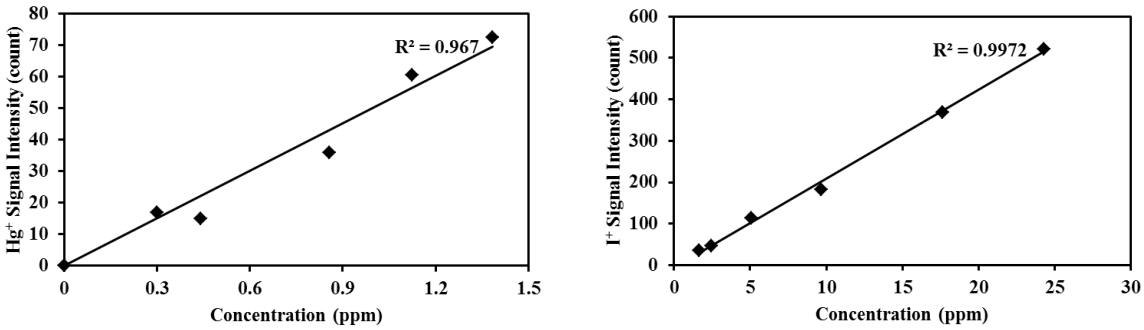

(a) Hg^+ signal (b) I^+ signal

Fig. 6-13 Concentration dependence of Hg^+ and I^+ signal intensity using 532 nm breakdown

The concentration dependence of Hg^+ and I^+ signal intensity was measured using ns 532 nm breakdown when the diluent gas of N_2 was introduced to reduce the concentration, as shown in Fig. 6-13. Hg^+ and I^+ signal intensity was directly proportional to the concentration. Hg concentration was examined using a mercury gas detector tube, sampling point as shown in Fig. 3-6(a). The concentration of CH_3I can be calculated according to the ratio of standard gas and diluent gas.

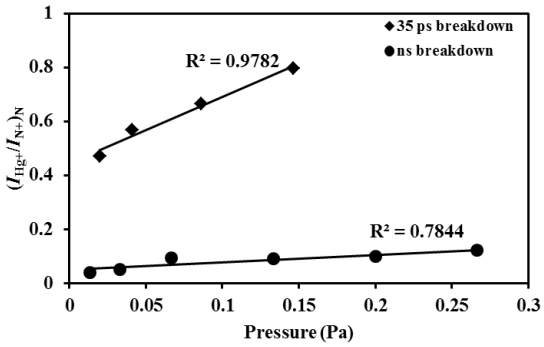

Fig. 6-14 Dependence of $(I_{Hg+}/I_{N+})_N$ on pressure using different pulse width lasers operated at 532 nm

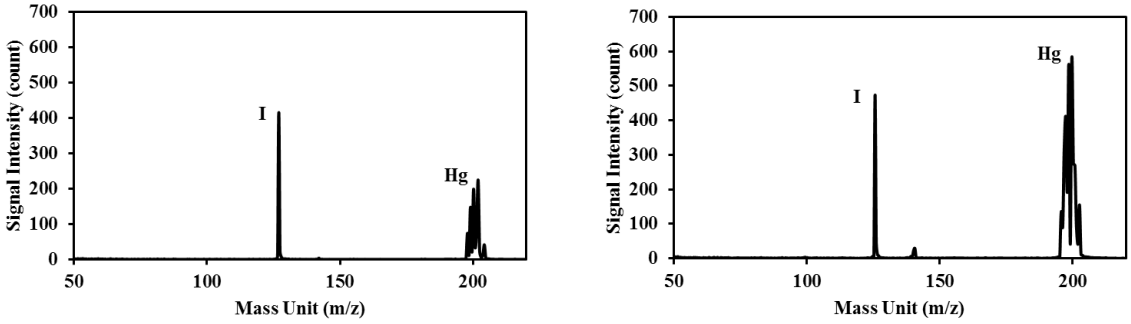

(a) ns 532 nm breakdown (b) 35 ps 532 nm breakdown

Fig. 6-15 Measured results of Hg and CH_3I using different pulse width lasers

In order to enhance the detection ability, 35 ps laser operated at 532 nm was also employed to measure Hg and CH_3I. Fig. 6-14 shows the comparison of the normalized ratio of Hg^+ to N^+ signal intensity between ns laser and 35 ps laser breakdowns operated at 532 nm under different pressure conditions. The measurement result using 35 ps laser breakdown was much more preferable than that using ns laser breakdown. The measured results of Hg^+ and I^+ mass spectra using ns laser and 35 ps laser breakdowns are shown in Fig. 6-15. The signal intensity of Hg^+ and I^+ can be enhanced 3.8 times and 1.3 times employing 35 ps laser breakdown. Taking into account the experimental conditions, the power of ns laser was 10 times higher than that of 35 ps laser. The signal intensity can be enhanced by enlarging the focal area (changing the angle α of the focal lens) and increasing the laser power. The enhancement of Hg and iodine was different because of the different breakdown features for atomic Hg and molecular CH_3I. The ion signal of CH_3I^+ (mass:142 amu) can be observed in the case of 35 ps laser breakdown. Therefore higher laser power is necessary for more efficient breakdown process. The detection limit depends mainly on the signal intensity because the background noises are the same for both ps and ns laser breakdown cases in the same conditions. The detection limit of 1200 shots (2 mins) was estimated and it was calculated by evaluating the ratio of the slope of the Hg^+ and I^+ calibration curve (m_s) to the background noise (standard deviation: σ) around 200 m/z and 127 m/z. The detection limits of Hg^+ and I^+ signals using 35 ps laser breakdown were about 0.82 ppb ($3\sigma/m_s$) and 6.18 ppb ($3\sigma/m_s$) respectively. Further enhancement will be possible by adjusting the system parameters such as laser power and breakdown area for individual atoms and introducing the resonance ionization process together with breakdown.

7 Conclusions and suggestions

7.1 Conclusions

The size-segregated particles of coal and fly ash were measured using laser-induced breakdown spectroscopy (LIBS) with the temperature correction method. With temperature correction, signals became much more stable than those without plasma temperature correction. In order to improve the accuracy of carbon content in thermal power plants, the influence of coexisting gases such as CO_2 was also detected. The trace species such as heavy metal of Hg in thermal power plants and radioactive materials of Sr, iodine and so on in nuclear power plants concerning the environment and human health were measured using low pressure LIBS and laser breakdown time-of-flight mass spectrometry (LB-TOFMS) with the features of enhanced detection limit. Major results of different measurements are shown below.

7.1.1 Elemental detection of coal and fly ash using LIBS

Contents of fly ash are important factors for the operation of coal-fired plants. LIBS technique was applied to measure contents of size-segregated particles depending on particle diameter. The plasma temperature correction method was introduced to the size-segregated fly ash and pulverized coal to detect their quantitative content information. With temperature correction, signal stability has been significantly improved. Acquired results successfully clarified the content dependence on particle diameter. Major results of fly ash and coal measurements are shown as follows.

(1) LTE was assumed in a limited range of plasma temperature in laser-induced plasma and the quantitative measurement was improved by choosing the appropriate plasma temperature range. In the case of fly ash measurement, the emission intensity ratio of Mg: I_{Mg1}/I_{Mg2} became a plasma temperature indicator and the range of I_{Mg1}/I_{Mg2}: 4-8 showed better LTE condition resulting in the accurate plasma correction compared to the range of I_{Mg1}/I_{Mg2}: 12-24.

(2) In fly ash, contents of Al, Ca, and unburned carbon decreased as decreasing the diameter but Fe was in steady content due to different behavior of these elements during coal combustion. Detected results of fly ash under dynamic mode indicate the practicability of measurement of size-segregated particles. The fluctuation of composition such as carbon content can be measured according to the particle diameter. It is helpful to obtain the detailed and timely information in real power plants, which cannot be acquired using a conventional method during coal combustion.

(3) The measured results of coal show the contents of Fe, Al and Ca were almost constant in coal particles with different diameters. However, the carbon content decreased when the diameter decreased, which display a good agreement with actual situation of coal and further support the reasonableness of this method.

(4) In the measurement of fly ash contents, CO_2 causes the spurious C signal in fly ash LIBS spectra. The CO_2 effect is rather sensitive to the concentration in surrounding gas and less than 1% CO_2 will cause the spurious C signal. It becomes important to reduce the CO_2 content in burned gas when applying LIBS for the measurement of unburned carbon content in fly ash under the burned gas conditions.

7.1.2 Trace species measurement using low pressure LIBS

The LIBS signals of trace species were detected at low pressure using nanosecond and picosecond lasers under various conditions. The detection features of LIBS have been discussed in detail.

(1) Hg, Sr and Cs have been measured using low pressure LIBS under different conditions. According to the measurement results of Hg, Sr and Cs, the interference of continuum emission from plasma itself decreased dramatically, which led to the increase of signal to background ratio at reducing pressure condition. Stable and longer plasma was generated under reduced pressure conditions. In the case of Hg measurement, Hg signal with low NO emission intensity was observed using picosecond lasers, which demonstrated the enhancement of I_{Hg}/I_{NO} in the low pressure and short pulse plasma generation process, especially using 35 ps laser. There was no great difference in I_{Hg}/I_{NO} by nanosecond (6 ns) breakdown between central and edge signals. The edge I_{Hg}/I_{NO} of the picosecond (150 ps) breakdown was significantly better than the central I_{Hg}/I_{NO}, due to the non-equilibrium plasma generation process.

(2) The delay time is an important parameter in LIBS process concerning the plasma temperature. Under low pressure conditions, the delay time was not a determining factor for Hg measurement in air. In the measurement of iodine using 532 nm breakdown, $I_{I\text{-}3}/I_{N\text{-}1}$ increased when the delay time increased. The measured results of I_{Hg}/I_{NO} and $I_{I\text{-}3}/I_{N\text{-}1}$ at 400 mJ/p were much better than that at 1000 mJ/p because of the effect of electron impact ionization.

(3) The laser-induced plasma process can be controlled using laser pulse width for the influence of multi-photon ionization. I_{Hg}/I_{NO} of picosecond laser with 35 ps pulse width induced plasma was the highest among three pulse width lasers. Meanwhile, the ratio of I_{Hg}/I_{NO} increased when decreasing the pressure to improve the detection limit. Short pulse width lasers including 150 ps and 35 ps lasers were employed to measure iodine signal. The intensity ratio of I-3 to N-1 was enhanced using short pulse width lasers, especially 35 ps laser. It is feasible to enhance LIBS detection limit by low pressure and short pulse laser induced plasma, such as picosecond laser with 35 ps pulse width.

(4) The buffer gas effect has been analyzed by Hg and iodine measurements using N_2 and air as the buffer gas. The spectra in air were different from that in N_2 due to the high quenching rates of excited Hg and iodine in buffer gas of air and different coexisting molecular and atomic emissions. The detection limit of Hg in N_2 using nanosecond breakdown was 3.5 ppb ($3\sigma/m_s$) at 6.6 kPa. Low pressure laser-induced plasma process was also employed

to measure Hg with buffer gas of air using different pulse with lasers. The Hg detection limit of nanosecond breakdown was 450 ppb ($3\sigma/m_s$) at 700 Pa. According to the enhancement of picosecond breakdown at low pressure, the detection limit was evaluated to be 30 ppb ($3\sigma/m_s$) in picosecond (35 ps) breakdown at 700 Pa. Iodine detection limit in N_2 was 60 ppb ($3\sigma/m_s$) in nanosecond breakdown at pressure of 700 Pa. there was not evident enhancement of iodine detection limit employing short pulse width breakdowns. Using low pressure LIBS, it is feasible to measure iodine in air, especially short pulse laser breakdown. The detection limit of iodine in air became worse due to the high quenching rate of excited iodine in buffer gas of air.

7.1.3 Trace species measurement using LB-TOFMS

Laser breakdown TOFMS method was developed and applied to detect trace species, such as mercury and iodine in mixture. In order to measure Hg and iodine with heavy mass in mixture, laser breakdown process is essential to eliminate or minimize fragmentation from other species. Measurements employing 532 nm and 1064 nm breakdowns display the results without interference of fragmentations compared to that the laser breakdown process using 266 nm in the mass region of 30-300 m/z. Furthermore, the isotope can be detected because the method depends on the mass of atom and molecule with high sensitivity.

(1) Different breakdown patterns of several hydrocarbons were measured for the detection of H and C contents using 1064 nm and 532 nm breakdowns. Each hydrocarbon shows its characteristic breakdown mass spectra. It is found that a linear relation between element ratio of H to C in molecules and breakdown ion signals. The yields of H and C ions were highly consistent with the structure of these molecules. H and C yields using 532 nm breakdown are higher compared with that using 1064 nm breakdown.

(2) Influence of laser power on signal intensity shows the linear growth when increasing the laser power. The signal intensity was also correlated with the pressure in the test chamber. However, because of the combination influence of laser radiation and produced electrons, the signal intensity presents a nonlinear growth.

(3) As two wavelengths were employed to break and ionize the samples of Hg and CH_3I, the results using 532 nm breakdown present higher signal intensity than that using 1064 nm breakdown. The influence of pressure in the test chamber on Hg^+ and I^+ signal intensity shows the linear growth when the pressure increases. Because of the recombination of Hg^+ and I^+ with electrons, power dependence of Hg^+ and I^+ signal intensity increases first and then decreases. Among the buffer gases of N_2, Ar and He, the lowest recombination rate was measured using He as a buffer gas because of the highest ionization potential of He. Due to the influence of recombination, the method of enlarging focal area and decreasing the laser power reduces the recombination rate of Hg^+ and I^+ with electrons. It is a proven means to enhance the detection limit with appropriate focal area.

(4) Using 35 ps laser breakdown process, the intensity of I^+ signal can be enhanced 1.3 times and Hg^+ signal intensity can be enhanced 3.8 times compared to nanosecond breakdown. The detection limits of Hg^+ and I^+ signal were 0.82 ppb ($3\sigma/m_s$) and 6.18 ppb ($3\sigma/m_s$) using 35 ps laser breakdown operated at 532 nm respectively. It is demonstrated that the method is significantly desirable to measure Hg and iodine in mixture.

7.2 Suggestions

The LIBS technique with the temperature correction method is useful for the analysis of coal combustion in the power plants because of its sensitivity, fast analysis and non-contact features. Further studies will focus on the real-time content detection of fly ash in real power plant applications. Low pressure LIBS and LB-TOFMS feature the sensitive and rapid detection without complex sample preparation compared to the conventional methods. These two methods will be applied to the practical applications, such as monitoring systems of power plants and environment according to the requirements because of their different features.

References

[1] Gauderman, W.J.; Gilliland, G.F.; Vora, H.; Avol, E.; Stram, D.; McConnell, R.; Thomas, D.; Lurmann, F.; Margolis, H.G.; Rappaport, E.B.; Berhane, K.; Peters, J.M. Association between air pollution and lung function growth in Southern California children: results from a second cohort. *Am J Respir Crit Care Med.* **2002**, *166*, 76-84.

[2] Arden Pope III, C.; Dockery, D.W. Health effects of fine particulate air pollution: lines that connect. *J. Air Waste Manage. Assoc.* **2006**, *56*, 709-742.

[3] Kampa, M.; Castanas, E. Human health effects of air pollution. *Environ. Pollut.* **2008**, *151*, 362-367.

[4] Linak, W.P.; Yoo, J.I.; Wasson, S.J.; Zhu, W.Y.; Wendt, J.O.L.; Huggins, F.E.; Chen, Y.Z.; Shah, N.; Huffman, G.P.; Gilmour, M.I. Ultrafine ash aerosols from coal combustion: Characterization and health effects. *P. Combust. Inst.* **2007**, *31*, 1929-1937.

[5] Swaine, D.J. Why trace elements are important. *Fuel Process. Technol.* **2000**, *65-66*, 21-33.

[6] Oberdorster, G.; Oberdorster, E.; Oberdorster, J. Nanotoxicology: an emerging discipline evolving from studies of ultrafine particles. *Environ. Health Persp.* **2005**, *113*, 823-839.

[7] Curtis, L.; Rea, W.; Smith-Willis, P.; Fenyves, E.; Pan, Y. P. Adverse health effects of outdoor air pollutants. *Environ. Int.* **2006**, *32*, 815-830.

[8] Autrup, H. Ambient air pollution and adverse health effects. *Procedia Social and Behavioral Sciences* **2010**, *2*, 7333-7338.

[9] Ipolyi, I.; Massanisso, P.; Sposato, S.; Fodor, P.; Morabito, R. Concentration levels of total and methylmercury in mussel samples collected along the coasts of Sardinia Island (Italy). *Anal. Chim. Acta* **2004**, *505*, 145-151.

[10] Obrist, D. Atmospheric mercury pollution due to losses of terrestrial carbon pools? *Biogeochemistry* **2007**, *85*, 119-123.

[11] Lapanje, A.; Drobne, D.; Nolde, N.; Valant, J.; Muscet, B.; Leser, V.; Rupnik, M. Long-term Hg pollution induced Hg tolerance in the terrestrial isopod Porcellio scaber (Isopoda, Crustacea). *Environ. Pollut.* **2008**, *153*, 537-547.

[12] Li, P.; Feng, X. B.; Qiu, G. L.; Shang, L. H.; Li, Z. G. Mercury pollution in Asia: A review of the contaminated sites. *J. Hazard. Mater.* **2009**, *168*, 591-601.

[13] Papp, Z.; Dezső, Z.; Daróczy, S. Significant radioactive contamination of soil around a coal-fired thermal power plant. *J. Environ. Radioact.* **2009**, *59*, 191-205.

[14] Brim, H.; Venkateswaran, A.; Kostandarithes, H.M.; Fredrickson, J.K.; Daly, M.J. Engineering deinococcus geothermalis for bioremediation of high-temperature radioactive waste environments. *Appl. Environ. Microbiol.* **2003**, *69*, 4575-4582.

[15] Kanai, Y. Monitoring of aerosols in Tsukuba after Fukushima Nuclear Power Plant incident in 2011. *J. Environ. Radioact.* **2012**, *111*, 33-37.

[16] Buesseler, K.; Aoyama, M.; Fukasawa, M. Impacts of the Fukushima nuclear power plants on marine radioactivity. *Environ. Sci. Technol.* **2011**, *45*, 9931-9935.

[17] Tanaka, K.; Takahashi, Y.; Sakaguchi, A.; Umeo, M.; Hayakawa, S.; Tanida, H.; Saito, T.; Kanai, Y. Vertical profiles of iodine-131 and cesium-137 in soils in Fukushima prefecture related to the Fukushima Daiichi Nuclear Power Station accident. *Geochem. J.* **2012**, *46*, 73-76.

[18] Sato, I.; Kudo, H.; Tsuda, S. Removal efficiency of water purifier and adsorbent for iodine, cesium, strontium, barium and zirconium in drinking water. *J. Toxicol. Sci.* **2011**, *36*, 859-834.

[19] Kim, C.K.; Byun, J.I.; Chae, J.S.; Choi, H.Y.; Choi, S.W.; Kim, D.J.; Kim, Y.J.; Lee, D.M.; Park, W.J.; Yim, S.A.; Yun, J.Y. Radiological impact in Korea following the Fukushima nuclear accident. *J. Environ. Radioact.* **2012**, *111*, 70-82.

[20] Manolopoulou, M.; Vagena, E.; Stoulos, S.; Ioannidou, A.; Papastefanou, C. Radioiodine and radiocesium in Thessaloniki, Northern Greece due to the Fukushima nuclear accident. *J. Environ. Radioact.* **2011**, *102*, 796-797.

[21] Deguchi, Y.; Noda, M.; Fukuda, Y.; Ichinose, Y.; Endo, Y.; Inada, M.; Abe, Y.; Iwasaki, S. Industrial applications of temperature and species concentration monitoring using laser diagnostics. *Meas. Sci. Technol.* **2002**, *13***,** R103-R115.

[22] Deguchi, Y. *Industrial Applications of Laser Diagnostics*, CRS Press, Taylor & Francis: New York, USA, **2011**.

[23] Ctvrtnickova, T.; Mateo, M.P.; Yañez, A.; Nicolas, G. Application of LIBS and TMA for the determination of combustion predictive indices of coals and coal blends. *Appl. Surf. Sci.* **2011**, *257*, 5447-5451.

[24] Haider, A.F.M.Y.; Rony, M.A.; Abedin, K.M. Determination of the ash content of coal without ashing: a simple technique using laser-induced breakdown spectroscopy. *Energy Fuels* **2013**, *27*, 3725-3729.

[25] Yuan, T.B.; Wang, Z.; Lui, S.L.; Fu, Y.T.; Li, Z.; Liu, J.M.; Ni, W.D. Coal property analysis using laser-induced breakdown spectroscopy. *J. Anal. At. Spectrom.* **2013**, *28*, 1045-1053.

[26] Wang, Z.Z.; Deguchi, Y.; Kuwahara, M.; Taira, T.; Zhang, X.B.; Yan, J.J.; Liu, J.P.; Watanabe, H.; Kurose, R. Quantitative elemental detection of size-segregated particles using laser-induced breakdown spectroscopy. *Spectrochim. Acta Part B* **2013**, *87*, 130-138.

[27] Wang, Z.Z.; Deguchi, Y.; Kuwahara, M.; Yan, J.J.; Liu, J.P. Enhancement of laser-induced breakdown spectroscopy(LIBS) detection limit by low pressure and short pulse laser-induced plasma process. *Appl. Spectrosc.* **2013**, *67*, 1242-1251.

[28] Noll, R.; Mönch, I.; Klein, O.; Lamott, A. Concept and operating performance of inspection machines for industrial use based on laser-induced breakdown spectroscopy. *Spectrochim. Acta Part B* **2005**, *60*, 1070-1075.

[29] Gaft, M.; Sapir-Sofer, I.; Modiano, H.; Stana, R. Laser induced breakdown spectroscopy for bulk minerals online analyses. *Spectrochim. Acta Part B* **2007**, *62*, 1496-1503.

[30] Boué-Bigne, F. Laser-induced breakdown spectroscopy applications in the steel industry: Rapid analysis of segregation and decarburization. *Spectrochim. Acta Part B* **2008**, *63*, 1122-1129.

[31] Cho, H.H.; Kim, Y.J.; Jo, Y.S.; Kitagawa, K.; Arai, N.; Lee. Y.I. Application of laser-induced breakdown spectrometry for direct determination of trace elements in starch-based flours. *J. Anal. At. Spectrom.* **2001**, *16*, 622-627.

[32] Pouzar, M.; Černohorský, T.; Průšová, M.; Prokopčáková, P.; Krejčová, A. LIBS analysis of crop plants. *J. Anal. Atom. Spectrom.* **2009**, *24*, 953-957.

[33] Juvé, V.; Portelli, R.; Boueri, M.; Baudelet, M.; Yu, J. Space-resolved analysis of trace elements in fresh vegetables using ultraviolet nanosecond laser-induced breakdown spectroscopy. *Spectrochim. Acta Part B* **2008**, *63*, 1047-1053.

[34] Samek, O.; Beddows, D.C.S.; Telle, H.H.; Kaiser, J.; Liška, M.; Cáceres, J.O.; Gonzáles Ureña, A. Quantitative laser-induced breakdown spectroscopy analysis of calcified tissue samples. *Spectrochim. Acta Part B* **2001**, *56*, 865-875.

[35] Thareja, R.K.; Sharma, A.K.; Shukla, S. Spectroscopic investigations of carious tooth decay. *Med. Eng. Phys.* **2008**, *30*, 1143-1148.

[36] St-Onge, L.; Kwong, E.; Sabsabi, M.; Vadas, E.B. Quantitative analysis of pharmaceutical products by laser-induced breakdown spectroscopy. *Spectrochim. Acta Part B* **2002**, *57*, 1131-1140.

[37] Ma, Q.L.; Motto-Ros, V.; Lei, W.Q.; Boueri, M.; Zheng, L.J.; Zeng, H.P.; Bar-Matthews, M.; Ayalon, A.; Panczer, G.; Yu, J. Multi-elemental mapping of a speleothem using laser-induced breakdown spectroscopy. *Spectrochim. Acta Part B* **2010**, *65*, 707-714.

[38] Gittins, C.M.; Castaldi, M.J.; Senkan, S.M.; Rohlfing, E.A. Real-time quantitative analysis of combustion-generated polycyclic aromatic hydrocarbons by resonance-enhanced multiphoton ionization time-of-flight mass spectrometry. *Anal. Chem.* **1997**, *69*, 286-293.

[39] Heger, H.J.; Zimmermann, R.; Dorfner, R.; Beckmann, M.; Griebel, H.; Kettrup, A.; Boesl, U. On-line emission analysis of polycyclic aromatic hydrocarbons down to pptv concentration levels in the flue gas of an incineration pilot plant with a mobile resonance-enhanced multiphoton ionization time-of-flight mass spectrometer. *Anal. Chem.* **1999**, *71*, 46-57.

[40] Bente, M.; Sklorz, M.; Streibel, T.; Zimmermann, R. Thermal desorption-multiphoton ionization time-of-flight mass spectrometry of individual aerosol particles: a simplified approach for online single-particle analysis of polycyclic aromatic hydrocarbons and their derivatives. *Anal. Chem.* **2009**, *81*, 2525-2536.

[41] Gullett, B.K.; Touati, A.; Oudejans, L.; Ryan, S.P. Real-time emission characterization of organic air toxic pollutants during steady state and transient operation of a medium duty diesel engine. *Atmos. Environ.* **2006**, *40*, 4037-4047.

[42] Deguchi, Y.; Tanaka, N.; Tsuzaki, M.; Fushimi, A.; Kobayashi, S.; Tanabe, K. Detection of components in nanoparticles by resonant ionization and laser breakdown time-of-flight mass spectrometry. *Environ. Chem.* **2008**, *5*, 402-412.

[43] Dobashi, S.; Yamaguchi, Y.; Izawa, Y.; Deguchi, Y.; Wada, A.; Hara, M. Laser mass spectrometry: rapid analysis of polychlorinated biphenyls in exhaust gas of disposal plants. *Journal of Environment and Engineering* **2007**, *2*, 25-34.

[44] Deguchi, Y.; Dobashi, S.; Fukuda, N.; Shinoda, K.; Morita, M. Real-time PCB monitoring using time-of-flight mass spectrometry with picosecond laser ionization. *Environ. Sci. Technol.* **2003**, *37*, 4737-4742.

[45] Dobashi, S.; Yamaguchi, Y.; Izawa, Y.; Wada, A.; Hara, M. Safety management by use of laser mass spectrometry of polychlorinated biphenyls (PCBs) in the processed gas and work environment of a PCB disposal plant. *J. Mater. Cycles Waste Manage.* **2009**, *11*, 148-154.

[46] Pignone, M.; Greth, K.M.; Cooper, J.; Emerson, D.; Tang, J. Identification of mycobacteria by matrix-assisted laser desorption ionization–time-of-flight mass spectrometry. *J. Clin. Microbiol.* **2006**, *44*, 1963-1970.

[47] Hazen, T.H.; Martinez, R.J.; Chen, Y.F.; Lafon, P.C.; Garrett, N.M.; Parsons, M.B.; Bopp, C.A.; Sullards, M.C.; Sobecky, P.A. Rapid identification of vibrio parahaemolyticus by whole-cell matrix-assisted laser desorption ionization–time of flight mass spectrometry. *Appl. Environ. Microbiol.* **2009**, *75*, 6745-6756.

[48] Body, D.; Chadwick, B.L. Simultaneous elemental analysis system using laser induced breakdown spectroscopy. *Rev. Sci. Instrum.* **2001**, *75*, 1625-1629.

[49] Haider, A.F.M.Y.; Rony, M.A.; Lubna, R.S.; Abedin, K.M. Detection of multiple elements in coal samples from Bangladesh by laser-induced breakdown spectroscopy. *Opt. Laser Technol.* **2011**, *43*, 1405-1410.

[50] Wallis, F.J.; Chadwick, B.L.; Morrison, R.J.S. Analysis of lignite using laser-induced breakdown spectroscopy. *Appl. Spectrosc.* **2000**, *54*, 1231-1235.

[51] Mateo, M.P.; Nicolas, G.; Yañez, A. Characterization of inorganic species in coal by laser-induced breakdown spectroscopy using UV and IR radiations. *Appl. Surf. Sci.* **2007**, 254, 868-872.

[52] Yuan, T.B.; Wang, Z.; Li, L.Z.; Hou, Z.Y.; Li, Z.; Ni, W.D. Quantitative carbon measurement in anthracite using laser-induced breakdown spectroscopy with binder. *Appl. Opt.* **2012**, *51*, B22-B29.

[53] Ctvrtnickova, T.; Mateo, M.P.; Yañez, A.; Nicolas, G. Characterization of coal fly ash components by laser-induced breakdown spectroscopy. *Spectrochim. Acta Part B* **2009**, *64*, 1093-1097.

[54] Ctvrtnickova, T.; Mateo, M.P.; Yañez, A.; Nicolas, G. Laser induced breakdown spectroscopy application for ash characterization for a coal fired power plant. *Spectrochim. Acta Part B* **2010**, *65*, 734-737.

[55] Noda, M.; Deguchi, Y.; Iwasaki, S.; Yoshikawa, N. Detection of carbon content in a high-temperature and high-pressure environment using laser-induced breakdown spectroscopy. *Spectrochim. Acta Part B* **2002**, *57*, 701-709.

[56] Kurihara, M.; Ikeda, K.; Izawa, Y.; Deguchi, Y.; Tarui, H. Optimal boiler control through real-time monitoring of unburned carbon in fly ash by laser-induced breakdown spectroscopy. *Appl. Opt.* **2003**, *42*, 6159-6165.

[57] Zhao, Y.H.; Horlick, G. A spectral study of charge transfer and Penning processes for Cu, Zn, Ag, and Cd in a glow discharge. *Spectrochim. Acta Part B* **2006**, *61*, 660-673.

[58] Meij, R. A Sampling method based on activated carbon for gaseous mercury in ambient air and flue gases. *Water Air Soil Pollut.* **1991**, *56*, 117-129.

[59] Landis, M.S.; Stevens, R.K.; Schaedlich, F.; Prestbo, E.M. Development and characterization of an annular denuder methodology for the measurement of divalent inorganic reactive gaseous mercury in ambient air. *Environ. Sci. Technol.* **2002**, *36*, 3000-3009.

[60] Lee, S.J.; Seo, Y.C.; Jang, H.N.; Park, K.S.; Baek, J.I.; An, H.S.; Song K.C. Speciation and mass distribution of mercury in a bituminous coal-fired power plant. *Atmos. Environ.* **2006**, *40*, 2215-2224.

[61] Wolterbeek, B. Biomonitoring of trace element air pollution: principles, possibilities and perspectives. *Environ. Pollut.* **2002**, *120*, 11-21.

[62] Imperatoa, M.; Adamob, P.; Naimoa, D.; Arienzob, M.; Stanzionea, D.; Violanteb, P. Spatial distribution of heavy metals in urban soils of Naples city (Italy). *Environ. Pollut.* **2003**, *124*, 247-256.

[63] Ömer, D.; Ahmet, D.; Ahmet, B. Determination of heavy metals (Cd, Pb) and trace elements (Cu, Zn) in sediments and fish of the Southeastern Aegean Sea (Turkey) by atomic absorption spectrometry. *Food Chem.* **2006**, *95*, 157-162.

[64] Yokoyama, T.; Asakura, K.; Matsuda, H.; Ito, S.; Noda, N. Mercury emissions from a coal-fired power plant in Japan. *Sci. Total Environ.* **2000**, *259*, 97-103.

[65] Meij, R.; Vredenbregt, L.H.J.; Winkel, H.T. J. The fate and behavior of mercury in coal-fired power plants. *Air Waste Manage. Assoc.* **2002**, *52*, 912-917.

[66] Meij, R.; Winkel, H.T. Mercury emissions from coal-fired power stations: The current state of the art in the Netherlands. *Sci. Total Environ.* **2006**, *368*, 393-396.

[67] Wang, Y.J.; Duan, Y.F.; Yang, L.G.; Jiang, Y.M.; Wu, C.J.; Wang, Q.; Yang, X.H. Comparison of mercury removal characteristic between fabric filter and electrostatic precipitators of coal-fired power plants. *J. Fuel Chem. Technol.* **2008**, *36*, 23-29.

[68] Li, X.D.; Coles, B.J.; Ramsey, M.H.; Thornton, I. Sequential extraction of soils for multielement analysis by ICP-AES. *Chem. Geol.* **1995**, *124*, 109-123.

[69] Eggins, S.M.; Rudnick, R.L.; McDonough, W.F. The composition of peridotites and their minerals: a laser-ablation ICP–MS study. *Earth Planet. Sci. Lett.* **1998**, *154*, 53-71.

[70] Horn, I.; Rudnick, R.L.; McDonough, W.F. Precise elemental and isotope ratio determination by simultaneous solution nebulization and laser ablation-ICP-MS: application to U–Pb geochronology. *Chem. Geol.* **2000**, *164*, 281-301.

[71] Matsuura, H.; Hokura, A.; Katsuki, F.; Itoh, A.; Haraguchi, H. Multielement determination and speciation of major-to-trace elements in black tea leaves by ICP-AES and ICP-MS with the aid of size exclusion chromatography. *Anal. Sci.* **2001**, *17*, 391-398.

[72] Megan, R.L.H.; Joseph, M.; Robert, O.; Jennifer, B.; Yamac, D.; Caroline, M.; James, B.S. Ultrafast laser-based spectroscopy and sensing: applications in LIBS, CARS, and THz spectroscopy. *Sensors* **2010**, *10*, 4342-4372.

[73] Eland, K.L.; Stratis, D.N.; Lai, T.; Berg, M.A.; Goode, S.R.; Angel, S.M. Some comparisons of LIBS measurement using nanosecond and picosecond laser pulses. *Appl. Spectrosc.* **2001**, *55*, 279-285.

[74] Zhang, X.B.; Deguchi, Y.; Liu, J.P. Numerical simulation of laser induced weakly ionized helium plasma process by lattice Boltzmann method. *Jpn. J. Appl. Phys.* **2012**, *51*, 01AA04-01AA04-6.

[75] Davison, R.L.; Natusch, D.F.S.; Wallace, J.R.; Evans Jr. C.A. Trace elements in fly ash: dependence of concentration on particle size. *Environ. Sci. Technol.* **1974**, *8*, 1107-1113.

[76] Smith, R.D.; Campbell, J.A.; Nielson, K.K. Concentration dependence upon particle size of volatilized elements in fly ash. *Environ. Sci. Technol.* **1979**, *13*, 553-558.

[77] Linak, W.P.; Miller, C.A.; Wendt, J.O.L. Comparison of particle size distributions and elemental partitioning from the combustion of pulverized coal and residual fuel oil. *J. Air & Waste Manage. Assoc.* **2000**, *50*, 1532-1544.

[78] Seames, W.S. An initial study of the fine fragmentation fly ash particle mode generated during pulverized coal combustion. *Fuel Process. Technol.* **2003**, 81, 109-125.

[79] Gale, T.K.; Wendt, J.O.L. In-furnace capture of cadmium and other semi-volatile metals by sorbents. *P. Combust. Inst.* **2005**, *30*, 2999-3007.

[80] Payling, R.; Larkins, P. *Optical Emission Lines of the Elements*, John Wiley & Sons: New York, **2000**.

[81] Russell, N.V.; Méndez, L.B.; Wigley, F.; Williamson, J. Ash deposition of a Spanish anthracite: effects of included and excluded mineral matter. *Fuel* **2002**, *81*, 657-663.

[82] Sansonetti, C.J.; Salit, M.L.; Reader, J. Wavelengths of spectral lines in mercury pencil lamps. *Appl. Opt.* **1996**, *35*, 74-77.

[83] Herzberg, G. Molecular Spectra and Molecular Structure, 2nd ed.; Van Nostrand Reinhold Company: New York, U.S., **1950**; p.558.

[84] Minnhagen, L. The energy levels of neutral atomic iodine. *Ark. Fys. (Stockholm)* **1962**, *21*, 415-465.

[85] Moore, C.E. Selected tables of atomic spectra, atomic energy levels and multiplet tables - N I, N II, N III. In Nat. Stand. Ref. Data Ser., 2nd ed.; Nat. Bur. Stand.: U.S., **1975**; p. 80.

[86] Ogawa, M. Absorption cross sections of O_2 and CO_2 continua in the schumann and far - uv regions. *The Journal of Chemical Physics* **1971**, *54*, 2550-2556.

Acknowledgements

My thanks would go first to all people who have instructed and helped me a lot in the past few years. This dissertation can be completed successfully and I can graduate early less than three years. My deepest gratitude goes foremost to the professors including Prof. Deguchi, my supervisor in Tokushima University, and Prof. Yan and Prof. Liu, my supervisors in Xi'an Jiaotong University for their constant encouragement and guidance at all the stages. I am also greatly indebted to the members in our laboratory and the staffs who gave me their help and time as possible as they could during the period I studied in Japan, as well as my friends in Tokushima University. Last I also owe my sincere gratitude to my beloved family and boyfriend for their loving considerations and great confidence in me all through these years.

Achievements

Papers

<published or accepted>

[1] **Wang, Z.Z.**; Deguchi, Y.; Kuwahara, M.; Taira, T.; Zhang, X.B.; Yan, J.J.; Liu, J.P.; Watanabe, H.; Kurose, R. Quantitative elemental detection of size-segregated particles using laser-induced breakdown spectroscopy. *Spectrochim. Acta Part B* **2013**, *87*, 130-138.

[2] **Wang, Z.Z.**; Deguchi, Y.; Kuwahara, M.; Yan, J.J.; Liu, J.P. Enhancement of laser-induced breakdown spectroscopy(LIBS) detection limit by low pressure and short pulse laser-induced plasma process. *Appl. Spectrosc.* **2013**, *67*, 1242-1251.

[3] **Wang, Z.Z.**; Deguchi, Y.; Kuwahara, M.; Zhang, X.B.; Yan, J.J.; Liu, J.P. Sensitive measurement of trace mercury using low pressure laser-induced plasma. *Jpn. J. Appl. Phys*. **2013**, *52*, 11NC05-1-11NCO5-6.

[4] **Wang, Z.Z.**; Deguchi, Y.; Yan, J.J.; Liu, J.P. Rapid detection of mercury and iodine using laser breakdown time-of-flight mass spectrometry. *Spectrosc. Lett.* **2014**, DOI: 10.1080/00387010.2013.859158.

(4.1) **Wang, Z.Z.**; Deguchi, Y.; Yan, J.J.; Liu, J.P. Rapid detection of trace heavy metals using laser breakdown time-of-flight mass spectrometry. *Procedia Environ. Sci*. **2013**, *18*, 329-337.

[5] Deguchi, Y.; **Wang, Z.Z.**; Yan, J.J.; Liu, J.P. Laser wavelength and pressure dependence of laser breakdown time-of-flight mass spectrometry. *Procedia Environ. Sci*. **2013**, *18*, 192-199.

[6] Zhang, X.B.; Deguchi, Y.; **Wang, Z.Z.**; Yan, J.J.; Liu, J.P. Detection characteristics of iodine by low pressure and short pulse laser-induced breakdown spectroscopy(LIBS). *J. Anal. At. Spectrom.* **2014**, *29*, 1082-1089.

[7] Deguchi, Y.; Kamimoto, T.; **Wang, Z.Z.**; Yan, J.J.; Liu, J.P.; Watanabe, H.; Kurose, R. Applications of laser diagnostics to thermal power plants and engines. *Appl. Therm. Eng*. **2014**, DOI: 10.1016/j.applthermaleng.2014.05.063.

<under review>

[8] **Wang, Z.Z.**; Deguchi, Y.; Yan, J.J.; Liu, J.P. Breakdown pattern of hydrocarbons by laser breakdown time-of-flight mass spectrometry. *Spectrosc. Lett*. **2014**.

International symposiums

[1] **Wang, Z.Z.**; Deguchi, Y.; Kuwahara, M.; Taira, T.; Zhang, X.B.; Yan, J.J.; Liu, J.P.; Watanabe, H.; Kurose, R. Elemental detection of classified particles using laser-induced breakdown spectroscopy. 7th International Conference on Laser Induced Breakdown Spectroscopy. Sept. 29th, 2012---Oct. 4th, 2012. oral: S-12-4, p.98.

[2] **Wang, Z.Z.**; Deguchi, Y.; Kuwahara, M.; Zhang, X.B.; Yan, J.J.; Liu, J.P. Sensitive measurement of trace elements using low pressure and short pulse laser-induced plasma. 5th International Symposium on Advanced Plasma Science and its Applications for Nitrides and Nanomaterials. Jan. 28th, 2013---Feb. 1st, 2013. poster: P1041A, p.89.

[3] Deguchi, Y.; **Wang, Z.Z.**; Kuwahara, M.; Watanabe, H.; Kurose, R.; Yan, J.J.; Liu, J.P. Improvement on quantification measurement of fly ash contents using laser induced breakdown spectroscopy. 5th International Symposium on Advanced Plasma Science and its Applications for Nitrides and Nanomaterials. Jan. 28th, 2013---Feb. 1st, 2013. poster: P1035A, p.86.

[4] **Wang, Z.Z.**; Deguchi, Y.; Yan, J.J.; Liu, J.P. Measurement of isotopic samples using laser breakdown time-of-flight mass spectrometry. International Conference on Laser Applications in Nuclear Engineering. April 23rd, 2013---April 25th, 2013. poster: LANEp8-6, p.50.

[5] **Wang, Z.Z.**; Deguchi, Y.; Yan, J.J.; Liu, J.P. Rapid detection of trace heavy metals using laser breakdown time-of-flight mass spectrometry. 2013 International Symposium on Environmental Science and Technology. June 4th, 2013---June 7th, 2013. oral, pp.264-271.

[6] Deguchi, Y.; **Wang, Z.Z.**; Yan, J.J.; Liu, J.P. Laser wavelength and pressure dependence of laser breakdown time-of-flight mass spectrometry. 2013 International Symposium on Environmental Science and Technology. June 4th, 2013---June 7th, 2013. oral, pp.150-157.

[7] **Wang, Z.Z.**; Deguchi, Y.; Yan, J.J.; Liu, J.P. Comparison of detection characteristics of trace heavy metals using low pressure laser-induced breakdown spectroscopy and laser breakdown time-of-flight mass spectrometry. 7th Euro-Mediterranean Symposium on Laser Induced Breakdown Spectroscopy. Sept. 16th, 2013---Sept. 20th, 2013. poster: P_094, p.203.

[8] Deguchi, Y.; **Wang, Z.Z.**; Yan, J.J.; Liu, J.P. Sensitive detection of trace heavy metals using low pressure and short pulse width laser-induced breakdown spectroscopy. 7th Euro-Mediterranean Symposium on Laser Induced Breakdown Spectroscopy. Sept. 16th, 2013---Sept. 20th, 2013. oral: O_62, p.92.

[9] Deguchi, Y.; Kamimoto, T,; **Wang, Z.Z.**; Yan, J.J.; Liu, J.P. Applications of laser diagnostics to engines and thermal power plants. 2013 International Workshop on Heat Transfer Advances for Energy Conservation and Pollution Control. Oct. 18th, 2013---Oct. 21st, 2013. oral. **[invited presentation]**

[10] **Wang, Z.Z.**; Deguchi, Y.; Yan, J.J.; Liu, J.P. Sensitive measurement of element content using low pressure laser-induced breakdown spectroscopy and laser breakdown time-of-flight mass spectrometry. International Workshop on Laser Application for Nuclear Decommissioning and Decontamination. Dec. 12th, 2013. oral, pp.24-25.

Domestic workshops

[1] **Wang, Z.Z.**; Deguchi, Y.; Kuwahara, M.; Taira, T.; Zhang, X.B.; Yan, J.J.; Liu, J.P.; Watanabe, H.; Kurose, R. Elemental detection of classified particles using laser-induced breakdown spectroscopy. 東北大学金属材料研究所ワークショップ -素材製造プロセスおよび新素材開発の迅速化・高度化に資する分析・解析技術 -, Tohoku University. Dec. 17th, 2012---Dec. 19th, 2012. oral, pp.129-132. **[invited presentation]**

[2] **Wang, Z.Z.**; Deguchi, Y.; Yan, J.J.; Liu, J.P. Detection of trace heavy metals using LIBS and laser breakdown TOFMS. 中四国熱科学・工学研究会, 平成 25 年度研究討論会, Hiroshima University. May 18th, 2013. oral.

[3] **Wang, Z.Z.**; Deguchi, Y.; Yan, J.J.; Liu, J.P. Application of laser-induced breakdown spectroscopy and laser breakdown time-of-flight mass spectrometry in thermal power plant. Symposium on applications of advanced measurement technologies. Dec. 19th, 2013---Dec. 20th, 2013. poster 10: P010, pp.44-46.

Dissertation for Doctoral Degree